III-V SEMICONDUCTOR
LASERS AND DETECTORS

Thesis by

Liew-Chuang Chiu

In Partial Fulfillment of the Requirements

for the degree of

Doctor of Philosophy

California Institute of Technology

Pasadena, California

1983

(Submitted May 12, 1983)

To my parents

ACKNOWLEDGEMENTS

I would like to express my sincere gratitude to my advisor, Professor Amnon Yariv, for his encouragement and support throughout my graduate studies at Caltech. His keen scientific intuition and extraordinary physical insights have been a constant source of inspiration. It has been a privilege to be a member of his highly motivated quantum electronics research group.

A special thanks goes to Dr. Shlomo Margalit, who initiated valuable ideas leading to much of the work in this thesis. I am especially thankful to Dr. Tom Koch, who introduced me to the field of quantum electronics and had provided valuable assistance throughout my work. I am also indebted to Dr. Pei-Chuang Chen, Ti-rong Chen, Kit-Lai Yu, and John S. Smith, who collaborated in much of the work reported here. I would also like to thank Christopher Harder, Kerry Vahala, Drs. Henry Blauvelt, Abraham Hasson, Uziel Koren, and Kam-Yin Lau for their valuable assistance. The invaluable technical assistance of Mr. Desmond Armstrong deserves a note of special thanks.

Abstract

The subjects of this thesis can be divided into two main categories: III-V semiconductor lasers and detectors. The first two chapters are concerned with the InGaAsP/InP laser diodes. The final two chapters are related to fundamental problems in the avalanche photodiodes and the new class of quantum well infrared detectors.

The kinetics of the mass transport phenomenon in InP is studied experimentally. Application of this technique to laser fabrication has resulted in very low threshold terrace mesa lasers.

The continuing problem of the excess temperature sensitivity of InGaAsP lasers and light emitting diodes is studied in detail. Non-radiative Auger recombination and electron leakage are found to be important factors affecting the temperature sensitivities of these devices.

Impact ionization in the GaAlSb system is investigated. The resonant nature of the enhanced impact ionization of holes is discussed. Further enhancement is predicted to be possible in quantum well structures.

The new class of quantum well infrared detectors is described. Theoretical considerations on absorption coefficients and other parameters essential to device design and performance are discussed.

-TABLE OF CONTENTS-

Chapter 1 **INTRODUCTION** 1

Chapter 2 **STUDY AND APPLICATION OF THE MASS TRANSPORT PHENOMENON IN InP**

2.1 Introduction 4

2.2 Mass Transport Process 4

2.3 Properties of p-n Junctions "Grown" by Mass Transport Process 16

2.4 Application and Effects on Laser Performance 21

References - Chapter 2 29

Chapter 3 **TEMPERATURE DEPENDENCE OF THE THRESHOLD CURRENT OF InGaAsP DOUBLE HETEROSTRUCTURE LASERS**

3.1 Introduction 30

3.2 Interband Auger Recombination in InGaAsP 32

3.3 Nature of Electron Leakage in InGaAsP/InP Double Heterostructures 44

3.4 Carrier Leakage in InGaAsP/InP Heterostructure-Experiment 46

3.5 Carrier Leakage in InGaAsP/InP Heterosturcture-Theory 54

3.6 Dependence of T_0 on P-Cladding Layer Doping Level 66

3.7 Auger Recombination in Quantum Well InGaAsP Lasers 74

Appendix A 81

References - Chapter 3 84

Chapter 4 IMPACT IONIZATION IN III-V SEMICONDUCTOR COMPOUNDS

4.1 Introduction 87

4.2 Electron and Hole Impact Ionization Coefficients 90

4.3 Resonant Enhanced Hole Impact Ionization in GaAlSb? 95

4.4 Resonant Enhanced Hole Impact Ionization in Quantum Wells 99

References - Chapter 4 104

Chapter 5 QUANTUM WELL INFRARED DETECTORS

5.1 Introduction 105

5.2 Free Carrier Absorption in GaAs/GaAlAs Quantum Wells 105

5.3 Phononless Free Carrier Absorption in Quantum Wells 107

5.4 Intervalence Band Absorption 112

5.5 Multi-Quantum-Well Infrared Detector 113

5.6 Proposed Infrared Detector Using Inter-Subband Absorption and Tunneling 118

Appendix F 125

References - Chapter 5 128

Chapter 1
Introduction

Semiconductor laser diodes, which emit coherent radiation through stimulated radiative recombination of electrons and holes in direct gap semiconductor materials, have numerous important applications in communications and consumer electronics. The small size, high efficiency, capability to be modulated directly to the GHz region, and feasibility to be integrated with other semiconductor electronic devices make them the most suitable candidates as light sources in optical fiber communication systems. Injection laser diodes employing the quaternary compound of InGaAsP lattice-matched to InP as active region are capable of emitting in the spectral range of 1.1-1.6 μm. This wavelength range falls in the region where modern optical fibers exhibit low loss and negligible dispersion. At 1.55 μm, silica fibers with attenuation as low as 0.2 dB/km have been attained. Moreover, the zero dispersion wavelength in single mode fibers can be controlled by a balance between the negative material dispersion and positive waveguide dispersion. As such, the zero dispersion wavelength can be shifted to the desired low loss region. Thus, for long distance high data rate intra- and inter-continental optical fiber communication, the quaternary lasers are the most promising light sources.

For high speed optical fiber communication, reliable lasers with low threshold are highly desirable. The buried heterostructure (BH) lasers, with built-in optical and carrier confinements, are attractive candidates for light transmitters in communication links. However, fabrication of conventional BH lasers requires a rather critical regrowth step in an Liquid Phase Epitaxy (LPE) system. As a

result, high yield is difficult to achieve. Chapter 2 discusses the mass transport process and its application to laser fabrication. This new technique makes possible the fabrication of low threshold lasers without the regrowth step. Section 2.2 describes experiments conducted to study the kinetics of the mass transport process. Section 2.3 studies the properties of p-n junctions "grown" by the mass transport process, and section 2.4 describes the application of the mass transport process in laser fabrication. In particular, the terrace mass transport laser and its performance will be described.

Though InGaAsP lasers have been demonstrated to be reliable light sources, a continuing problem plaguing these devices is their excess temperature sensitivity. The threshold currents of quaternary lasers are found to be rather sensitive to changes in ambient temperature. The temperature sensitivity of the threshold current of InGaAsP lasers is discussed in detail in chapter 3. Section 3.2 studies the interband non-radiative Auger recombination in InGaAsP. Section 3.3 discusses the nature of electron leakage over the InGaAsP/InP heterobarrier, and the possible relationship between the electron leakage and Auger recombination. In section 3.4, direct experimental evidence of electron leakage is presented. The effects of leakage on the laser threshold is described. Section 3.5 presents a theoretical model for the electron leakage, and calculated results are compared with available experimental data. Section 3.6 describes the experiments performed to verify some of the theoretical implications. In addition, a new modified laser structure with low temperature sensitivity and threshold will also be described. Finally, in section 3.7, Auger recombination in quantum well lasers is discussed briefly.

In an optical communication link, the performance of the receiver is just as important as that of the transmitter. For long distance optical communication, high speed, low noise detectors with high sensitivity are desirable. An important

class of semiconductor detectors is the Avalanche Photodiodes (APD's), which operate on the fundamental processes of carrier multiplication through impact ionization. Impact ionization in III-V semiconductors is the subject of chapter 4. Expressions for the electron and hole impact ionization coefficients in relatively weak fields ($< 10^5$ V/cm) are derived in section 4.2. Section 4.3 discusses the recently observed "resonant" enhanced hole impact ionization in GaAlSb. The resonant nature of the enhancement is disputed. In section 4.4, further enhancement in hole impact ionization in quantum well GaAlSb detectors is discussed.

Chapter 5 is concerned with a new class of infrared semiconductor detectors: the quantum well infrared detectors. Section 5.2 presents calculations of phonon-assisted free carrier absorption in GaAs/GaAlAs quantum wells. Section 5.3 discusses the possibility of having phononless free carrier absorption in quantum wells, with absoprtion coefficient estimated to be an order of magnitude larger than the phonon-assisted process. Section 5.4 discusses the intervalence band absorption in quantum wells. In section 5.5, two types of infrared quantum well detectors are proposed, using electron emission from quantum wells and intervalence band absorption respectively. In addition, preliminary experimental results of a detector of the former type will be presented. Finally, section 5.6 discusses the possibility of fabricating improved versions of the detectors using inter-subband absorption and tunneling in GaAs/GaAlAs heterojunction superlattices.

Chapter 2
Study and Application of the Mass Transport Phenomenon in InP

2.1 Introduction

The recently discovered mass transport phenomenon in InP [2.1,2.2] has generated considerable interest. Application of this technique to the fabrication of double heterostructure (DH) InGaAsP lasers has resulted in very low threshold devices [2.2]. For quaternary InGaAsP/InP lasers, this technique eliminates the critical regrowth step necessary in some structures, most notably the buried heterostructure (BH), thereby simplifying the entire fabrication process. The mass transport technique also provides greater flexibility in diode laser fabrication. The simplicity of the mass transport process makes it an attractive technique in the fabrication of other InP based semiconductor devices and in integrated opto-electronics. The viability of this technique in device fabrication will depend on its consistency and reproducibility. The process has been found to be highly reproducible and quite controllable over the entire wafer. In view of its potential, a better understanding of the process itself would be desirable. In this chapter, a study of the mass transport process is presented. The properties of the resultant mass transport p-n junctions in laser structures are described. Some advantages and disadvantages of the mass transport technique in laser fabrication and consequent effects on laser performance are also discussed.

2.2 Mass Transport Process

The mass transport process refered to in this chapter was first observed by

Liau and Walpole in the fabrication of a heterostructure laser with integrated passive waveguide [2.1]. It was found that when part of a quaternary layer sandwiched between InP layers was selectively etched away and the wafer heated to about 670 °C in an LPE system in an atmosphere of H_2 and PH_3, the original air space adjacent to the quaternary layer was filled with InP (see Fig. 1(a) of [2.1] and Figs. 2 of [2.2], or Figs. 2.3(b) and 2.4 in this chapter). Thus, "masses" of InP have been transported and "grown" on the exposed quaternary material. This InP mass transport phenomenon should be distinguished from the conventional LPE growth of InP, in which the InP is introduced from specially prepared growth solution. This new technique was successfully employed in the fabrication of a very low threshold buried heterostructure laser [2.2] and terrace laser to be described in section 2.4.

However, the origin and kinetics of the mass transport phenomenon thus observed was still unclear. Consequently, a systematic study was conducted to provide information on the origin and dynamics of the mass transport process, and also to probe the characteristics of mass transported InP homojunctions (i.e. p-n junction formed at the interface of the the mass transported InP and the original InP layer) to gain information on the crystalline quality of the mass transported region.

In the original work [2.1,2.2], mass transport of InP was observed in a liquid phase epitaxial (LPE) system in an atmosphere of H_2 and PH_3. In our case, however, PH_3 was not used, and the LPE system was merely flushed with hydrogen. In most of the cases studied, an InP cover wafer and a thick graphite plate were employed to cover the substrate, which is positioned in a recessed slot on a conventional LPE graphite boat. To accomplish the mass transport process, the LPE system was heated to around 675 °C and maintained at that temperature for a period of time depending on the desired experimental conditions and

circumstances.

To facilitate the study of the transport kinetics, U and V shape grooves were etched with iodic acid along the (011) and $(01\bar{1})$ crystallographic directions respectively on an InP substrate. The width and depth of the U shape groove were $\sim 10\mu m$ and $\sim 4.5\mu m$ respectively, and the corresponding values are $\sim 5\mu m$ and $\sim 2.5\mu m$ for the V shape groove (Figs. 2.1). After cleaning, the wafers were placed in a shallow slot on a conventional sliding graphite boat and loaded into the LPE system for mass transport. Experiments were performed in the temperature range of 670–740 °C and with heating times between forty minutes and three hours. Figs. 2.1 and 2.2 compare the shapes of the grooves before and after heating. The shapes of the grooves were clearly deformed by the heating. In addition to the rounded corners, the depth of the V shape groove was $\sim .3\mu m$ shallower after transport, and the width of the top opening was slightly wider. The bottom width of the U shape groove was $\sim 1.4\mu m$ narrower, and the slightly curved bottom became flat after transport. Notice that the convex corners were slightly rounded and materials were clearly "grown" at the concave corners, thus changing the width and depth of the groove.

A qualitative understanding of the mass transport process through the vapor phase could be gained by considering the variation of equilibrium vapor pressure with the curvature of the solid surface in equilibrium with its vapor. Denoting this pressure for a flat surface by P, then the deviation ΔP from P near a curved surface could be expressed as [2.3]

$$\frac{\Delta P}{P} = \frac{C}{T}\frac{1}{R} \qquad (2.2.1)$$

where C is a constant, T is the temperature and R the radius of curvature. For a convex surface, R is positive and the equilibrium vapor pressure at the surface exceeds P. Therefore, materials at such places are more prone to be

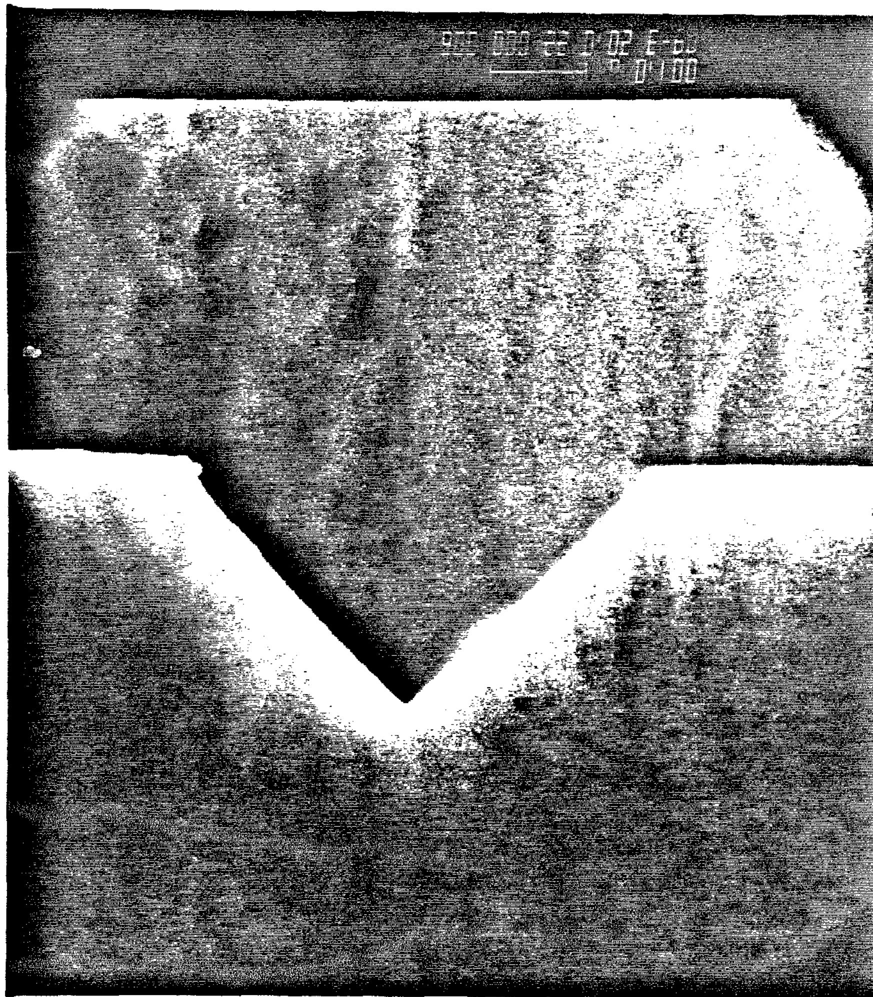

Figure 2.1(a) SEM picture of the V shape groove before mass transport.

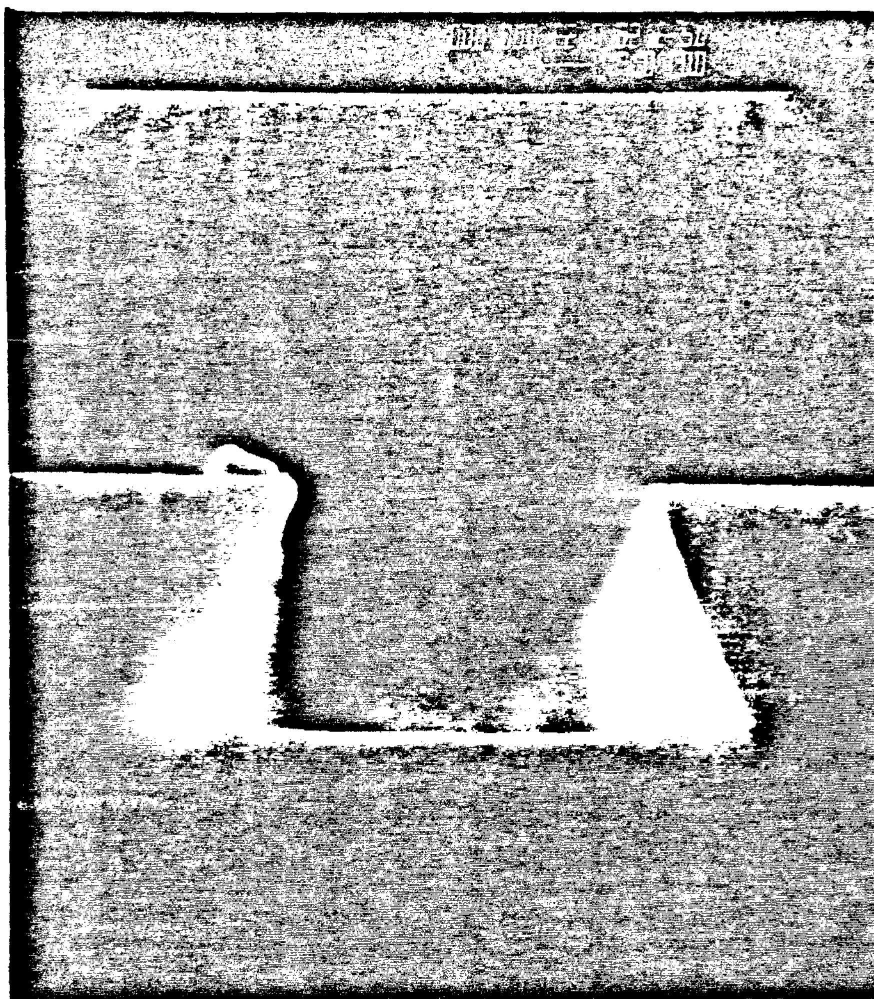

Figure 2.1(b) SEM picture of the U shape groove before mass transport.

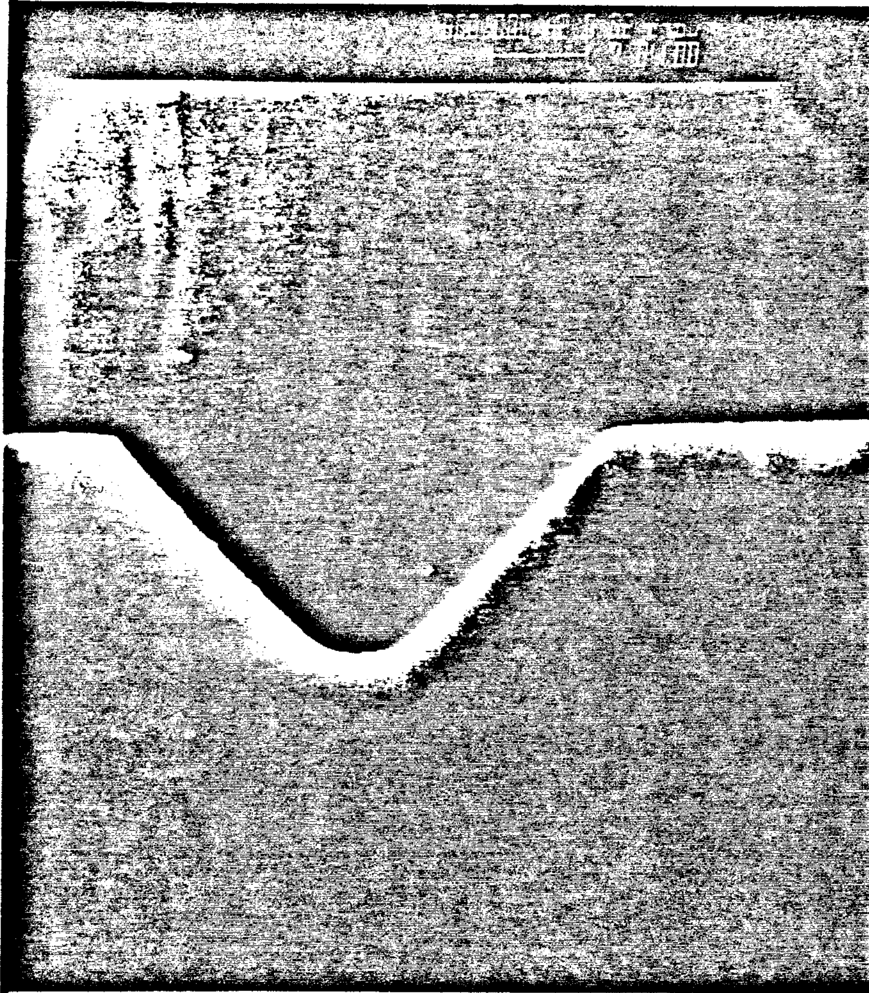

Figure 2.2(a) SEM picture of the V shape groove after high temperature (720 ^{o}C) mass transport.

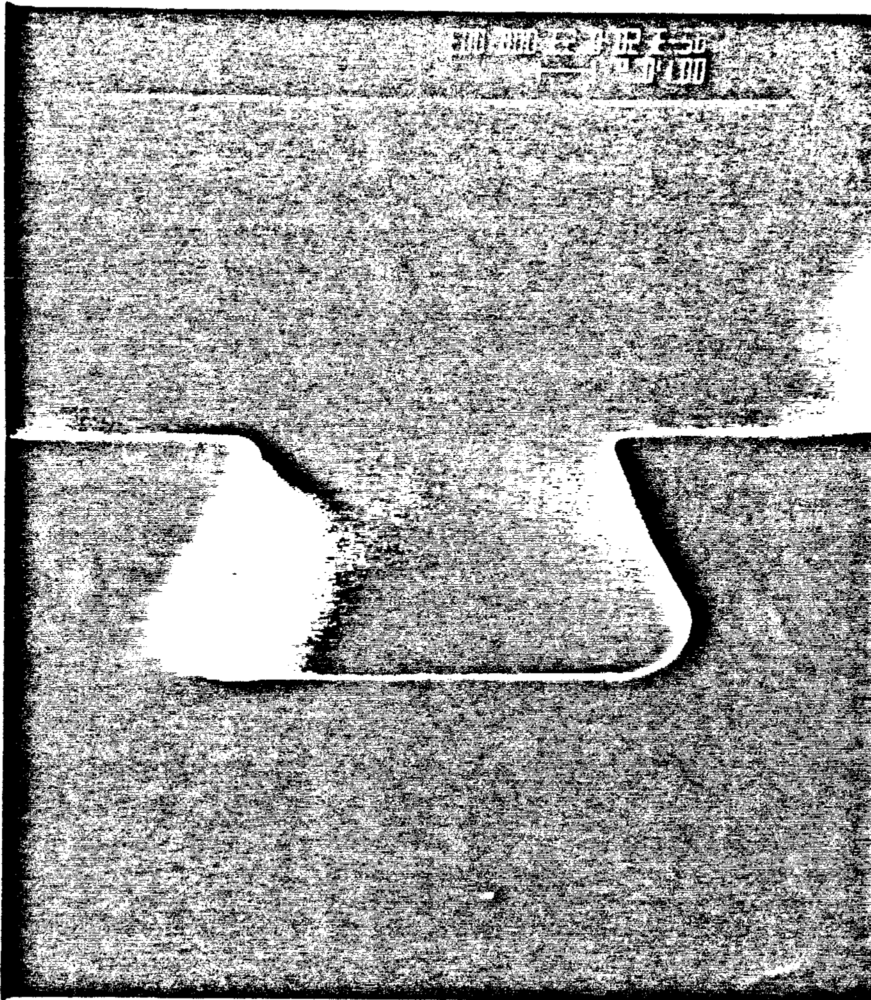

Figure 2.2(b) SEM picture of the U shape groove after high temperature (720 ^{o}C) mass transport.

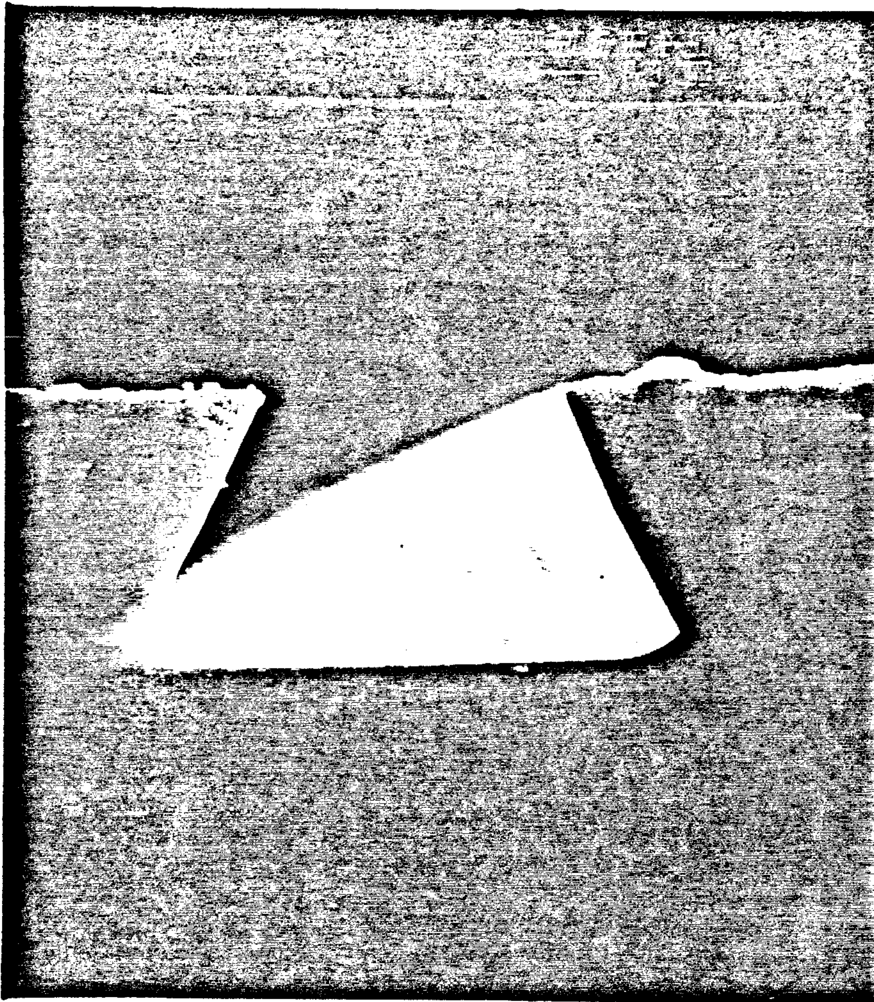

Figure 2.2(c) SEM picture of the U shape groove after "low" temperature (670 ^{o}C) mass transport.

evaporated. Conversely, near a concave surface with negative R, the equilibrium vapor pressure is lower and material could be grown. This is consistent with experimental observations of Figs. 2.1 and 2.2 and also Figs. 2.2 of [2.2]. In our experiments, a few tiny In droplets were always found on the surface of the wafer after the transport process. This is most probably the result of the dissociation of InP during the heating period.

Unfortunately, these observations alone do not eliminate other possible mass transport mechanisms, including the movements of InP molecules over the crystal surfaces in the solid phase or other solid phase mass migration processes. However, when a very thin layer of Si_3N_4 was deposited over the entire substrate, no discernible change in shape was observed after heating. This may indicate that the possibility of solid phase mass migration processes was quite remote. We recognize that the presence of the Si_3N_4 layer alters the surface property of the wafer and the above mentioned processes, though unlikely, cannot be positively ruled out.

To probe further, two experiments were performed. These employed the terrace laser structure with a long and narrow etched channel. The terrace was etched either along the (011) or the $(01\bar{1})$ crystallographic direction. Three epitaxial layers are then grown successively on the etched down portion of the wafer to form a DH laser structure (Fig. 2.3 (a)). The three LPE grown layers are n^+-InP cladding layer; undoped InGaAsP active layer; and p-InP cladding layer respectively. Following deposition of a new Si_3N_4 etching mask on the grown wafer, windows for chemical etching were opened with one side parallel to and approximately 5 μm away from the edge of the original terrace. The p-InP cladding layer underneath the windows was then removed selectively with a solution of hydrochloric acid and water (1.5 : 1). The quaternary InGaAsP layer was etched next, either with a solution of $KOH{:}K_3Fe(CN)_6{:}H_2O$ or $H_2SO_4{:}H_2O_2{:}H_2O$,

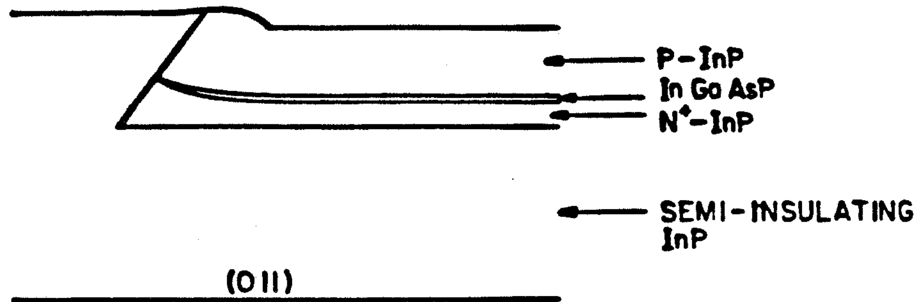

Figure 2.3(a) Schematic cross-section of the three basic layers of the DH terrace laser on semi-insulating InP along the (011) direction.

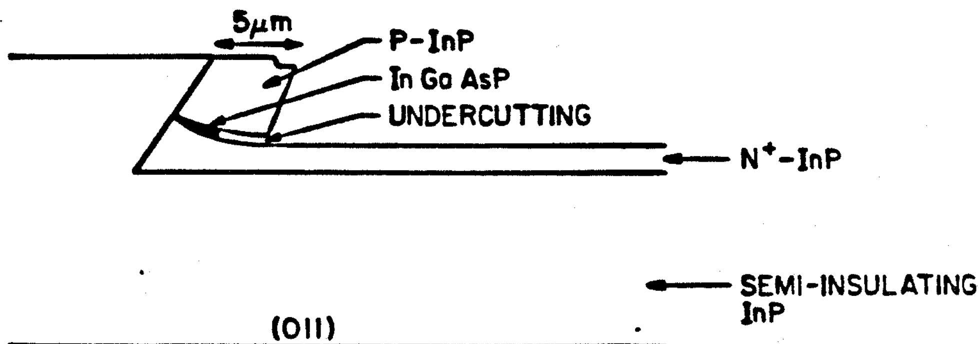

Figure 2.3(b) Schematic cross-section of 2.3(a) after the selective undercutting into the active layer.

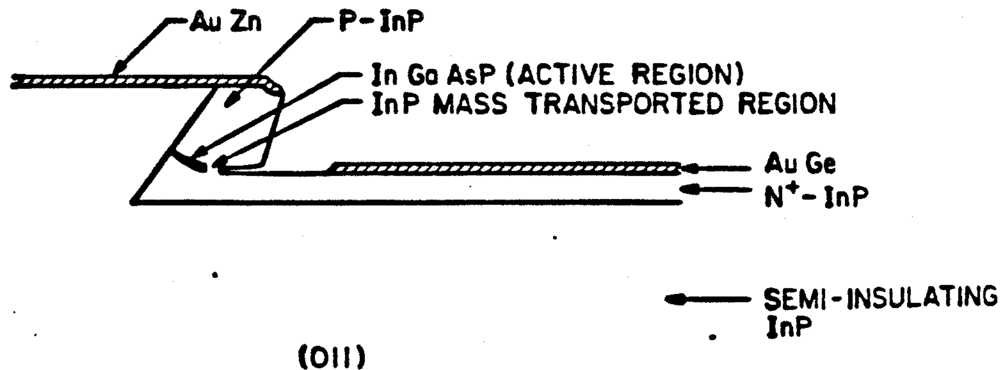

Figure 2.3(c) Schematic cross-section of the fabricated DH terrace laser structure.

resulting in a desired undercutting into the InGaAsP active layer as shown in Fig. 2.3(b). In the first experiment, the substrate and some phosphorous powder were placed in an evacuated ampule ($\sim 10^{-6} - 10^{-7}$ mm Hg). The mass of the phosphorous powder was estimated to produce a pressure slightly higher than one atmosphere. No mass transport was observed after heating at 700 °C for an hour. In the second experiment, a substrate and an InP wafer, separated by about 10 cm, were loaded into an evacuated ($\sim 10^{-7}$ mm Hg) ampule. In this experiment, a temperature difference of $\sim$ 30 °C was created along the axis of the ampule between the substrate (at 700 °C) and InP wafer (at 730 °C). After an hour, the InP wafer was decomposed with a drastic change in surface condition, but the surface of the substrate remained clean and free from In droplets. Moreover, mass transport was observed on the substrate and the etched channel was completed filled (as in Fig. 2.4(b)). These experiments provided strong support for the vapor phase transport mechanism.

The transport process was found to be a very sensitive function of temperature and less sensitive to the duration of heating. Figs. 2.1 consist of SEM photographs of the grooves before heating, and Figs. 2.2(a)-(b) show the grooves after heating at 720 °C for three hours, and Fig. 2.2(c) after heating for three hours at 670 °C. In contrast to Fig. 2.2(b), Fig. 2.2(c) shows only minute deformation in the shape of the groove. Conditions for mass transport were also studied in the terrace structure described above. After the mass transport process, a "burying layer" was "grown" next to the exposed quaternary layer, giving rise to a buried laser structure. Here, besides the temperature and duration, the process also depended on the thickness of the active layer. The width of the transported region was found to vary directly with temperature and duration but inversely with the thickness. Figs. 2.4 show the different widths under two rather different conditions, where the temperature and duration were 675 °C,

(a)

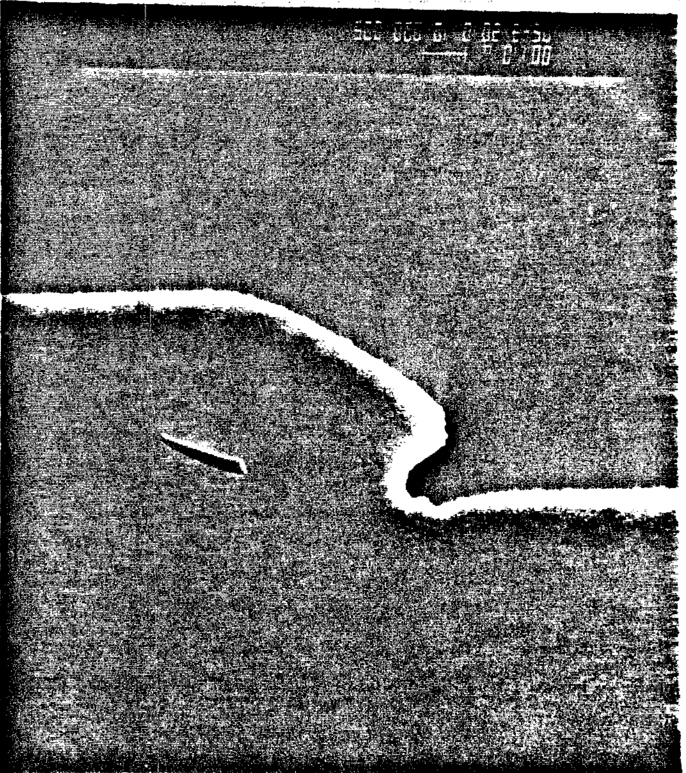

(b)

Figure 2.4 SEM pictures of the mass transported terrace structure: (a) lower temperature and shorter heating time; (b) higher temperature and longer heating time.

forty five minutes and 740 °C, 1.5 hour for 2.4(a) and 2.4(b) respectively. It can be seen that for lower temperature and shorter heating time, the mass transport process only occurred in the thin constricted etched region, where the vapor pressure could be higher. From Fig. 2.4(a), it was apparent that in the thin and constricted regions, the mass was transported from regions adjacent to the quaternary layer. When the wafer was exposed directly to the reducing atmosphere of the LPE system (without the InP cover wafer and graphite plate), mass transport also occurred next to the quaternary layer. However, thermal etching was observed in this case and large In droplets were found on the surface of the wafer. In view of this and the results of the experiments conducted in ampules described above, it seems that in the presence of the InP cover wafer and graphite plate, the vapor pressure was automatically adjusted to a condition suitable for mass transport. Moreover, the cover wafer and graphite plate also protect the substrates from problems of thermal etching. Thus, the cover wafer provides a convenient and practical way to obtain reproducible and controllable mass transport process.

2.3 Properties of p-n Junctions 'Grown' by Mass Transport Process

The properties and quality of a p-n junction are important factors influencing the performance of a semiconductor laser. Characteristics and effects of the transported region on laser performance will be described in the following sections. By etching away the quaternary layer completely in the terrace structure, an InP-InP homojunction results after mass transport. These junctions were then compared with the InP-InGaAsP junctions in both the cases with (InP-Q MT) and without (InP-Q NMT) a mass transported region grown next to the InGaAsP layer. In each of the three cases, characteristics of 6-8 diodes from the same wafer were measured and an average value was taken. Fig. 2.5 shows the typical

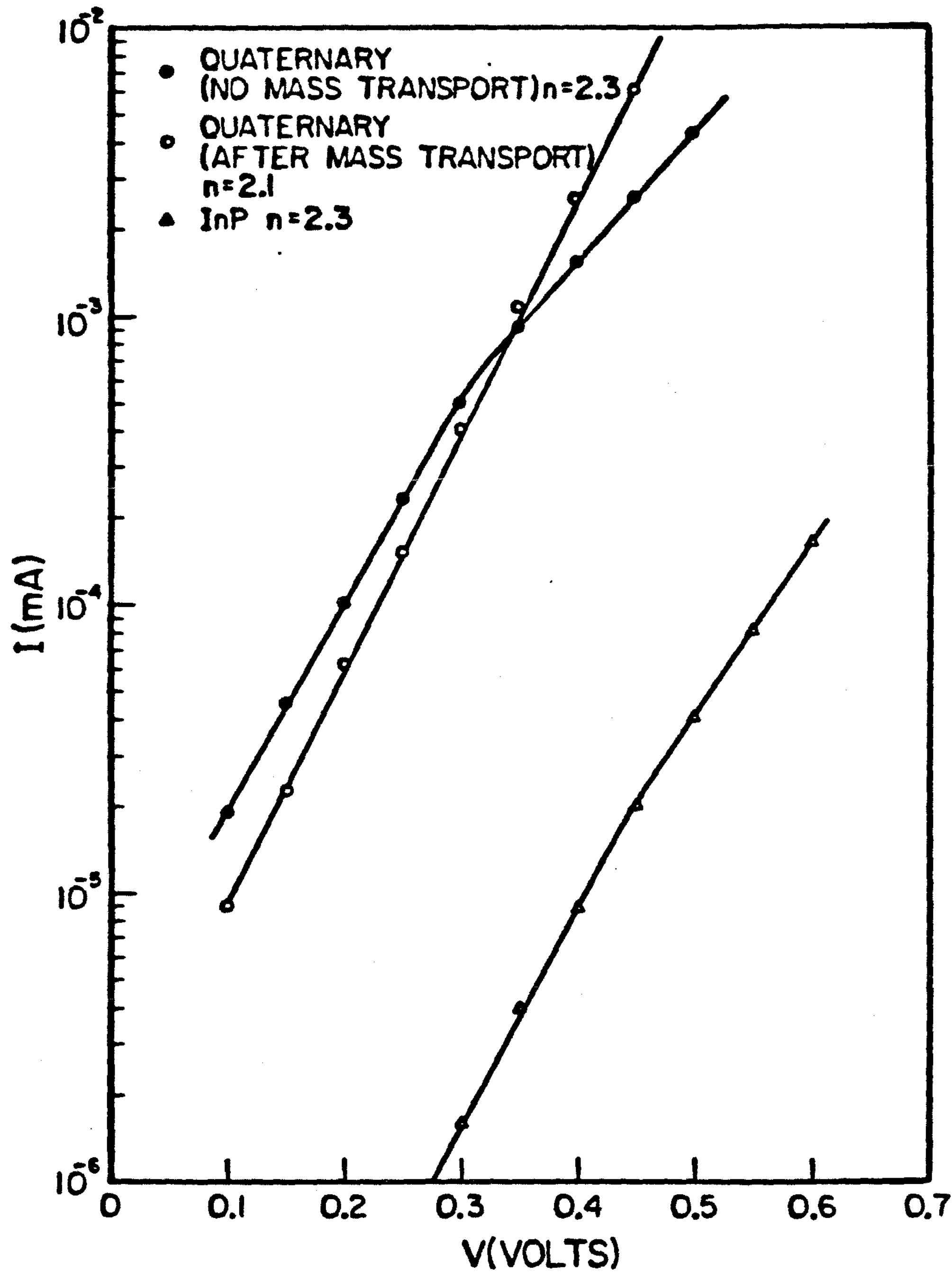

Figure 2.5 Forward I-V characteristics of the diodes.

forward I-V characteristic at low voltages. Assuming the diodes obey the equation

$$J = J_s\left(e^{\frac{eV}{nkT}} - 1\right) \tag{2.3.1}$$

where J and J_s are the current and reverse saturated current densities respectively, e the electronic charge and V the applied voltage. The values of n and J_s were found to be 2.3, $(1.2\pm 0.59)\times10^{-6}$ A/cm^2 (InP); 2.1, $(1.59\pm 0.57)\times10^{-4}$ A/cm^2 (InP-Q MT); and 2.3, $(1.58\pm 0.21)\times10^{-4}$ A/cm^2 (InP-Q NMT) respectively for the three cases. The values of n were indicative of generation-recombination dominated process. The deviation at higher voltages was due to the effect of the series resistance. In Fig. 2.6 is shown the curve tracer photograph where the difference in turn-on voltages for the hetero- and homojunctions was clearly displayed. The larger turn-on voltage for InP is a direct consequence of the much smaller J_s, which in turn is due to the smaller n_i (larger bandgap E_g), the intrinsic carrier concentration, of InP as compared with InGaAsP.

Fig. 2.7 shows a typical C-V characteristics of the three different types of diodes. The linear relationship of $1/C^2$ vs V justifies the classification of these as abrupt junctions. From these measurements, values of the built-in voltages (V_{bi}) and doping concentrations could be extracted. Assuming these to be one-sided abrupt junctions, the doping concentrations in the active layers were estimated to be $(1.0\pm 0.3)\times10^{17}$cm^{-3} (InP), $(1.5\pm 0.5)\times10^{18}$cm^{-3} (InP-Q MT) and $(5.0\pm 1.0)\times10^{17}$cm^{-3} (InP-Q nMT). These values are consistent with the approximate values calculated from the semi-empirical expression of Sze [2.4]

$$V_B = 60\left(\frac{E_g}{1.1}\right)^{\frac{3}{2}}\left(\frac{N}{10^{16}}\right)^{\frac{3}{4}} \tag{3.3.2}$$

where E_g is the bandgap energy in eV and N the concentration in cm^{-3}. The values of the reverse breakdown voltages were found to be 14 V (InP-InP), 1.8 V

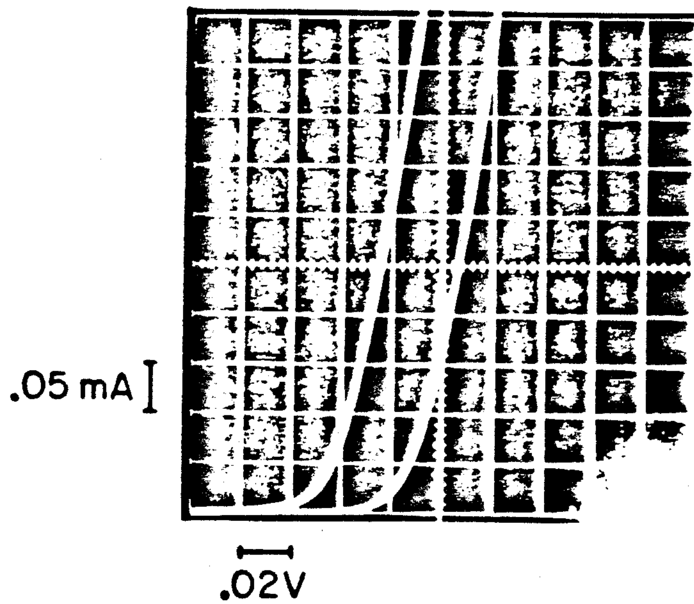

Figure 2.6 Curve tracer photograph showing the difference in I-V characteristics of the hetero- and homojunctions. The homojunction has a larger turn-on voltage.

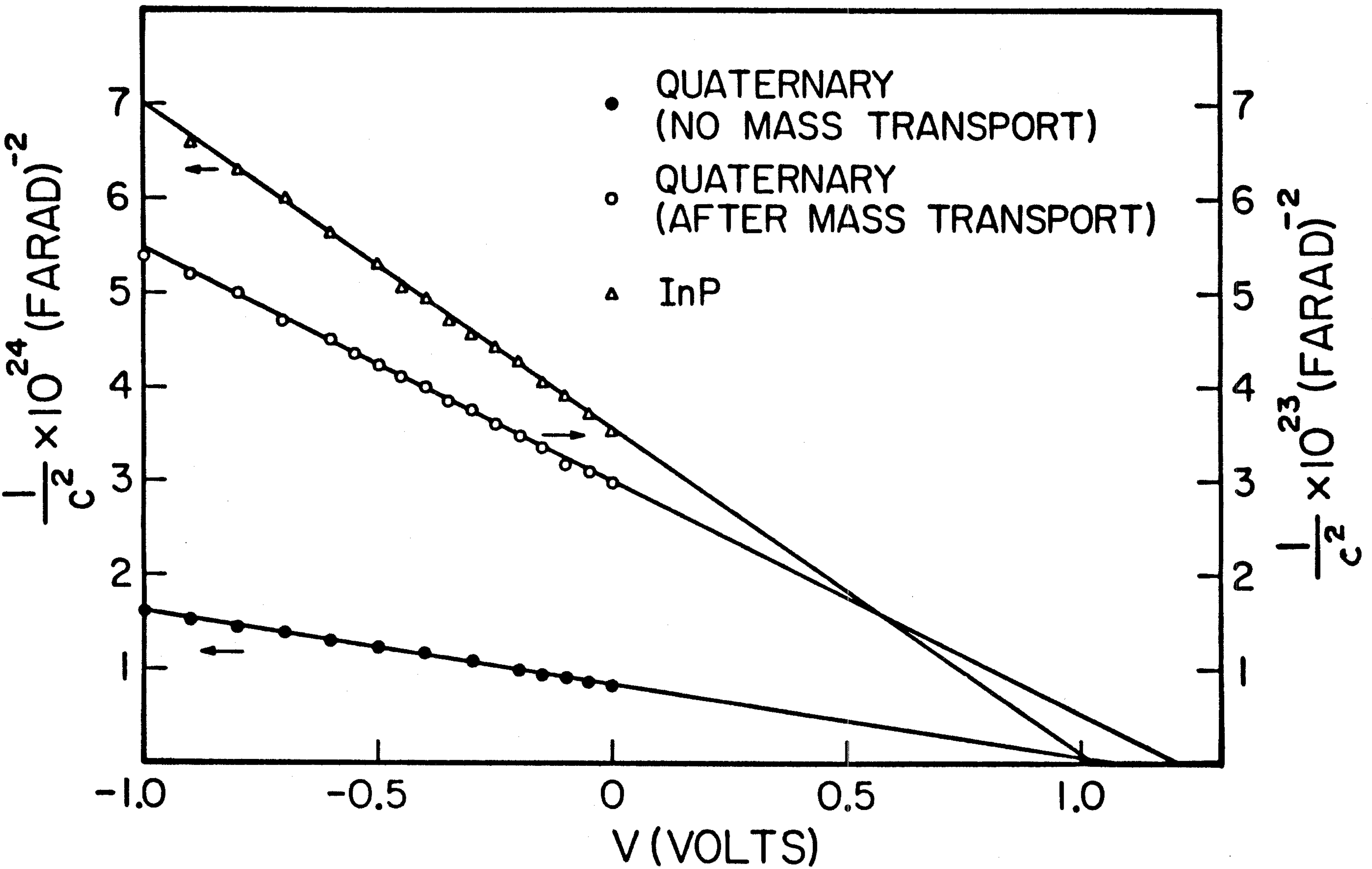

Figure 2.7 C-V characteristics of the diodes.

(InP-Q MT) and 3.6 V (InP-Q NMT). The higher doping concentration in the quaternary layer after heating is most probably due to the Zn diffusion from the cladding layer into the quaternary layer when the wafer was heated at around 675 °C during the transport process [2.5]. This has important consequences on the temperature sensitivity of laser thresholds, as will be explained in the next section and further elaborated in chapter 3.

The junction characteristics are summarized in Table 2.1. The InP mass transport homojunction is indistinguishable from grown junctions, indicating the high crystalline quality of the transported region.

2.4 Application and Effects on Laser Performance

The mass transport technique has been applied in laser fabrication, resulting in extremely low threshold lasers [2.2]. In the BH structure of [2.2], the otherwise necessary and critical regrowth process is completely eliminated. The mass transport technique can also find application in the fabrication of other devices, such as LED's and super-luminescent diodes, just to name a few. However, it should be mentioned that the mass transport process can also give rise to undesirable results. For example, in the fabrication of distributed feedback lasers, the corrugation grating on the substrate could be smeared due to the transport process, and special care has to be taken to prevent the transport process [2.6]. In this section, the low threshold terrace mass transport laser (T-MT) will be described and compared with the terrace mesa laser (T-ME) to probe the effects of mass transport on laser performance.

The terrace structure shown in Figs. 2.3 has been processd into low threshold lasers (Fig. 2.3(c)). Fig. 2.4(a) showed the SEM photograph of the cross-section of the T-MT laser. The T-ME's and T-MT's were identical in all respects except that the mass transport step was skipped in the T-ME's, resulting in active layers

Junction	InP-Q (NMT)	InP-Q (MT)	InP-InP (MT)
Type	Abrupt	Abrupt	Abrupt
n	2.3	2.1	2.3
J_s (A/cm^2)	$(1.58\pm 0.21)\times 10^{-4}$	$(1.59\pm 0.57)\times 10^{-4}$	$(1.2\pm 0.59)\times 10^{-6}$
$V_{turn-on}$ (V)	0.6-0.7	0.6-0.7	0.9-1
$V_{breakdown}$ (V)	3.6	1.8	14
$V_{built-in}$ (V)	1.1	1.2	1.0
N (cm^{-3})	$(5.0\pm 1.0)\times 10^{17}$	$(1.5\pm 0.5)\times 10^{18}$	$(1.0\pm 0.3)\times 10^{17}$

Table 2.1 Comparison of the properties of the InGaAsP-InP heterojunction and InP-InP homojunction.

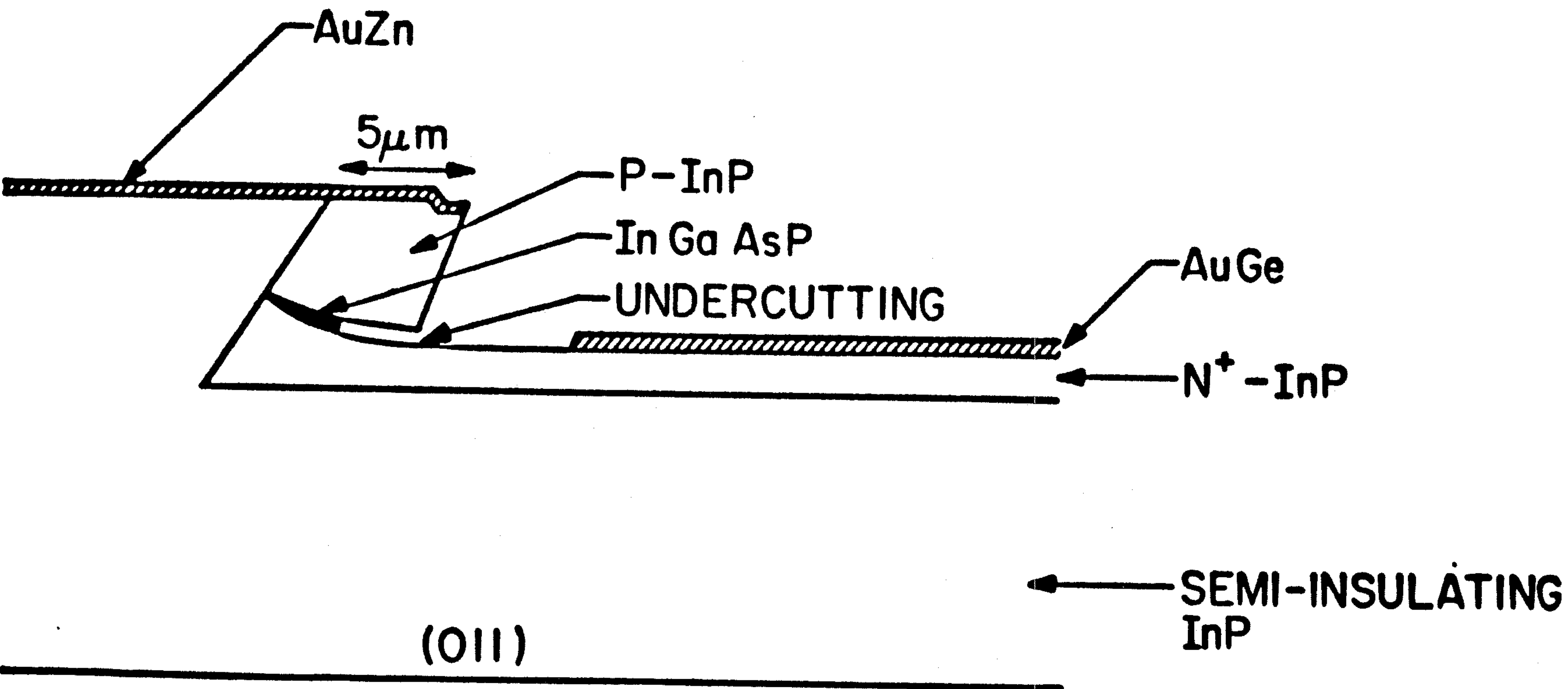

Figure 2.8 Schematic cross-section of the fabricated T-ME laser.

which were not "buried" and were exposed directly to air. Fig. 2.8 shows the schematic drawing of the T-ME laser. Since the only structural difference in these two lasers is the mass transported region in T-MT, the T-ME laser is thus a suitable structure for making a comparative study to investigate the effects of mass transport on laser performance.

The T-MT lasers with similar dimensions had threshold currents averaging around 20 mA, compared to 14 mA in the case of the air interface T-ME's. The average L-I characteristics of T-MT's are linear up to 4 I_{th}. The corresponding figure for the T-ME's is 7 I_{th}. Also, the T-ME's were found to have higher external quantum efficiencies than the T-MTs (35-45% vs 55-65%). Fig. 2.9 shows the L-I characteristics of typical T-MT and T-ME's. The far field patterns are shown in Fig. 2.10. Here the scattering from the exposed sidewall of the T-MEs is apparent. In addition, the T-ME's were found to be less temperature sensitive. Using the empirical relation for the temperature dependence of threshold current

$$I_{th} = I_o e^{\frac{T}{T_o}} , \qquad (3.4.1)$$

the T_o's for the TM-E and T-MT lasers were found to lie in the range of 60–70 °K and 40–50 °K respectively. The lower T_os of the T-MT's could be explained by the larger electron leakage over the InGaAsP/InP heterobarrier due to lower doping level in the cladding layer as a result of zinc out diffusion during the heating period of the mass transport process. This leads us into the subject of the temperature dependence of quaternary lasers treated in detail in the next chapter, where further experimental evidence as well as theoretical model calculations provide a coherent interpretation of the difference in T_o's of the T-ME and T-MT lasers.

The comparison of the characteristics of the T-MT and T-ME lasers is summarized in Table 2.2 It should be stressed that though T-ME lasers appear to be

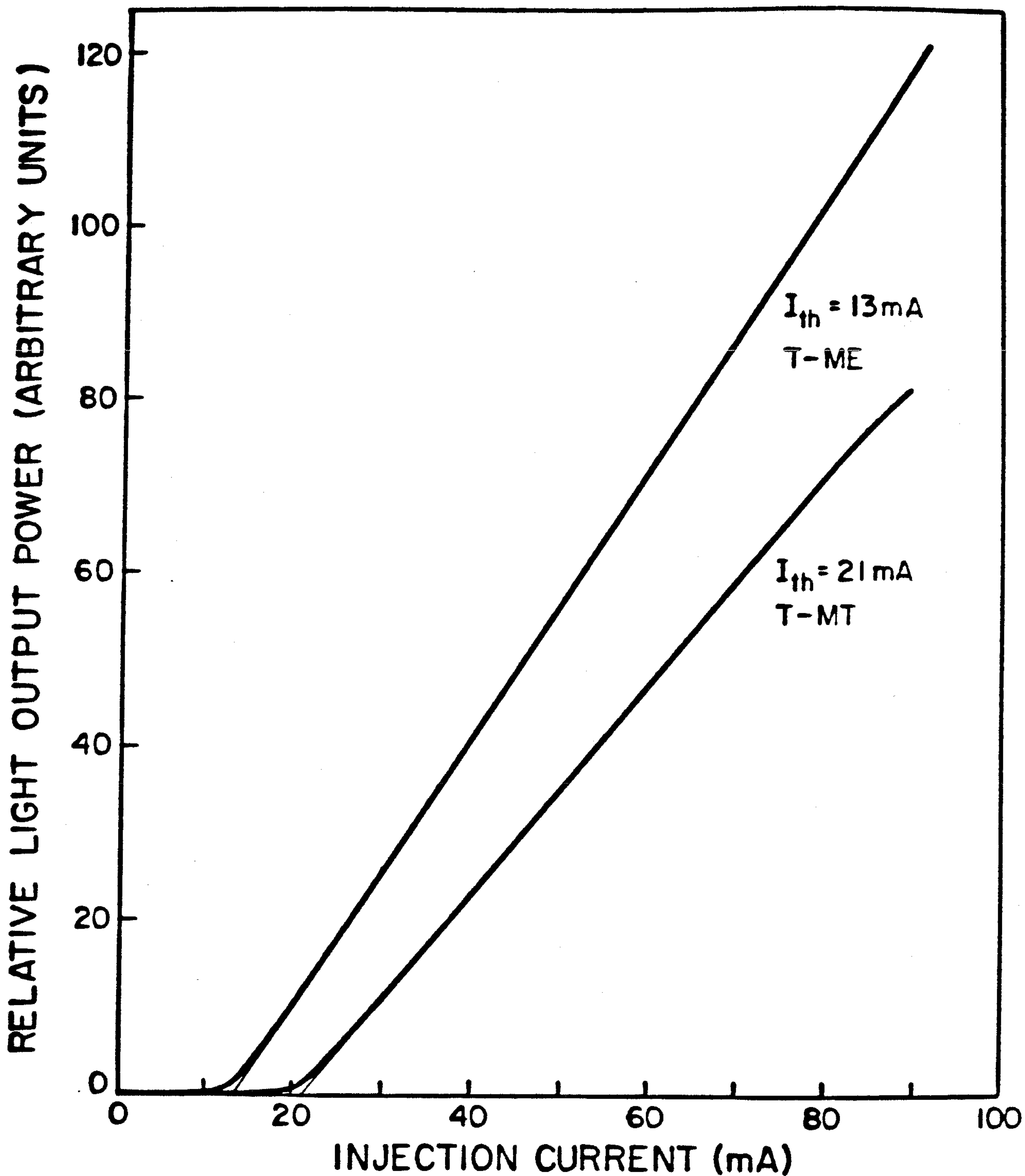

Figure 2.9 L-I characteristics of typical T-MT and T-ME lasers.

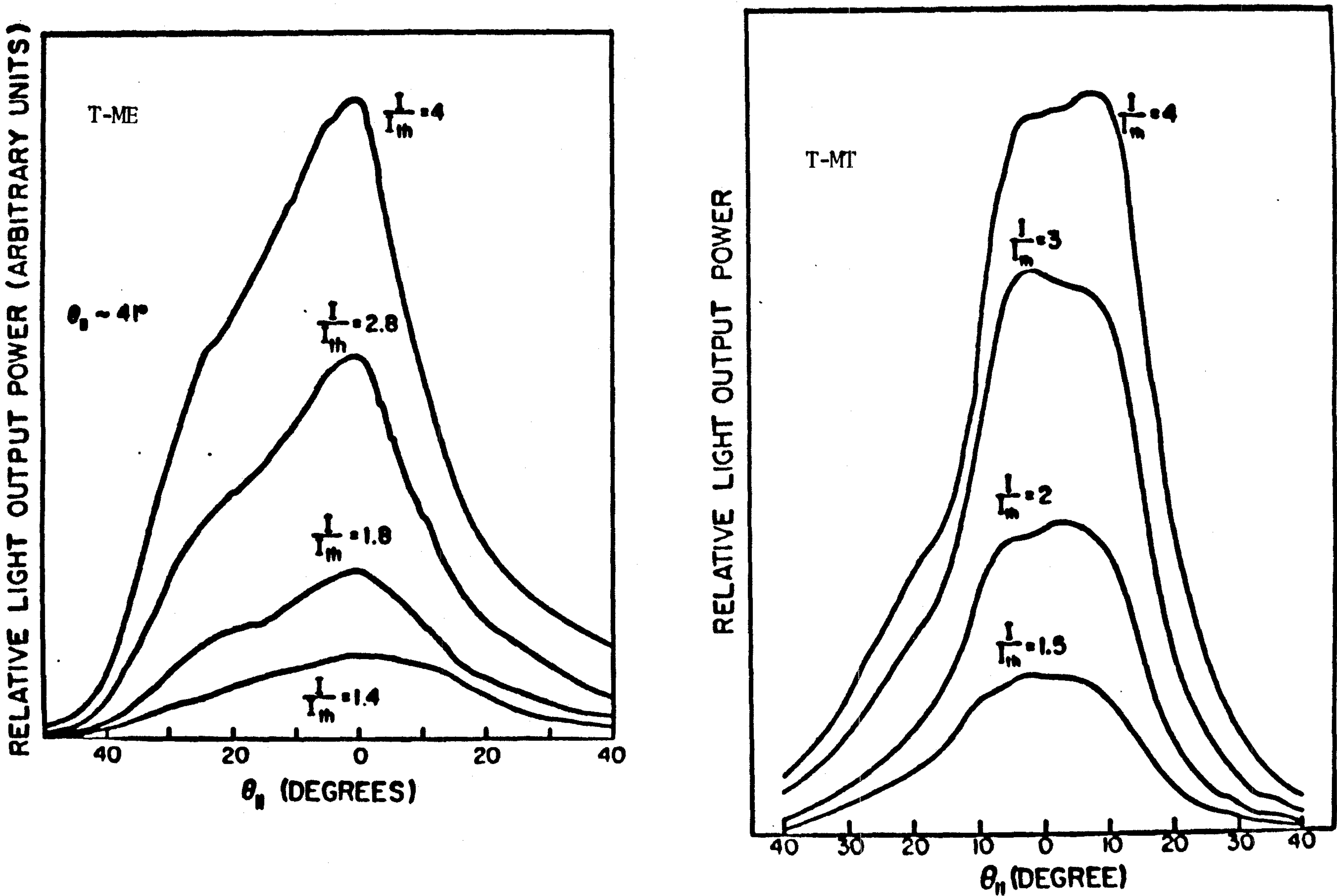

Figure 2.10 Far field patterns of the T-ME and T-MT lasers.

-	T-ME	T-MT
I_{th} (mA)	14	20
L-I linearity	up to 7 I_{th}	up to 4 I_{th}
η^{*} (%)	55-65	35-45
T_o (°K)	60-70	40-50

* external differential quantum efficiency.

Table 2.2 Comparison of the characteristics of the T-MT and T-ME lasers

superior, the exposed unpassivated InGaAsP surface leads to higher surface scattering loss and an irregular asymmetric far field pattern (Fig. 2.10(a)). More importantly, surface passivation is essential for the long term stability of lasers. Thus the mass transport process offers an excellent way to passivate the surface.

References - Chapter 2

2.1 Z. L. Liau and J. N. Walpole, Paper WB 3, Technical Digest, Topical Meeting on Integrated and Guided Wave Optics, Optical Society of America (1982)

2.2 Z. L. Liau and J. N. Walpole, Appl. Phys. Lett., **40** , p. 568 (1982)

2.3 J. W. Cahn, and D. W. Hoffman, Acta Metallurgica, **22** , p. 1205, (1974)

2.4 S. M. Sze, 'Physics of Semiconductor Devices," Chap. 2, J. Wiley and Sons, New York (1981)

2.5 C. B. Su, J Schlafer, J. Manning, and R. Olshansky, Elect. Lett., **18** , p. 595, (1982)

2.6 K. Utaka, private communication.

Chapter 3
Temperature Dependence of the Threshold Current of InGaAsP Double Heterostructure Lasers

3.1 Introduction

Semiconductor injection lasers using the quaternary compound InGaAsP as active layers generally exhibit threshold current densities that depend strongly on temperature. Empirically, the temperature dependence of the threshold current of all semiconductor lasers can be expressed in the form

$$I_{th} = I_o \, e^{\frac{T}{T_o}} \tag{3.1.1}$$

where I_o is a constant, T is the temperature, and T_o is a characteristic temperature that measures the temperature sensitivity of the laser. InGaAsP lasers are characterized by a low T_o ranging from 50-80 °K for temperatures above ~ 220 °K. This value is considerably lower than that of GaAlAs/GaAs lasers, which is typically greater than 120 °K. A typical plot of ln I_{th} vs T for the GaAlAs/GaAs and InGaAsP/InP systems is shown in Fig. 3.1. For InGaAsP lasers, the temperature beyond which the T_o drops drastically is termed the "break-point" temperature.

Also, in InGaAsP light emitting diodes (LEDs), the output power saturates at high injection current densities. The excess temperature sensitivity in lasers and severe output power saturation in LEDs remain the two unsolved problems. The underlying mechanisms in the two cases are believed to be the same. Hitherto, many mechanisms, including in plane superluminescence [3.1], inter-facial

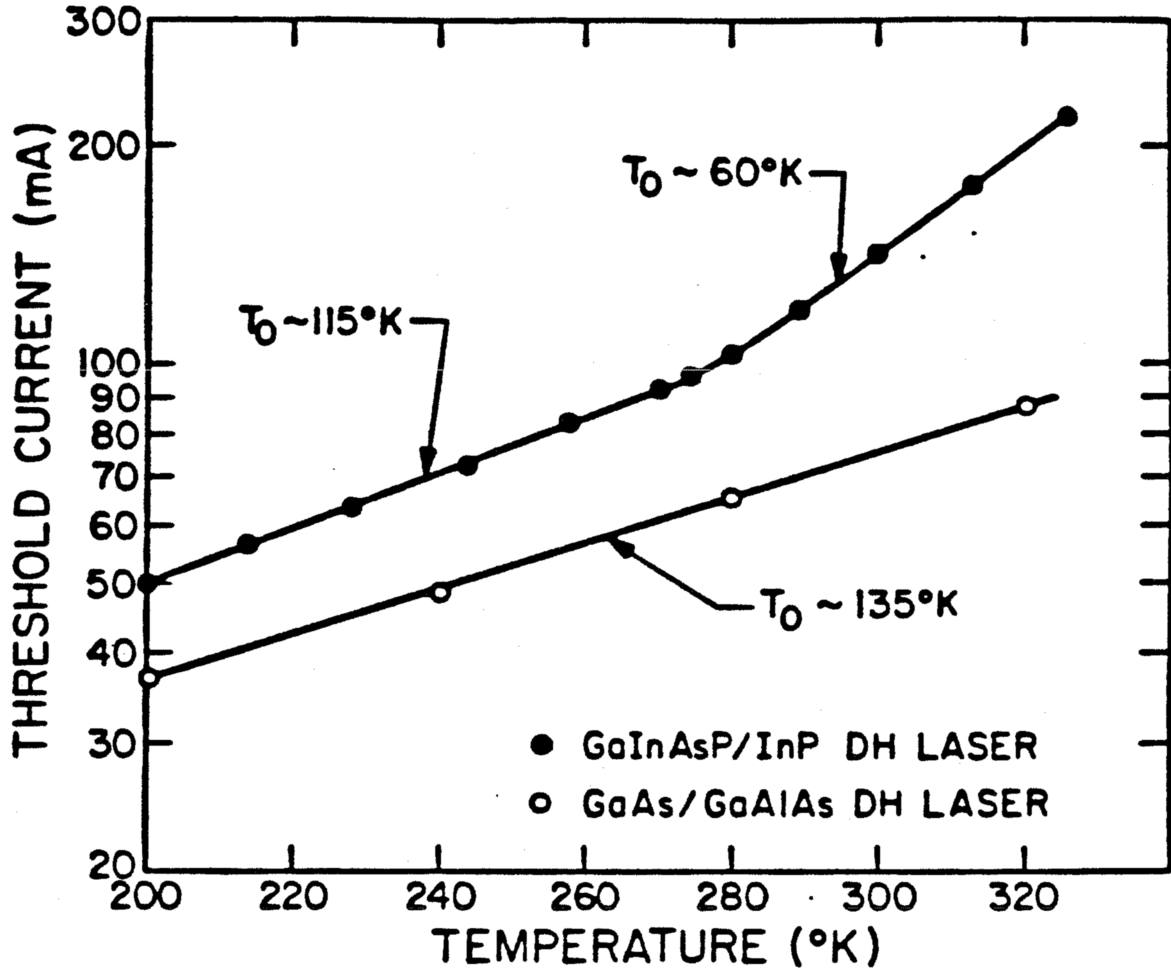

Figure 3.1 Typical plot of ln I_{th} vs T for the GaAlAs/GaAs and InGaAsP/InP lasers.

recombination [3.2], inter-valence band absorption [3.3], non-radiative recombination via traps [3.4], non-radiative Auger recombination [3.5,3.6,3.7,3.8], and carrier leakage [3.9,3.10,3.11] have been proposed to explain the phenomena. Among the various mechanisms listed above, the non-radiative Auger recombination and carrier leakage over the heterobarrier are believed to be the dominating factors. The importance of these two factors will be studied in this chapter.

In the following sections, the non-radiative Auger recombination and carrier leakage will be discussed. Theoretical calculations and models will be compared with experimental results. In addition, Auger recombination in quantum well lasers will also be discussed briefly.

3.2 Interband Auger Recombination in InGaAsP

It is well known that non-radiative Auger recombination processes become significant in low bandgap semiconductors at high temperatures [3.12,3.13]. Figs. 3.2 show the two dominant Auger processes. In the CHCC process, an electron (1) in the conduction band recombines non-radiatively with a hole (1') in the heavy hole band, and the excess energy is imparted to another electron (2) with the appropriate momentum (Fig. 3.2(a)). In the CHSH process, the energy and momentum is taken up by a hole which is excited from the heavy hole band to the split-off hole band (Fig. 3.2(b)).

The theory of Auger recombination in semiconductors was first developed by Beattie and Landsberg [3.12]. The transition probability is obtained from first order perturbation theory by employing Fermi's Golden Rule with a screened Coulomb interaction Hamiltonian given by

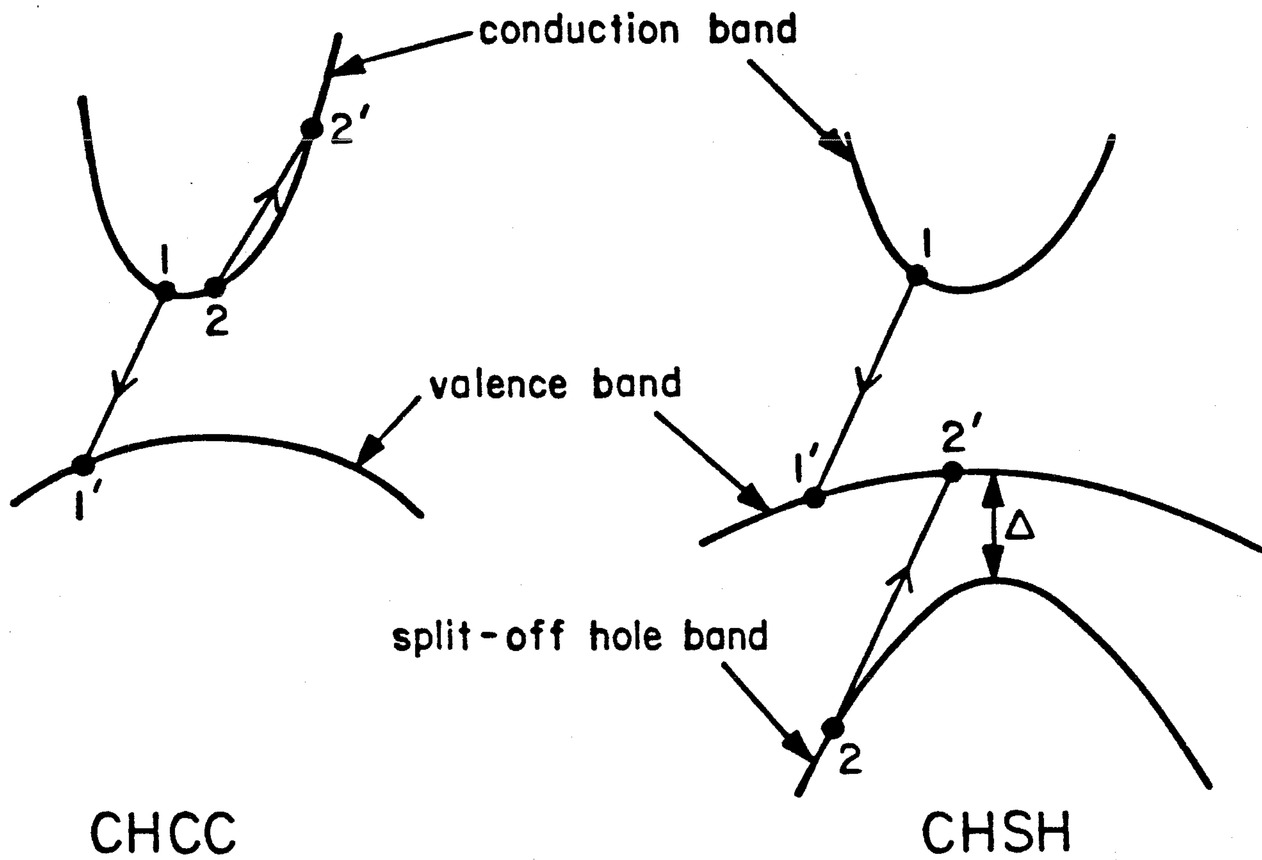

Figure 3.2 The CHCC and CHSH Auger recombination processes. 1,2 and 1', 2' are the initial and final states, respectively.

$$H' = \frac{e^2}{4\pi\varepsilon} e^{-\frac{|\vec{r}_2 - \vec{r}_1|}{L_D}} \frac{1}{|\vec{r}_2 - \vec{r}_1|} \tag{3.2.1}$$

In the above, e is the electronic charge, ε the static dielectric constant, and L_D is the screening length calculated from

$$L_D^{-2} = \frac{e^2}{\varepsilon kT} \frac{2}{(2\pi)^3} \int f(k)\,(1 - f(k))\,d\vec{k} \tag{3.2.2}$$

Here, f is the Fermi factor given by

$$f_i = \frac{1}{1 + \exp\left(\frac{E_i - E_f}{kT}\right)} \tag{3.2.3}$$

where k is the Boltzman constant, T the temperature, and E_f the Fermi level. Taking the electron wavefunctions as Bloch states,

$$\varphi_{c,v}(\vec{k},\vec{r}) = u_{c,v}(\vec{k},\vec{r})\, e^{i\vec{k}\cdot\vec{r}} \tag{3.2.4}$$

where c and v denote conduction and valence band respectively; the matrix element is then given by [3.12,3.13]

$$H'_{if} = \frac{e^2}{\varepsilon V} \frac{F_{nn'}\,F_{mm'}}{|\vec{k}_i - \vec{k}_f|^2 + L_D^{-2}} \tag{3.2.5}$$

In deriving (3.2.5), the Umklapp processes, which can be shown to be negligible [3.12], have been neglected. The overlap integrals $F_{nn'}$ are given by

$$F_{nn'}(\vec{k},\vec{k}') = \int u_n^*(\vec{k},\vec{r})u_{n'}(\vec{k}',\vec{r})\,d\vec{r} \tag{3.2.6}$$

The transition rate can then be expressed as [3.13]

$$P = \frac{2\pi}{\hbar}(2\beta)2\left(\frac{V}{(2\pi)^3}\right)^3\left(\frac{e^2}{\varepsilon V}\right)^2 \iiint \frac{|F_1F_2|^2}{(\,|\vec{k}_1 - \vec{k}_{1'}|^2 + L_D^{-2}\,)^2}$$

$$\times\ [f_1f_2(1-f_{1'})(1-f_{2'}) - (1-f_1)(1-f_2)f_{1'}f_{2'}]\,\delta(E_f - E_i)\,d\vec{k}_1 d\vec{k}_{1'} d\vec{k}_{2'} \tag{3.2.7}$$

In the above, $E_{f,i}$ are the energies of the particles before and after the interac-

tion respectively, and $2<\beta<3$ due to spin symmetry. The overlap integral $|F_1F_2|^2$ has been derived using the $\vec{k}\cdot p$ method [3.14]. For the CHCC process [3.14],

$$|F_1F_2|^2 \approx \frac{\hbar^2}{2m_o E_g} f_{cv} \, |\vec{k}_1 - \vec{k}_{1'}|^2 \tag{3.2.8}$$

and for CHSH process,

$$|F_1F_2|^2 \approx \alpha_{ch} \, \alpha_{sh} \, \frac{|\vec{k}_1 - \vec{k}_{1'}|^2}{E_g^{\,2}} \tag{3.2.9}$$

with

$$\alpha_{ch} = \frac{\hbar^2}{2m_o} \frac{E_p}{3E_g} \tag{3.2.10}$$

and

$$\alpha_{sh} = \frac{\hbar^2}{2m_o} \frac{E_p}{3\Delta\,(\Delta + E_g)} \frac{\hbar^2\,|\vec{k}_2 - \vec{k}_{2'}|^2}{2m_s} \tag{3.2.11}$$

Here, E_g is the bandgap, Δ the spin-orbit splitting, f_{cv} the oscillator strength, m_o the electron mass, m_s the split-off hole mass, and E_p is a band parameter related to the momentum matrix element [3.15]. Since semiconductor lasers operate under high injection condition which renders the conduction band degenerate, the full Fermi factors (3.2.3) must be used. Unfortunately, use of degenerate statistics renders the analytic integration of (3.2.7) impossible, and the rate P is thus calculated numerically assuming parabolic bands. The Auger lifetime is obtained from the expression

$$\tau_A = \frac{\Delta n}{P} \tag{3.2.12}$$

where Δn is the injected carrier density at threshold. It is assumed that the injection level is high, so that $\Delta n \approx n_{th}$, an excellent assumption for semiconductor lasers. Data from lasers emitting at 1.1, 1.27, 1.3, and 1.48 μm are taken from references 3.16, 3.5, 3.6, and 3.17 respectively. The band parameters used

in the calculation are listed in Table 3.1. For comparison, the calculated and experimental carrier lifetime at 300 °K are listed in Table 3.2. The total carrier lifetime is obtained from the sum of the radiative and Auger effects by

$$\frac{1}{\tau} = \frac{1}{\tau_{rad}} + \frac{1}{\tau_{chcc}} + \frac{1}{\tau_{chsh}} \tag{3.2.13}$$

The radiative lifetime is obtained by extrapolation of experimental values at low temperatures. As is evident from Table 3.2 and Figs. 3.3-3.6, reasonable agreement was obtained for lasers with low nominal threshold current densities. For lasers with high nominal current densities, the calculated Auger lifetimes are significantly shorter than the observed values. This is due to the high apparent carrier concentration resulting form the high threshold current density, which indicates the existence of additional loss mechanisms not accounted for here. It should be cautioned that the Auger lifetime is a rather sensitive function of carrier concentration as shown in Fig. 3.7, and calculated lifetimes are meaningful only if reliable values of n_{th} are available.

The Auger lifetime is known to vary approximately with the carrier concentration as

$$\frac{1}{\tau} \sim n^a \tag{3.2.14}$$

where a is between 2 and 4. Fig. 3.7 shows the relationship of $\frac{1}{\tau}$ and n for a 1.3 μm laser at 300 °K. From Fig. 3.7, it is deduced that a = 2.19 for CHCC process and 2.04 for the CHSH process. This compares favorably with the value of 2.2 obtained on LED experiments by Uji et al [3.18]. The apparently slight deviation of a from 2 can be very significant at high injection conditions where $n \sim 10^{18}$ cm^{-3}. Usually, the Auger process is also expressed in terms of the Auger coefficient C defined as

Symbol	$In_{1-x}Ga_xAs_yP_{1-y}$
E_g	$1.34 - .72y + .12y^2$
ε	$x\varepsilon_{GaAs} + (y-x)\varepsilon_{InAs} + (1-y)\varepsilon_{InP}$
$\frac{m_c}{m_o}$	$0.08 - 0.39y$
$\frac{m_h}{m_o}$	$(1-y)(.79x + .45(1-x)) + (.45x + .4(1-x))y$
$\frac{m_s}{m_o}$	$.17x + .083(y-x) + .15y$
Δ	$.11 + .421y - .152y^2$

For lattice matching to InP, $x=.4526y/(1-.031y)$

Table 3.1 Band parameters used in the calculation.

Wavelength (μm)	J_{th}/d (kA/cm$^2\mu m$	τ_{exp} (ns)	τ_{cal} (ns)
1.1	-	4.0	4.2
1.27	14.0	2.0	1.4
1.3	9.0	2.3	2.0
1.48	7.6	1.7	2.0

Table 3.2 Comparison of experimental and calculated carrier lifetimes for InGaAsP lasers at 300 °K.

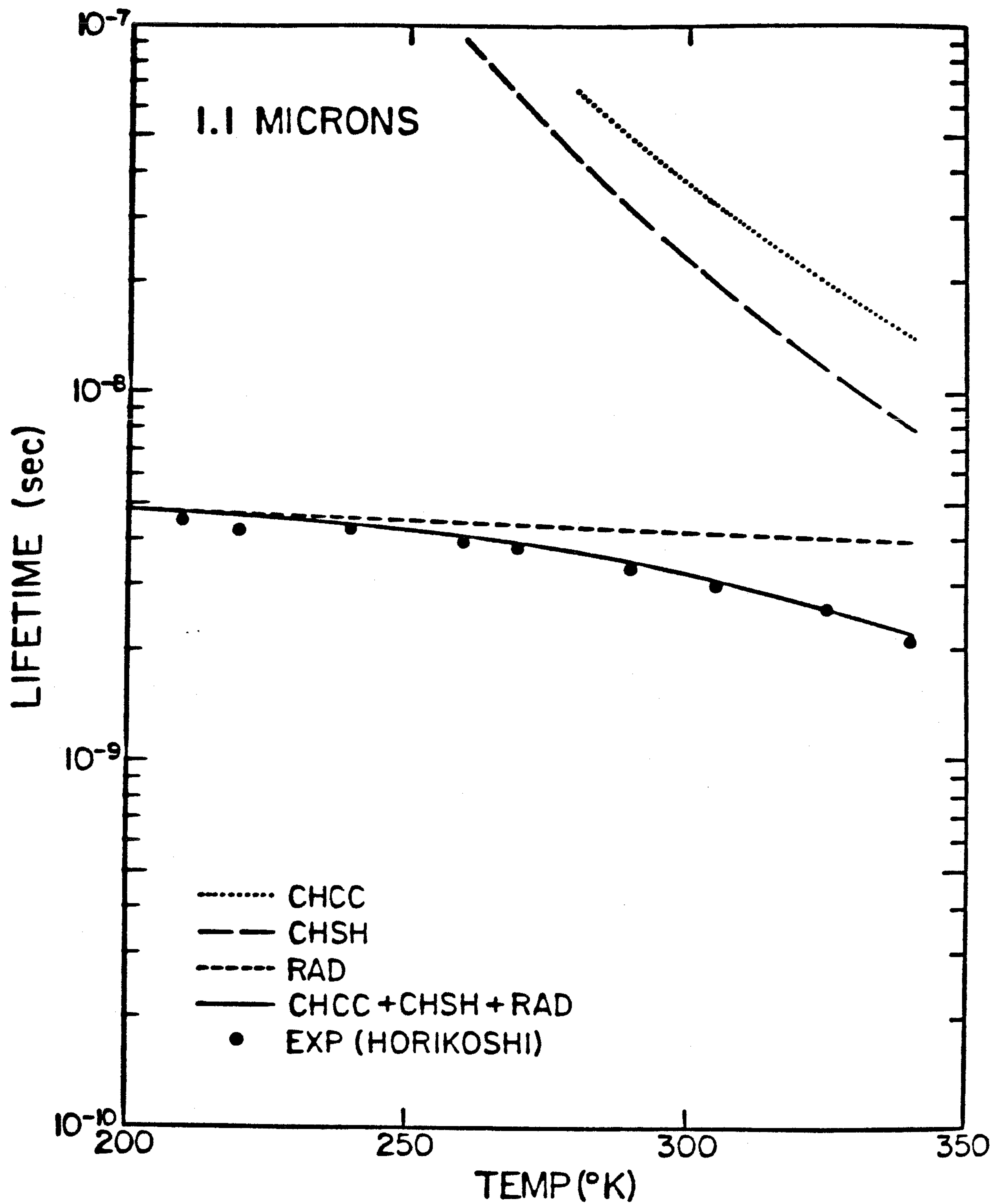

Figure 3.3 Calculated and measured lifetimes of 1.1 μm laser. Data taken from [3.16].

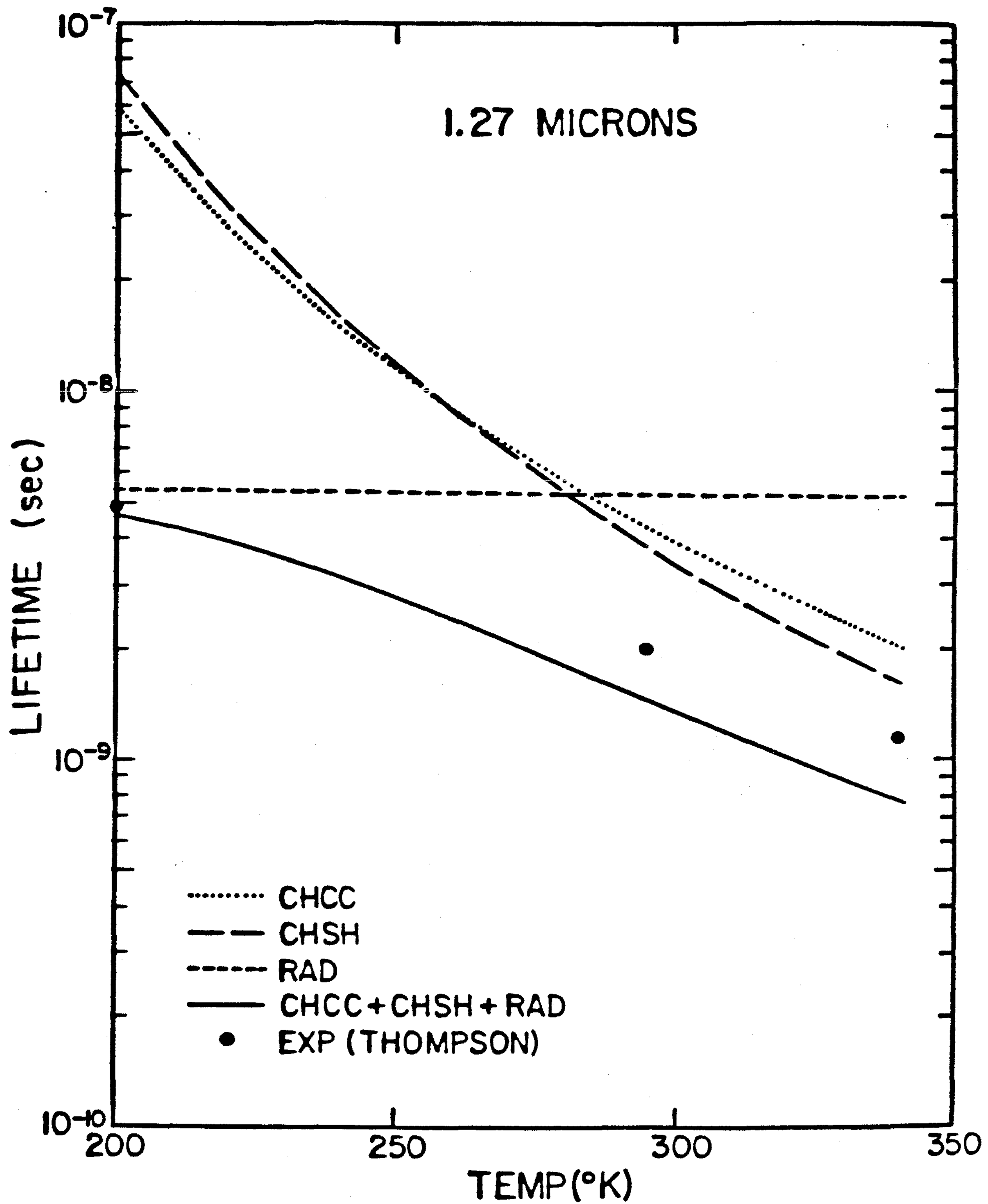

Figure 3.4 Calculated and measured lifetimes of 1.27 µm laser. Data taken form [3.5].

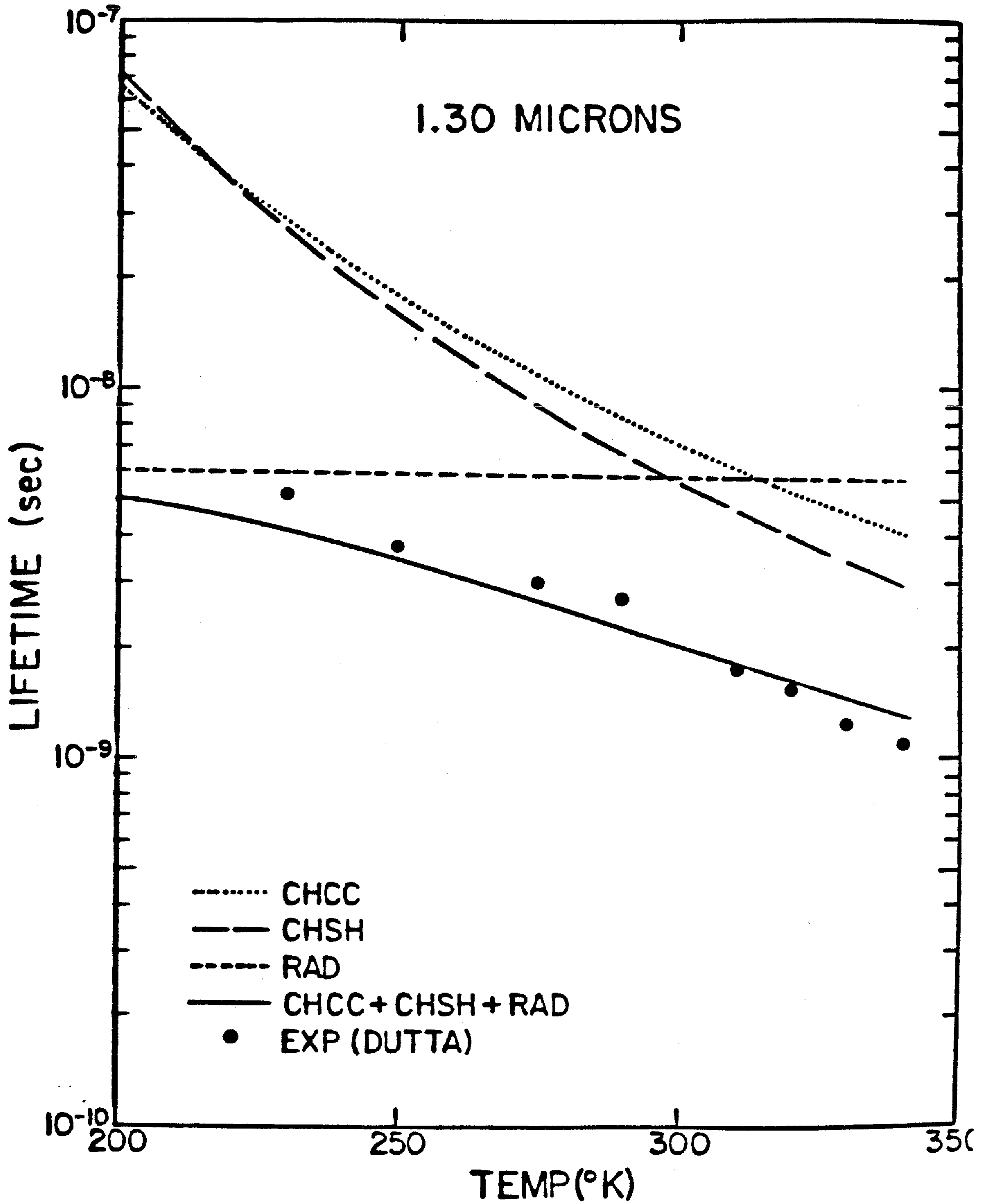

Figure 3.5 Calculated and measured lifetimes of 1.3 μm laser. Data taken from [3.6].

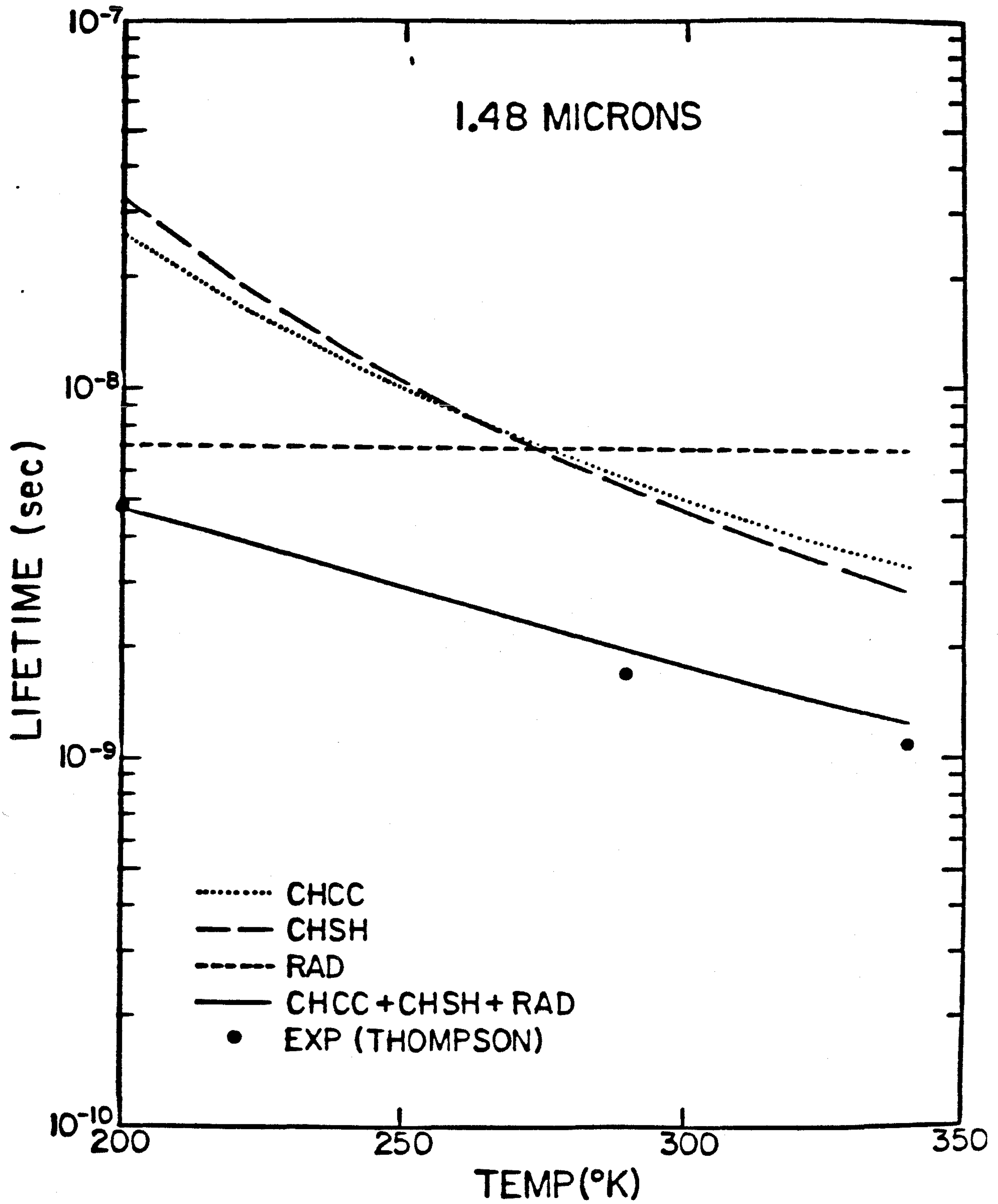

Figure 3.6 Calculated and measured lifetimes of 1.48 μm laser. Data taken from [3.17].

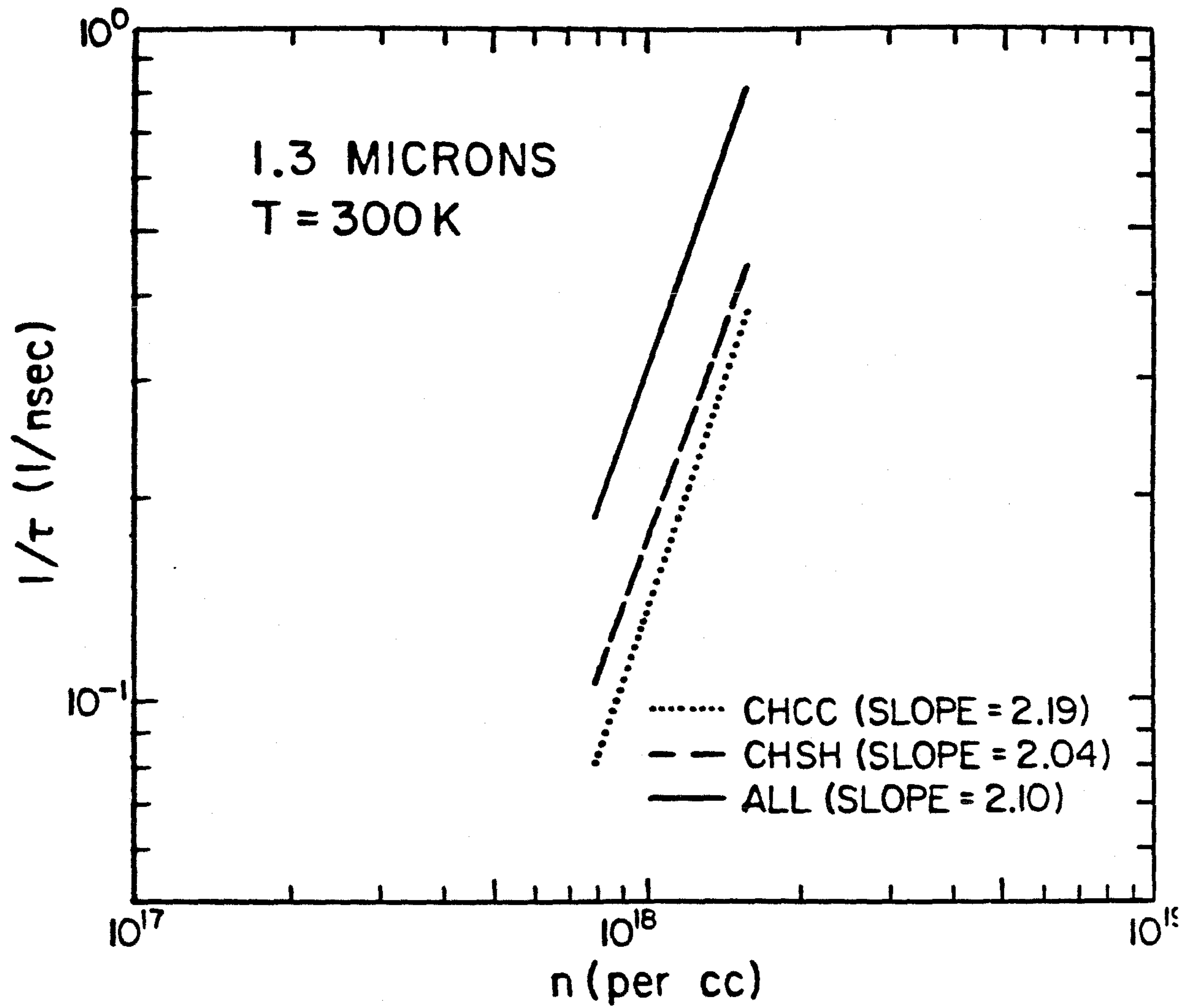

Figure 3.7 The inverse of Auger lifetime as a function of carrier concentration for a 1.3 μm InGaAsP laser at 300 oK.

$$\frac{n}{\tau} = C\,n^{b} = Cn^{1+a} \tag{3.2.15}$$

The values of C can be obtained from plots like Fig. 3.7.

The results of this section indicate the importance of non-radiative Auger recombination in InGaAsP lasers. However, it should be noted that non-radiative Auger recombination cannot explain the decrease in differential quantum efficiency in these lasers. This indicates the existence of other loss mechanisms. In the remainder of this chapter, the role played by carrier leakage will be discussed in detail, and the possible relationship between Auger recombination and carrier leakage will be discussed and employed to provide a more complete picture of the mechanisms leading to the low T_0.

3.3 Nature of Electron Leakage in InGaAsP/InP Double Heterostructures

Recently, the experiments of Yamakoshi et al [3.19,3.20] have demonstrated indirectly that electron leakage over the heterobarrier in InGaAsP LEDs is significant. In their structure, the electrons that leak over the heterobarrier recombine in another "leak detection" quaternary layer emitting at a shorter wavelength of 1.05 μm. The significant intensity of light at 1.05 μm serves as an indication of electron leakage.

In [3.20], the authors ruled out the non-radiative Auger recombination as the source of electron leakage on the basis that the dominant Auger process is the CHSH process. The end product of such process is an energetic hole and not electron. However, as can be seen from the previous section, the rate of the CHCC and CHSH processes are comparable in the quaternary system. Since the CHCC process creates an energetic electron, it can lead to electron leakage through the hot Auger electrons. It is found that such non-radiative recombination could also explain the observation of Yamakoshi's experiments, and the

nature of the electron leakage should be further investigated.

The total current through the LED can be written as [3.18]

$$I = I_R + I_{NR} = \frac{neSd}{\tau_{tot}} \tag{3.3.1}$$

where n is the electron density, S the area and d the thickness of the active region respectively, and τ_{tot} is given by (3.2.13). Therefore,

$$I_R = \frac{neSd}{\tau_{rad}} \tag{3.3.2}$$

and

$$I_{NR} = \frac{neSd}{\tau_{chcc}} + \frac{neSd}{\tau_{chsh}} \tag{3.3.3}$$

where I_R and I_{NR} denote radiative and non-radiative currents respectively. Since I/eSd is known from [3.20], we obtain the values of n/τ_{tot}. A self consistent approach is used to obtain n and τ_{tot}. Values of n are varied to calculate the Auger lifetimes for both the CHCC and CHSH processes until the value of n/τ_{tot} agrees with the experimental value of I/eSd. A typical value of 6 nsec [3.18] has been assumed for the radiative lifetime. It is noted that since the "leak detection" layer is much thicker than the 1.3 μm layer, the electron concentration in this layer is much smaller. As a result, the Auger lifetime is much longer than the radiative lifetime. Therefore, further electron leakage due to the Auger processes need not be considered for this layer.

If all "Auger electrons" leak out, the ratio of the light intensity at 1.3 μm and 1.05 μm would simply be given by

$$\frac{I_{1.3}}{I_{1.05}} = \frac{\tau_{chcc}}{\tau_{chsh}} \tag{3.3.4}$$

However, not all Auger electrons leak out, and if we assume that only a fraction β does leak out, the ratio of intensities becomes

$$\frac{I_{1.3}}{I_{1.05}} = \frac{\tau_{chcc}}{\beta \tau_{chsh}} \tag{3.3.5}$$

For the above to agree with the experimentally measured values of $I_{1.3}/I_{1.05}$, the required β's have been found to lie between 0.18 and 0.24. In Fig. 3.8 and 3.9, the measured intensity ratio as obtained from [3.20] is shown together with the calculated ratio of τ_{chcc}/τ_{rad} and $\tau_{chcc}/\beta\tau_{rad}$, where an average value of 0.22 has been used for β throughout. Since a single value of β is sufficient to bring about agreement between experiment and calculation, it gives a good indication that the electron leakage may be intimately related to the Auger process. Note that the CHCC process acts as a generating source of hot carriers, and carrier heating effects may then be important factors governing the current leakage. Evidence and a theoretical model of hot carrier enhanced leakage will be treated in the following sections.

3.4 Carrier Leakage in InGaAsP/InP Heterostructure—Experiment

Although the experiments of Yamakoshi et al [3.19,3.20] have demonstrated that there is significant carrier leakage over the hetero-barrier in 1.3 and 1.5 μm LEDs, the experimental evidence obtained is nevertheless indirect. In contrast, we have fabricated a laser-transistor structure to measure directly the electron and hole leakages over the InGaAsP/InP heterobarrier. The results show quantitatively the existence of a considerable amount of minority carrier leakage in the present laser structure ($\lambda = 1.2\,\mu$m) and that the leakage tends to increase with the injection current, even beyond the lasing threshold.

A schematic representation of the laser-bipolar-transistor used is shown in Fig. 3.10. The emitter-base junction functions as in an ordinary laser diode. The collector-base junction is reverse biased, as in a bipolar transistor, to collect the leakage current. The laser part of the transistor is similar to that of a terrace

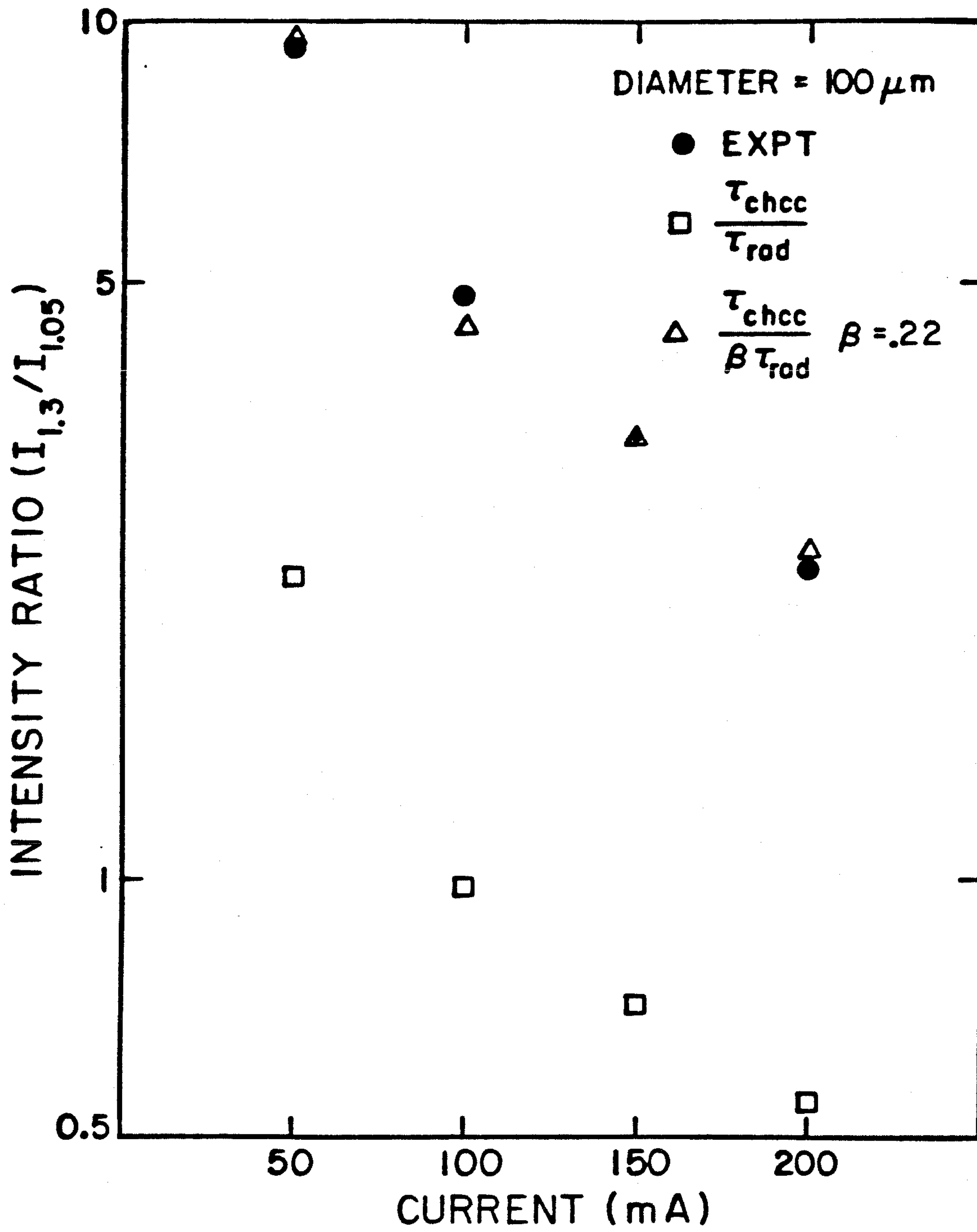

Figure 3.8 **Measured and "calculated" intensity ration $I_{1.3}/I_{1.05}$ for LED of diameter 100 μm.**

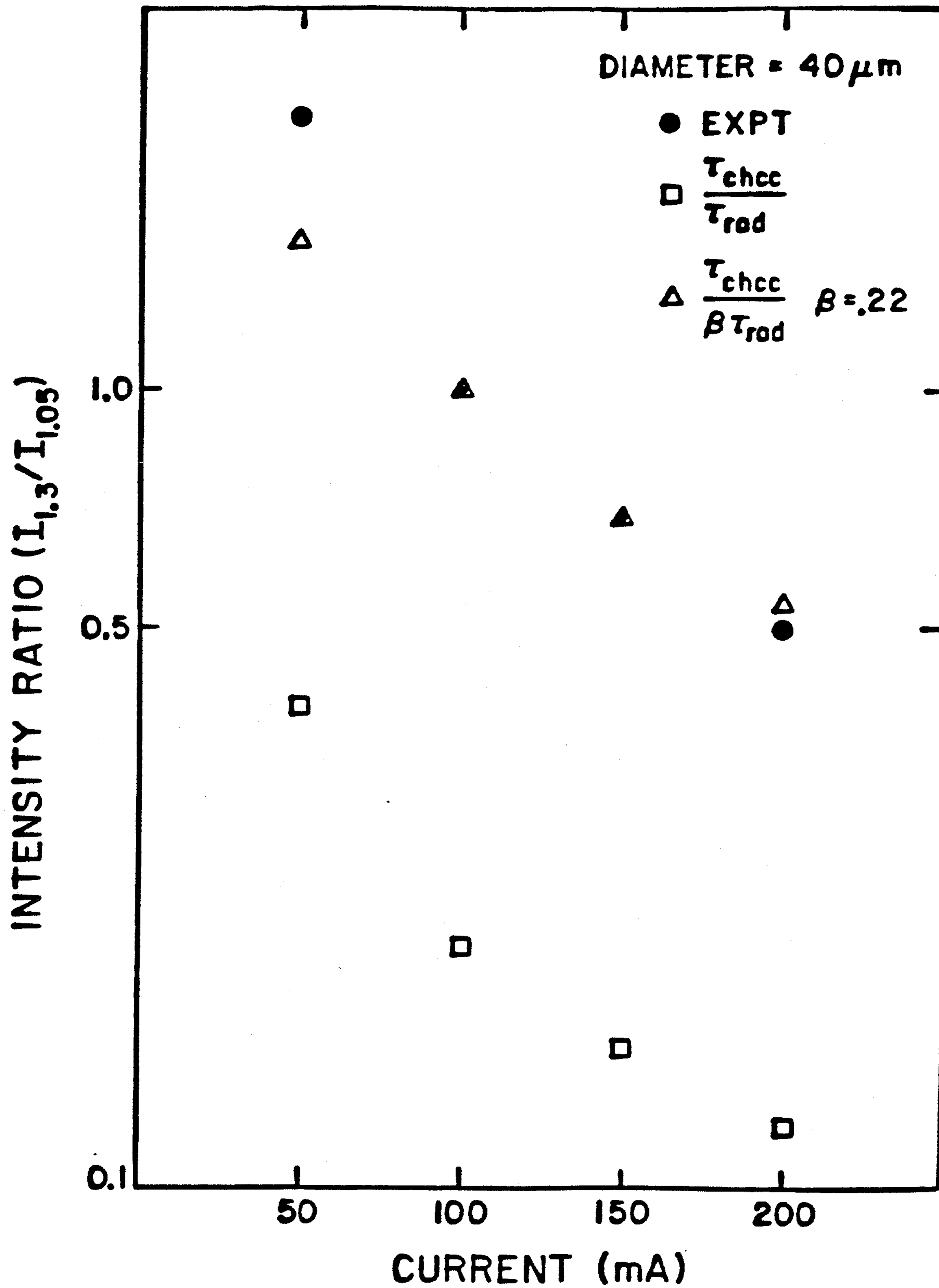

Figure 3.9 Measured and "calculated" intensity ration $I_{1.3}/I_{1.05}$ for LED of diameter 40 μm.

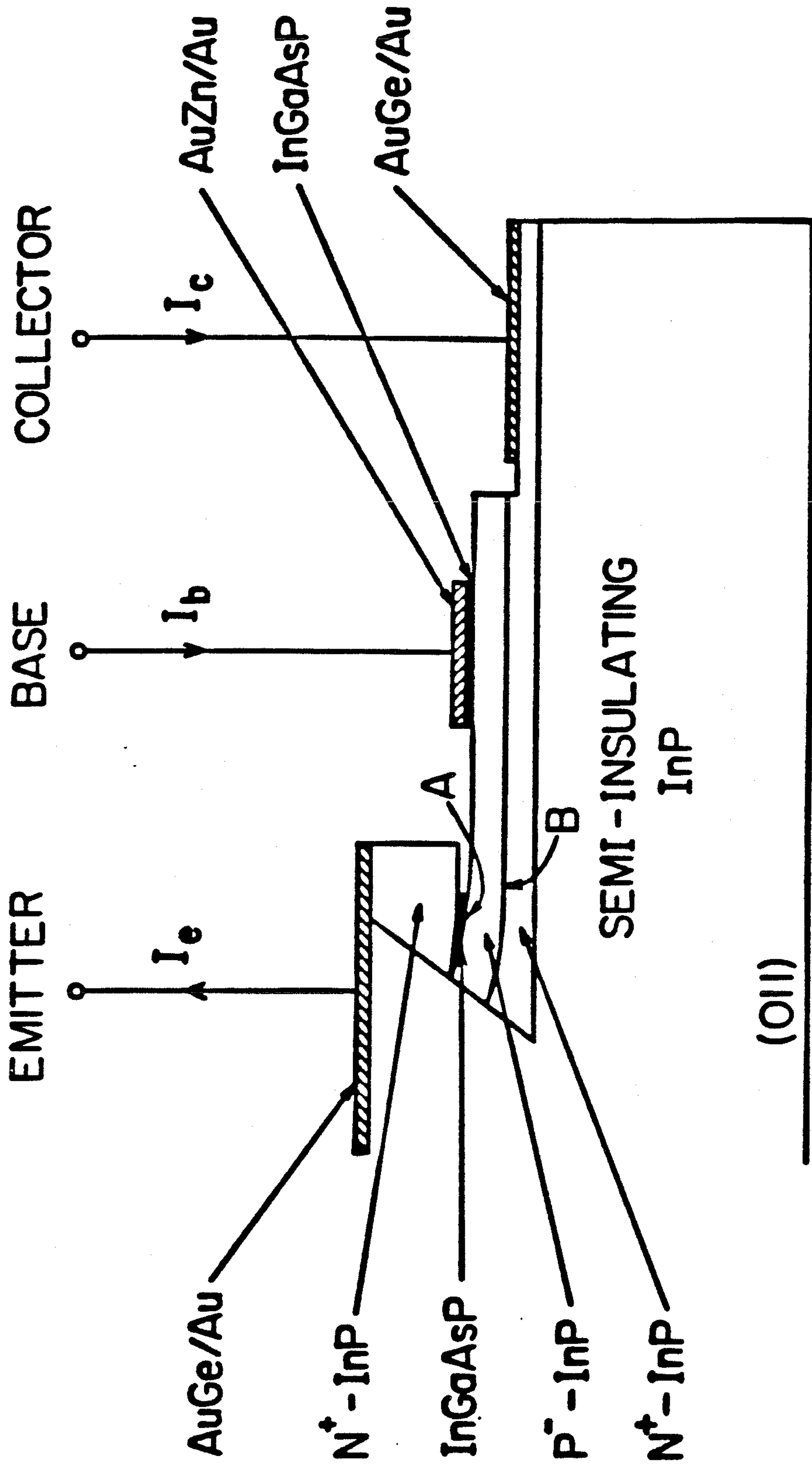

Figure 3.10 Schematic representation of the laser-bipolar-transistor structure.

mesa InGaAsP/InP DH laser described in chapter 2. However, an extra N^+-InP layer was added in order to collect the leakage current. The composition and the thickness of the four epitaxial layers are: N^+-InP collector layer (Sn doped, $N = 2\times10^{18}cm^{-3}$, 3-4 μm thick), P^--InP confining layer (Zn doped, $P = 2\times10^{17}cm^{-3}$, 1.5 μm thick), undoped InGaAsP active layer (background electron concentration is 4-9 $\times10^{16}cm^{-3}$, 0.2 μm thick) and N^+-InP confining layer (Sn doped, $N = 2\times10^{18}cm^{-3}$, 4 μm thick). The last three layers constitute a typical DH InGaAsP/InP laser. After epitaxial growth, selective etching was performed on the top N^+-InP layer with the resulting mesa structure formed as shown in the left part of Fig. 3.10. In order to have low threshold current lasers, the quaternary layer was undercut with a selective etchant to obtain the desired width. Part of the wafer was also etched down to the bottom N^+-InP layer to facilitate the fabrication of the collector contact as shown in the right part of Fig. 3.10. Finally, three electrical contacts for the emitter, base and collector of the N-p-N bipolar transistor, were fabricated as shown.

Under forward bias condition, the emitter-base junction acts as a laser diode. The electrons are injected from the N^+-InP (emitter) into the quaternary (base) region. In this structure, those electrons which have surmounted the hetero-barrier at A and arrived at the base-collector junction (B) will be swept out by the electric field in the reverse biased junction. As the thickness of the P^--InP layer is smaller than a diffusion length of the electron ($\sim 3-4\ \mu m$ [3.9]), most of the leaking minority carriers will be collected thus giving rise to the collector current I_c. Since the electron leakage is expected to be much more significant than hole leakage in this system due to the relatively small effective mass of electrons in the active region, the structure shown in Fig. 3.10 is specially designed to measure the electron leakage.

Since the active layer of the laser is bounded on the sides by semi-insulating InP and air respectively, the current leakage due to carriers bypassing the active region through the burying layer, as is the case in some conventional heterostructure lasers, is completely eliminated. This enables us to measure directly the carrier leakage over the hetero-barrier.

The general behavior of the collector current versus the collector voltage is shown in Fig. 3.11. As the collector voltage increases, the collector current also increases and eventually saturates. This saturation occurs when the junction is reverse biased and all the electrons which have overcome the hetero-barrier are collected. Hence, this saturated collector current is just the electron leakage current (assuming negligible carrier loss in the P^--InP layer by recombination process or other processes). It has been found that under low injection condition, the electron leakage is very small. However, it increases rapidly with increasing injection. For the present structure, the leakage current is about 15-30 percent of the total injection current (with collector disconnected) when the latter is about 20 mA (corresponding to a current density of $\sim$ 4 kA/cm^2, which is near the threshold current density of the lasers). A typical leakage current versus the total injection current characteristics is shown in Fig. 3.12. It is noticed that the leakage current increases with injection current and that no saturation occurs even above threshold.

To insure that the current leakage does not flow through the possible parasitic junction near the tip of the active layer, the quaternary layer of some of the lasers was etched away completely. The resulting device was then measured as described above. The results indicate negligible current leakage through this possible parasitic junction.

By reversing the dopant types in Fig. 3.10, hole leakage current can be meas-

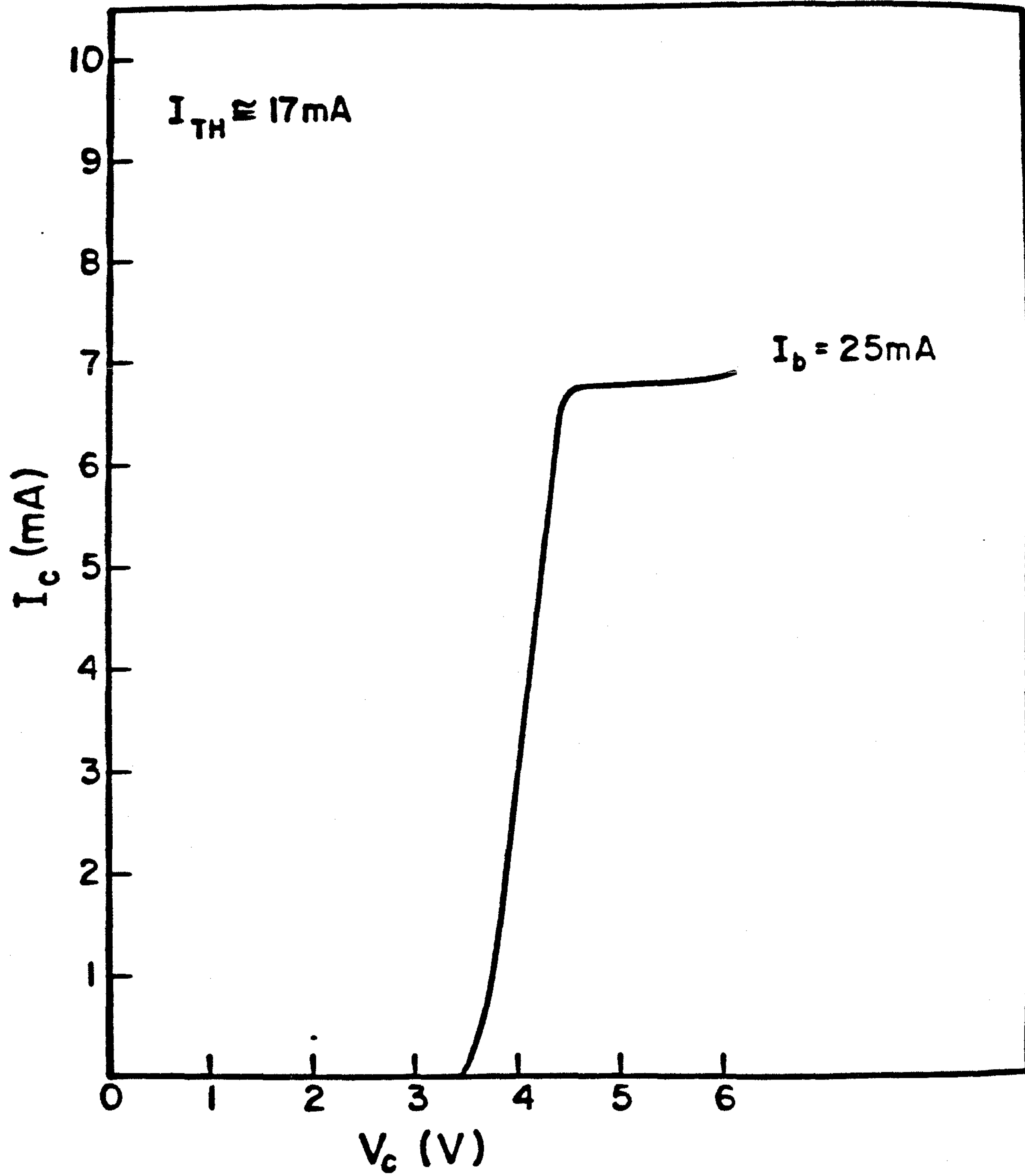

Figure 3.11 General behavior of the collector (leakage) current and collector voltage.

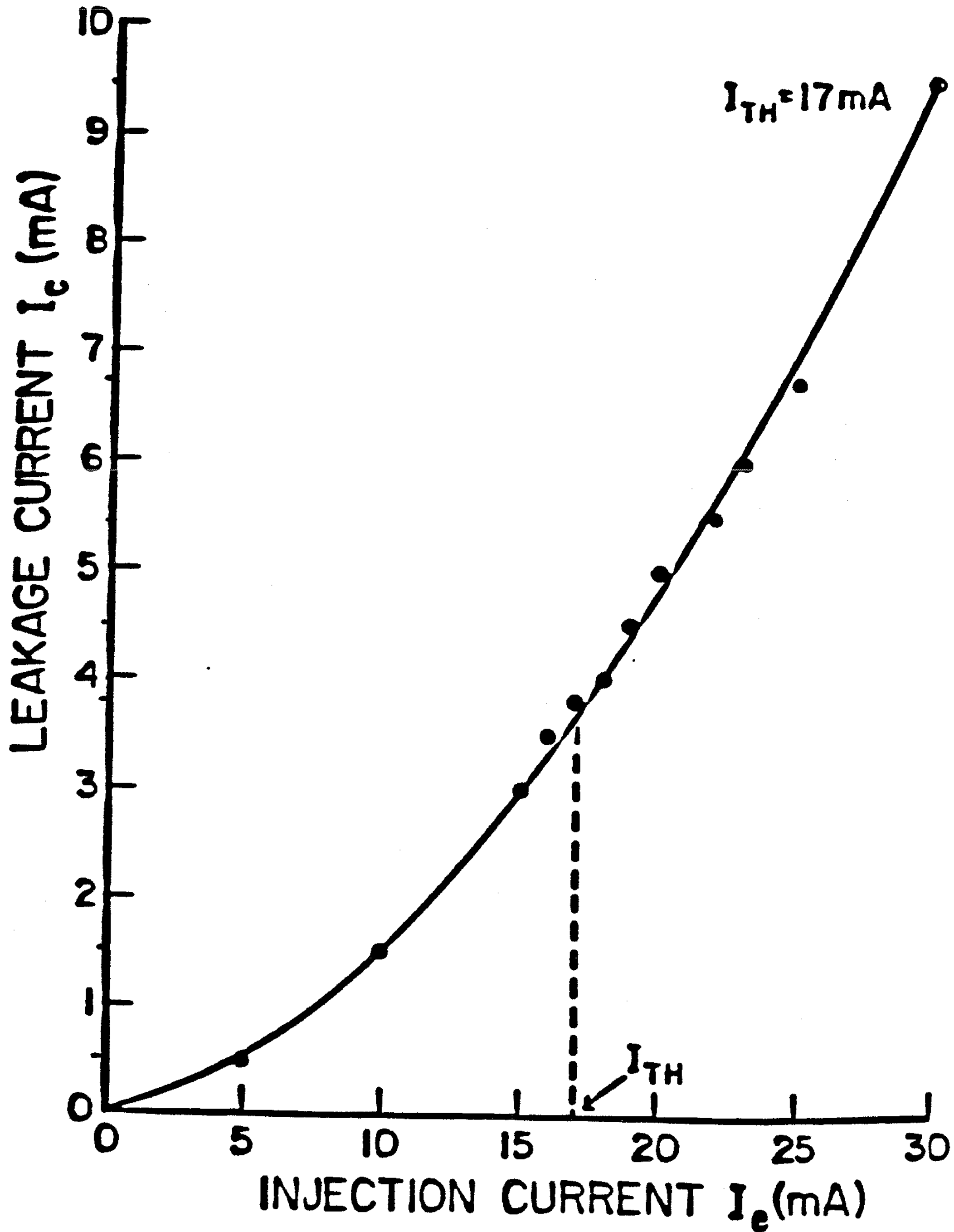

Figure 3.12 A typical leakage current vs injection current characteristics.

ured. However, no hole leakage was detected, even when the injection current was over 10 kA/cm^2. We thus conclude that hole leakage is insignificant in InGaAsP/InP heterostructures. The underlying physics will become clear in the next section.

The leakage current as a function of temperature has also been measured in the range of 10-30 °C. Results are shown in Fig. 3.13. It can be seen that the leakage current is a rather sensitive function of temperature. Since the leakage and threshold current can now be measured simultaneously, an intrinsic "leakage free" threshold can be obtained by substracting the measured leakage current from the threshold current. Thus, a "leakage free" characteristic temperature T_0 can be obtained. The result is shown in Fig. 3.14. This demonstrates directly the influence of electron leakage on the T_0 of the laser. The leakage free T_0 of 89 °K is still smaller than the corresponding figures for the GaAs lasers. This is believed to be limited by the non-radiative Auger recombination as explained in section 3.2.

3.5 Carrier Leakage in InGaAsP/InP Heterostructure—Theory

In this section, a theoretical model for the electron leakage is presented. The model takes into account the detail band structure at the InGaAsP/InP interface. Calculated results are then compared with available data for lasers and LEDs. The results indicate the important role played by hot carriers (section 3.3).

A most interesting and at first surprising experimental observation of the last section is the continued increase of leakage current with total current above lasing threshold (Fig. 3.12). Leakage model based on diffusion of electrons alone [3.8,3.21] cannot explain the observed phenomenon, as the expected clamping of carrier density above threshold would lead to a constant leakage

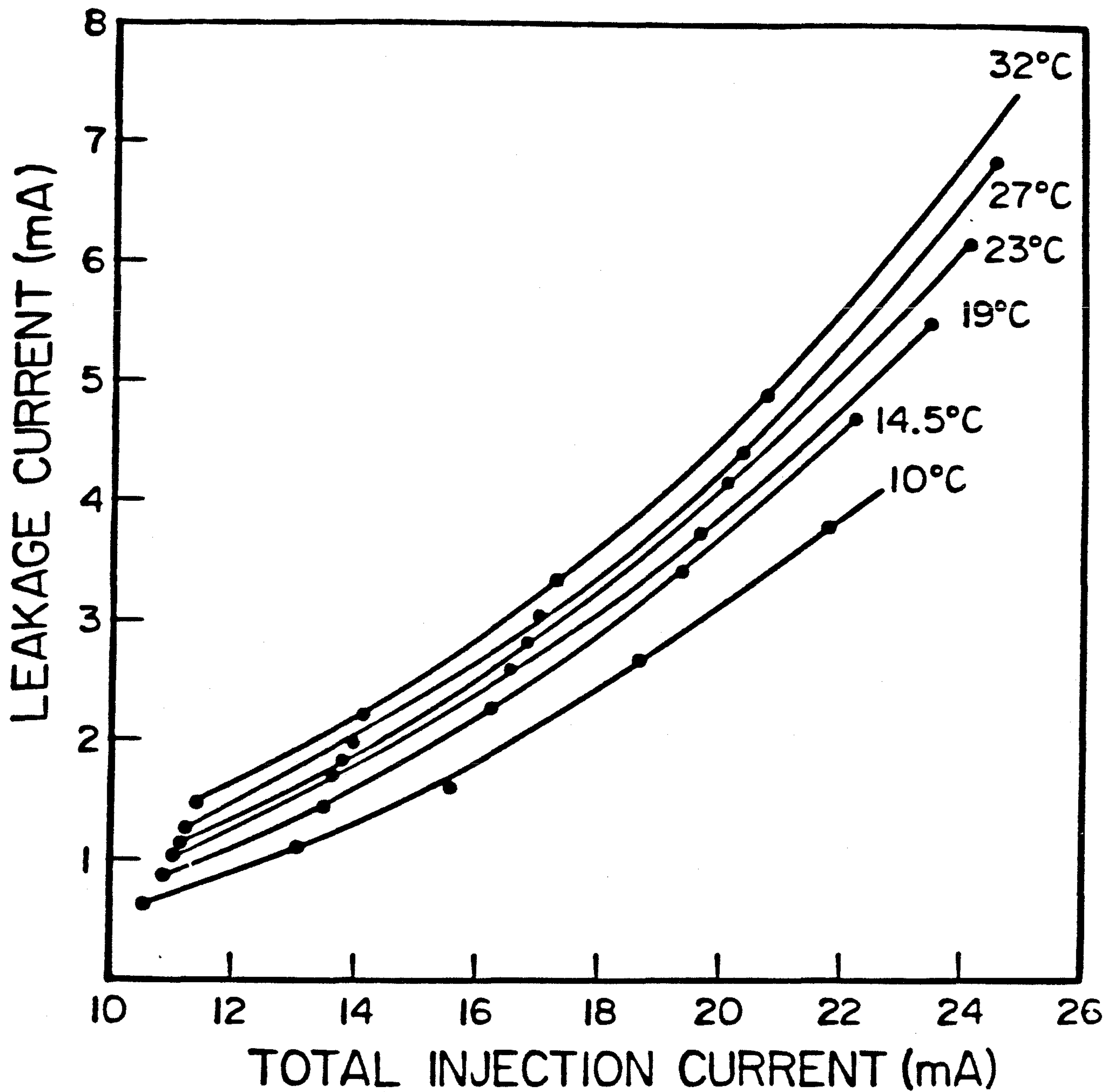

Figure 3.13 Measured leakage current in a 1.2 μ laser as a function of total injection current in the temperature range of 10 – 32 °C.

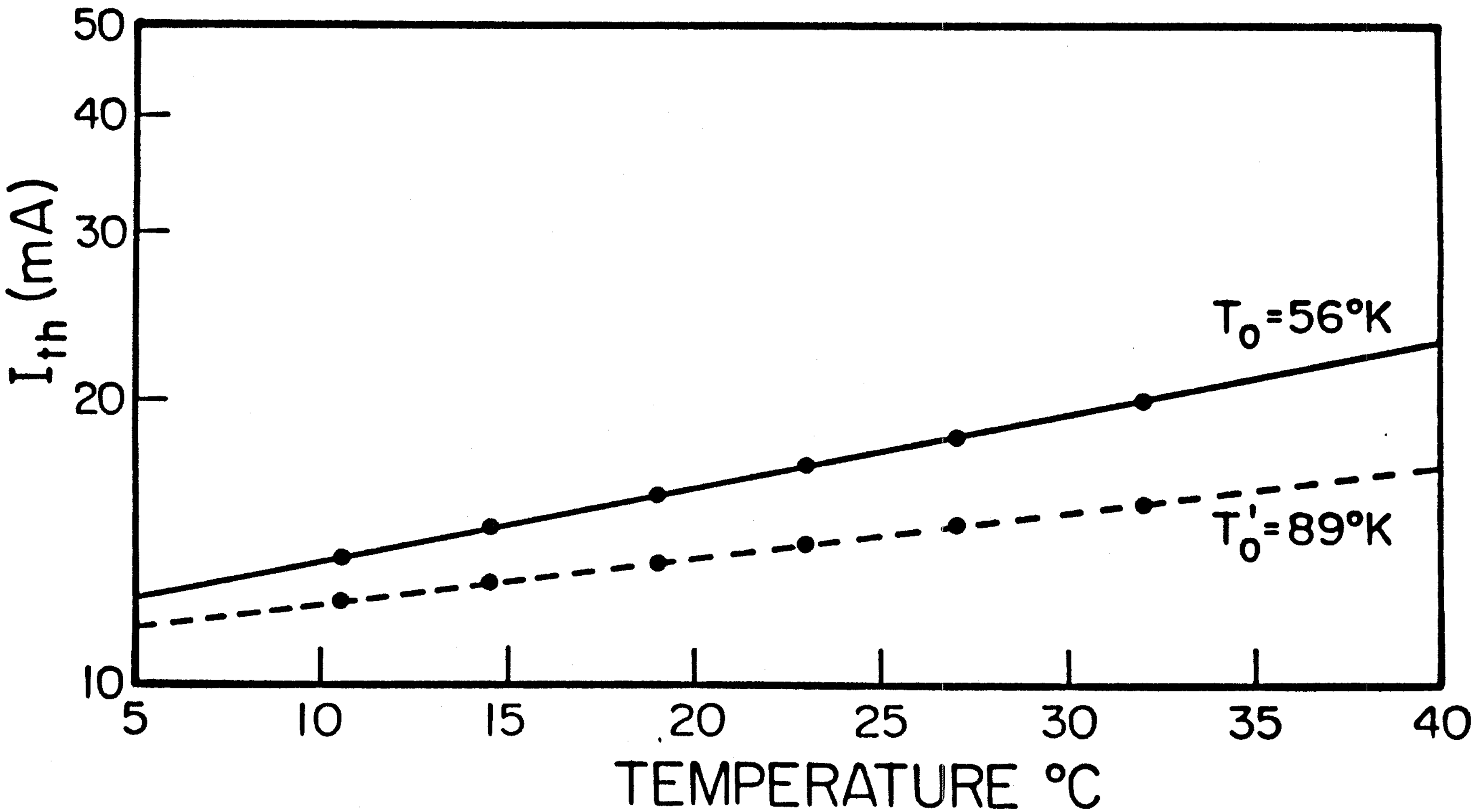

Figure 3.14 Measured T_0 and the "leakage free" intrinsic T'_0 when the leakage current is substracted.

current above lasing threshold . However, the observed behavior can be explained by invoking the electric field dominated drift component of electron current in the cladding layer. Anthony and Schumaker [3.22,3.23] were the first to recognize the significance of this field. However, their theory predicted a linear dependence of leakage current on injection current above threshold (see equation (3) of [3.23]), contrary to the experimental result (Fig. 3.12). The observed result can be explained by a theory analogous to the minority carrier injection in a Schottky diode [3.24], when the band discontinuity at the hetero-junction is taken into account.

Under high injection conditions in double heterostructure InGaAsP LEDs and lasers, if the doping level in the P-InP cladding layer is low, it can easily be shown that there exists a substantial electric field across the InP layer. In such a case, the hole current can be written as

$$\vec{J}_p = e\mu_P N_A \vec{E} \tag{3.5.1}$$

where e is the electric charge, μ_P the hole mobility, N_A the doping level in the P-InP layer, and $\vec{E}$ the electric field strength. For simplicity, only the component transverse to the junction plane will be considered. Under conditions where the majority of the current across the p-InGaAsP-P-InP interface is due to holes, the ratio of the drift and diffusion components of the electron leakage current at the junction is then given approximately by

$$\frac{J_{drift}}{J_{diff}} \approx \left(\frac{\mu_N}{\mu_P}\right)\frac{L}{eD_N N_A} J_p \tag{3.5.2}$$

where L is the thickness of the cladding layer, and is assumed to be small compared to the diffusion length of electrons in the P cladding layer, μ_N the electron mobility, and D_N the electron diffusion constant. Taking μ_N=3000 cm^2/V–sec, μ_P=150 cm^2/V–sec, L=1.5 μm, D_N=77 cm^2/sec (at 300 °K), and $N_A=10^{17} cm^{-3}$, it is

easily verified that the drift current is larger than the diffusion current when J_p exceeds ~ 420 A/cm^2. Since normal lasers operate at much higher current densities, it is expected that the drift rather than diffusion current will dominate. Since the drift (leakage) current increases with the field $\vec{E}$, and $\vec{E}$ increases with J_p (see (3.5.1)), it follows that the leakage current continues to grow with injection current past threshold.

Fig. 3.15 shows the band structure (not to scale) at the p-InGaAsP--P-InP hetero-interface at thermal equilibrium. κ, the fraction of the diffusion potential (V_D) on the wide-gap side, is given by [3.25]

$$\kappa = \frac{1}{1 + \frac{\varepsilon_2 N_{A2}}{\varepsilon_1 N_{A1}}} \tag{3.5.3}$$

where ε is the dielectric constant and the subscripts 1 and 2 denote the low and high gap materials respectively. The hole current under a forward bias V ($=V_1+V_2$; $V_2=\kappa V$, $V_1=(1-\kappa)V$) is then given by (Appendix A)

$$\begin{aligned} J_P &= \tilde{J}_{ps}\,(e^{\frac{eV_2}{kT}} - e^{-\frac{eV_1}{kT}}) \\ &= \tilde{J}_{ps}\, e^{-\frac{eV_1}{kT}}(e^{\frac{eV}{kT}} - 1) \\ &= J_{ps}\,(e^{\frac{eV}{kT}} - 1) \end{aligned} \tag{3.5.4}$$

with

$$J_{ps} = eN_{A2}\left(\frac{kT}{2m_{2h}\pi}\right)^{\frac{1}{2}} \frac{1}{\left(1 + \frac{\left(\frac{kT}{2m_{2h}\pi}\right)^{\frac{1}{2}}}{v_{d2}}\right)} e^{-\frac{eV_1}{kT}} e^{-\frac{\kappa e V_D}{kT}} \tag{3.5.5}$$

where

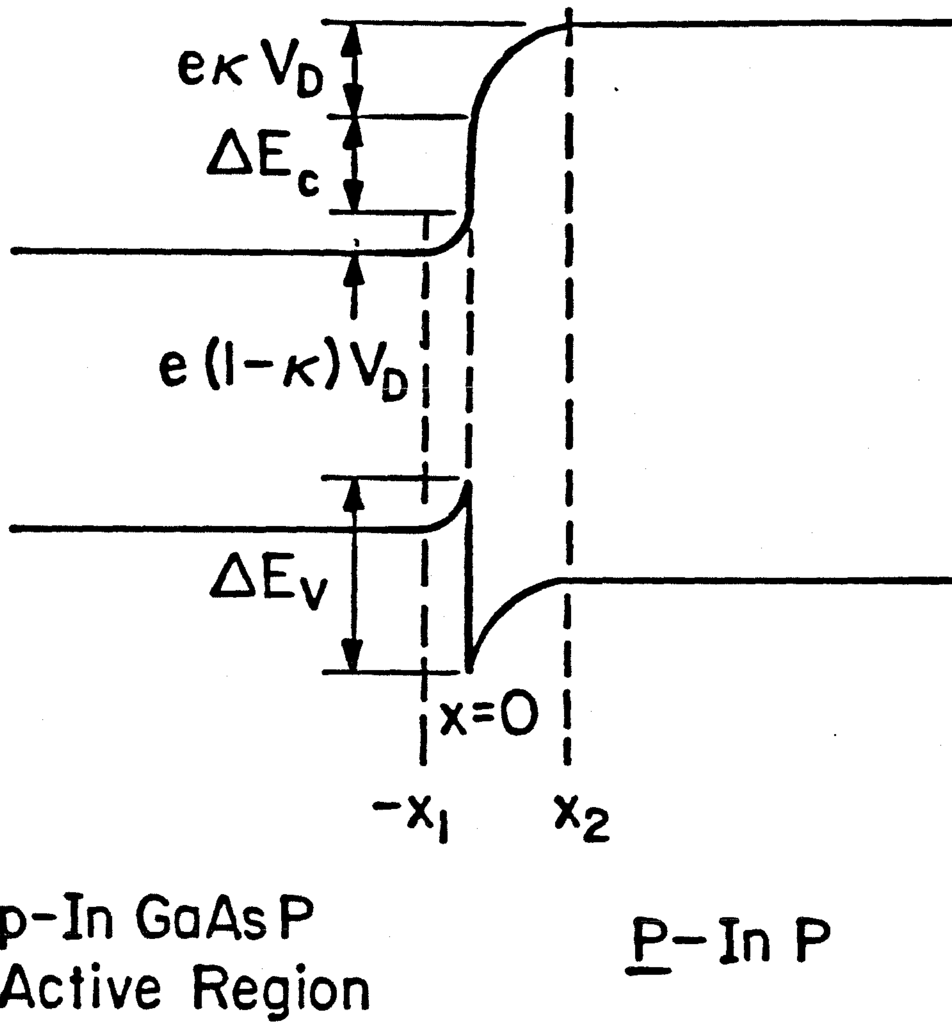

Figure 3.15 **Band structure at the p-InGaAsP–P-InP hetero-interface at thermal equilibrium.**

$$v_{d2}^{-1} = \frac{1}{\mu_{P2}kT}e^{\frac{(1-\kappa)eV_D}{kT}}e^{-\frac{\Delta E_v}{kT}}\mathrm{erf}[(\frac{\kappa eV_D}{kT})^{\frac{1}{2}}]\sqrt{\frac{\pi\varepsilon_2 kT}{2N_{A2}}} \qquad (3.5.6)$$

which are analogous to the thermionic-diffusion model of a Schottky barrier [3.26]. In the above, m_{2h} is the hole effective mass and ΔE_v is the discontinuity in the valence band. The electron concentration at x_2 (see Fig. 3.15) is given approximately by

$$N_2(x_2) = (\frac{m_{2e}}{m_{1e}})^{\frac{3}{2}} n_1 e^{\sum_{i=1}^{4} A_i (\frac{n_1}{N_{C1}})^i} e^{-\frac{\Delta E_c}{kT}} e^{-\frac{eV_D}{kT}}(e^{\frac{eV}{kT}} - 1) \qquad (3.5.7)$$

where n_1 is the electron density in material 1 (InGaAsP), A_i's are constants which account for the degeneracy [3.25], and N_{C1} and N_{C2} are the conduction band effective density of states.

In most cases, it can be verified that $v_d >> (\frac{kT}{2m_{2h}\pi})^{\frac{1}{2}}$, and the conduction mechanism is dominated by thermionic emission [3.27]. Also, though (3.5.4) indicates a rectifying characteristic, the large J_{ps} value (exceeds 1000 A/cm^2 in most cases) renders the junction more "ohmic" than rectifying in nature.

Solving the carrier transport and continuity equations for electrons, the electron leakage current is given by [3.24]

$$J_e(x) = (\frac{\mu_N}{\mu_P})\frac{J_P}{N_{A2}}N_2(x_2) - \frac{eD_N}{A}N_2(x_2)\left[\frac{1}{y_1}e^{\frac{L}{y_2}-\frac{x}{y_1}} + \frac{1}{y_2}e^{-\frac{L}{y_1}+\frac{x}{y_2}}\right] \qquad (3.5.8)$$

where

$$A = e^{\frac{x_2}{y_2}-\frac{L}{y_1}} - e^{-\frac{x_2}{y_1}+\frac{L}{y_2}}$$

$$y_{\frac{1}{2}} = \frac{\pm L_{ed}^2 + \sqrt{L_{ed}^4 + 4L_e^2}}{2} \qquad (3.5.9)$$

$$L_{ed}^2 = \left(\frac{\mu_N}{\mu_P}\right)\frac{J_p \tau_{N2}}{eN_{A2}} , \quad \text{and} \quad L_e^2 = D_N \tau_{N2}$$

with τ_{N2} the electron lifetime in the InP cladding layer and L the thickness of the cladding layer. In arriving at the above solution, we have assumed the boundary condition of $N_2(L) = 0$. However, when the leakage is drift dominated, the boundary condition $N_2(L)$ is not important as is apparent from (3.5.8).

The total injected current density J_{tot} is simply

$$J_{tot} = J_p + J_e = J_{rec} + J_{leak} \tag{3.5.10}$$

Since J_e is just the leakage current J_{leak}, it follows that the recombination current $J_{rec} = J_p$. Up to lasing threshold, J_p can be expressed as

$$\frac{J_{rec}}{ed} = Bn_1(n_1+N_{A1}) + C_{chcc}n_1^{2.09}(n_1 + N_{A1}) + C_{chsh}n_1(n_1 + N_{A1})^{2.14} \tag{3.5.11}$$

where d is the active layer thickness, B the radiative recombination constant, C_{chcc} and C_{chsh} are the Auger coefficients for the CHCC and CHSH processes (3.2.15). B is estimated from spontaneous lifetime data and C_{chcc} and C_{chsh} are calculated as described in section 3.2.

As can be seen from (3.5.4), (3.5.5), (3.5.6) and (3.5.7), the discontinuities in the conduction (ΔE_c) and valence band (ΔE_v) play an important role in determining the magnitude of the leakage current. Unfortunately, the discontinuity in the quaternary system is not known accurately. However, there are experimental [3.28,3.29] and theoretical [3.30] indications that a substantial fraction of the discontinuity lies in the valence band. We have used $\Delta E_c = \frac{1}{3}E_g$ as measured in Refs. [3.28] and [3.29]. If the interface is graded, then the potential "spike" which is resistive to hole injection would decrease, resulting in less leakage. Here, an abrupt interface is assumed. However, the ratio $\frac{\Delta E_c}{\Delta E_v}$ as well as the

doping level N_{A2} are varied to provide a quantitative trend and estimate of the leakage current and its effects.

It was found that for 1.3 μm LEDs, if effects of carrier heating and/or Auger enhanced leakage [3.31] were excluded, the predicted leakage using reasonable parameters would be much smaller than the observed values. Much better agreement could be obtained by incorporating carrier heating effect or employing a boundary condition $n_2(x_2) \sim e^{-\frac{3}{4}\frac{\hbar\omega_o}{E}\frac{d^2}{L_p^2}}$ (where $\hbar\omega_o$ is the optical phonon energy, E is the maximum energy an Auger electron can lose and still be able to surmount the heterobarrier, and L_p is the electron mean free path) and use the approach in section 3.3. Due to the uncertainty in L_p and the availability of experimental data on carrier heating effect, the former is chosen. The results of T_e at 300 °K from Ref. [3.32] have been used and the electron temperatures at various lattice temperatures (T_L) are estimated from the expression

$$T_e(T_L) = T_e(300)\ \frac{C_{chcc}(T_L)}{C_{chcc}(300)} \tag{3.5.12}$$

Thus, it is implicitly assumed that the hot carriers are generated by the Auger process.

Results of the calculation are presented in Figs. 3.16-3.19. Fig. 3.16 shows the calculated ratio of $\frac{J_e}{J_p}$ in an LED with d=.15 μm, L=.3 μm at various temperatures under three different injection conditions. The triangles are experimental data from Ref. [3.20]. For $\Delta E_c = \frac{1}{3}E_g$, reasonable agreement can be obtained by taking $N_{A1} = 4.6\times10^{17}\text{cm}^{-3}$ and $N_{A2} = 1.4\times10^{17}\text{cm}^{-3}$. The dashed line denotes ratio of $\frac{J_e}{J_p}$ when the carrier heating effect has been neglected. Fig. 3.17 shows the calculated effect of doping and discontinuity on the magnitude of leakage

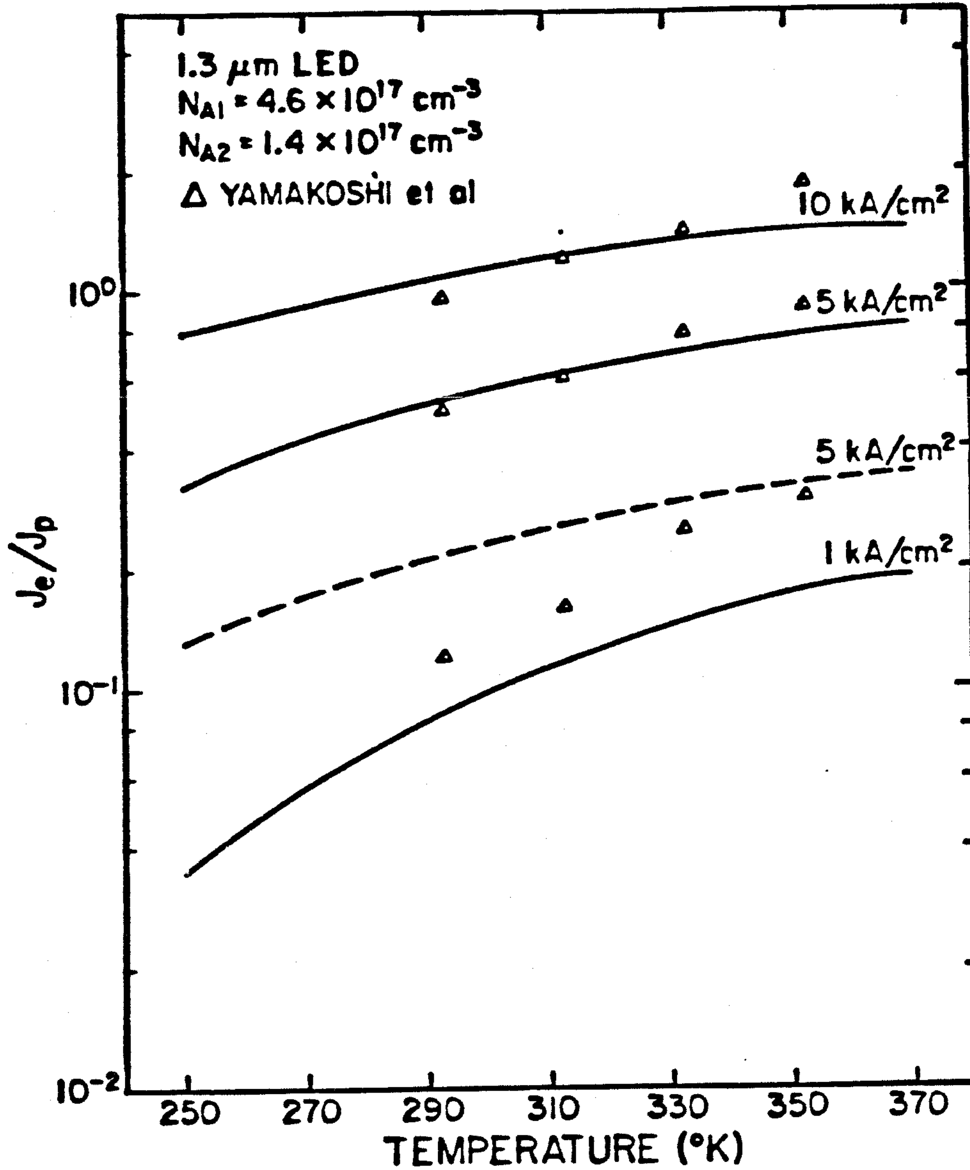

Figure 3.16 Calculated $\frac{J_e}{J_p}$ under different injection conditions. Experimental data are from Ref. [2]. The dashed line denotes the result when hot carrier effect is neglected.

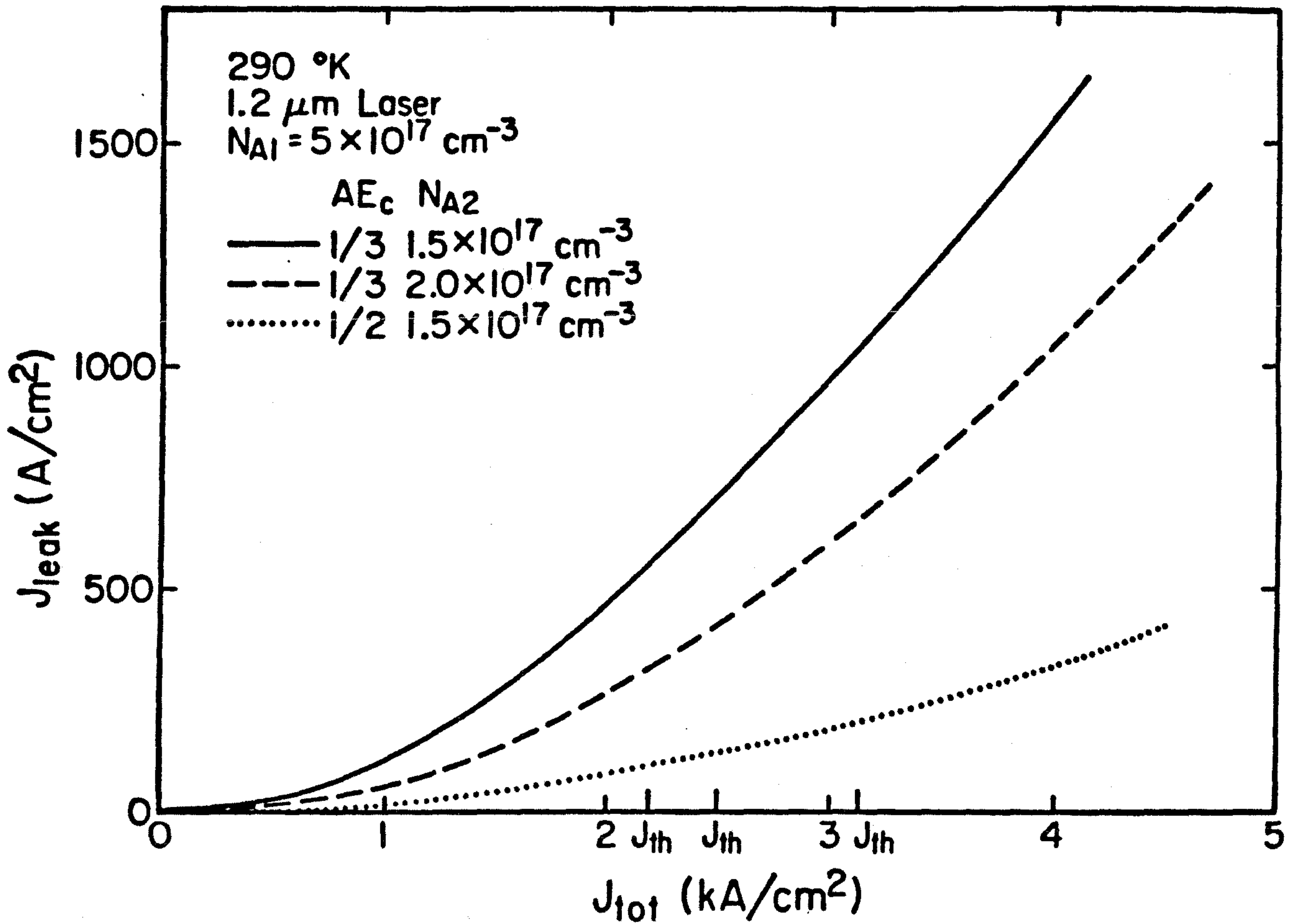

Figure 3.17 **Calculated electron leakage current versus total injected current for different P-InP doping levels and different discontinuities (ΔE_c) in the conduction band.**

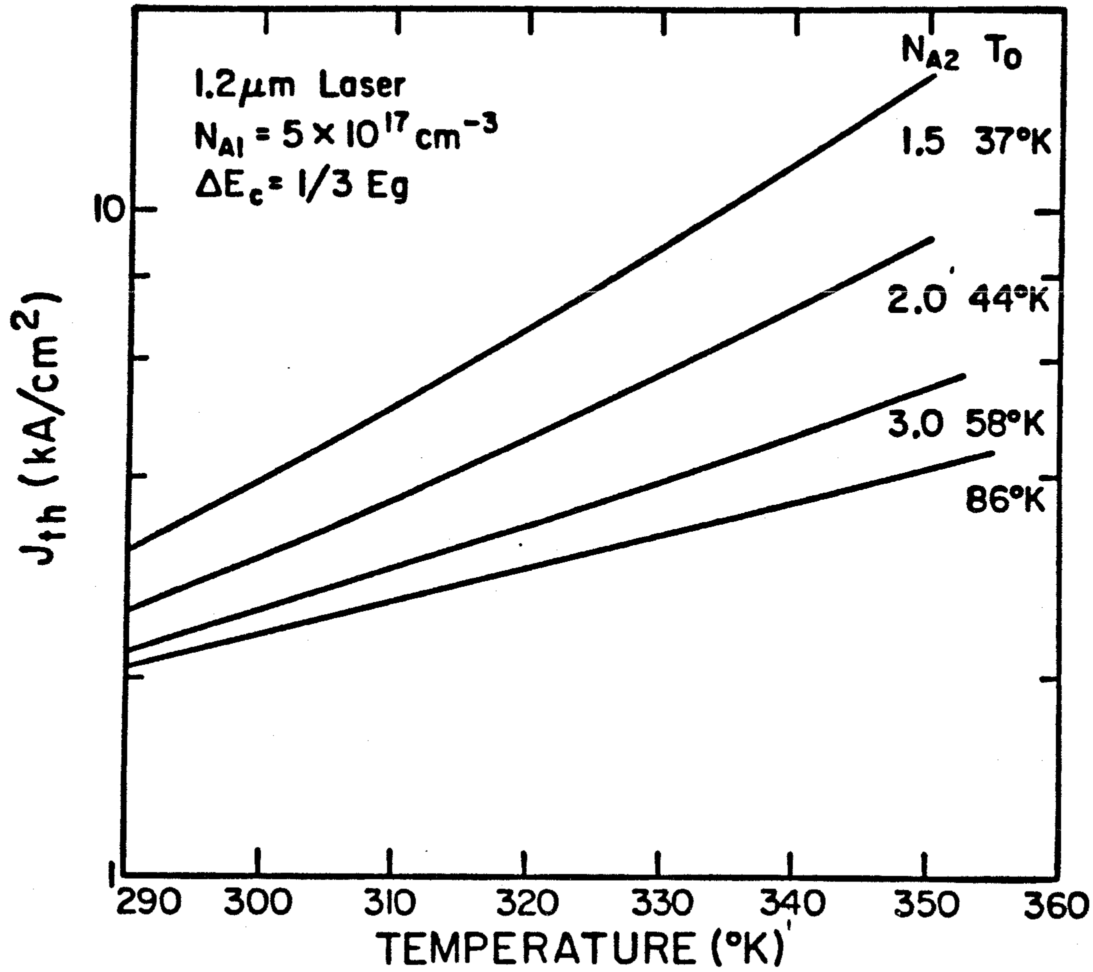

Figure 3.18 **Calculated T_o for different P-InP doping levels. The T_o = 86 °K is calculated without electron leakage.**

current in a 1.2 μm laser with d=.2 μm and L=1.5 μm. It is apparent that in order to minimize leakage, the cladding layer could be doped heavily or a graded junction be grown to smear the "spike" at the interface. There is a slight discontinuity in slope at J_{th}. However, for larger leakage currents, the change in slope is very small and insignificant. Fig. 3.18. depicts the effect of leakage current on the T_o of the laser. The influence of the P-doping is again conspicuous. Note that the curve for T_o = 58 and 86 °K agrees with the measured one of Fig. 3.14. Fig. 3.19 shows the measured leakage and the predicted leakage using the present model and that of [3.23] at a temperature of 295 °K. It should be stressed that when the doping level in the cladding layer is high, the "spike and notch" at the hetero-interface can be "washed out," resulting in reduced leakage current and also different dependence of the leakage current on the total injection current beyond threshold.

It is also clear from (3.5.8) that the ratio of the hole leakage current to electron leakage current will be on the order of $\left(\frac{\mu_P}{\mu_N}\right)^2$. Thus, the hole leakage current will be insignificant, and is consistent with the experimental result of section 3.4. To compare the influence of leakage current in lasers of different emission wavelengths, ratios of J_e/J_{tot} have been calculated for $N_{A1} = 5\times10^{17}$ cm^{-3}, $N_{A2} = 2\times10^{17}$ cm^{-3}, and $\Delta E_v = \frac{1}{3}E_g$ at an ambient temperature of 290 °K. The results are summarized in Table 3.3. From the table, we see that leakage current decreases as wavelength increases. This is expected since ΔE_c increases with the wavelength, giving rise to better carrier confinement. Also, the importance of carrier heating effect is apparent, especially for devices with emission wavelengths beyond 1.3 μm.

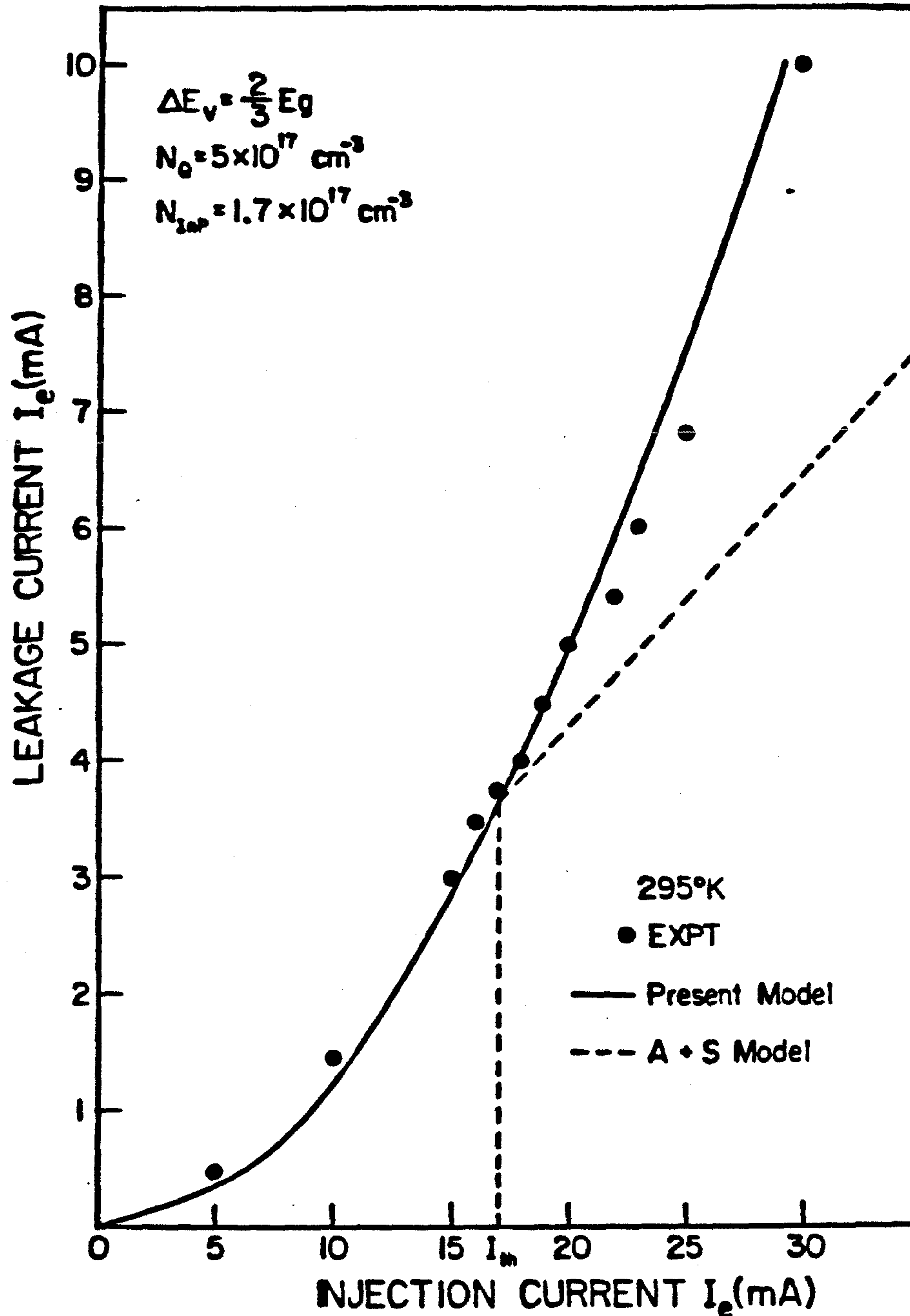

Figure 3.19 Measured electron leakage current vs injection current characteristics. The dashed line is the predicted leakage current from Ref. [8], the solid line is that predicted by the present model (the discontinuity in slope at threshold is almost imperceptible).

-	With Hot Carriers			Without Hot Carriers		
λ	1.2	1.3	1.5	1.2	1.3	1.5
J_e/J_{tot}	22%	11%	4%	11%	3%	0.4%

Table 3.3 Comparison of J_e/J_{tot} for lasers at 1.2, 1.3, and 1.5 μm with and without carrier heating effect.

3.6 Dependence of T_0 on P-Cladding Layer Doping Level

From the previous section (equation (3.5.8) and Fig. 3.18), we see that the leakage current decreases at least quadratically as the inverse of the doping level in the cladding layer. Therefore, when the doping level in the cladding layer is high, the leakage current is reduced, leading to higher T_o (Fig. 3.18).

To substantiate the above, experimental investigations of the effects of P-layer doping level on the inherent T_o of InGaAsP lasers emitting at 1.2 and 1.3 μm were performed under various conditions. The lasers used in the study are the Terrace Mesa Lasers (T-ME) described in chapter 2. This particular structure was chosen because it was essentially the same structure as that used in the measurement of electron leakage. In the first experiment, the atomic fractions of zinc in the growth melt were $\sim 10^{-5}$ and $\sim 10^{-4}$ respectively. The T_o for the low doping level lasers was found to be 43 ± 5 °K [3.33], with average threshold current density around 5.2 kA/cm^2. The external quantum efficiency was found to be 50-60 % for both facets. For the lasers grown with higher zinc concentration, the T_o was 85 ± 5 °K (highest obtained was 90 °K) with threshold current densities averaging around 8.4 kA/cm^2. Thus, by increasing the doping level in the growth melt, the T_o was increased significantly. In doing so, however, we paid the penalty in higher threshold current density and lower quantum efficiency (~ 30 % for both facets). This increase in the threshold current density is attributed to the out-diffusion of Zn from the cladding into the active layer during crystal growth [3.9,3.34].

In the second experiment, a grown wafer with moderate P-doping in the cladding layer was cleaved into two structurally identical pieces, one of which was re-introduced into the liquid phase epitaxy (LPE) system and heated to 675 °C in an atmosphere of H_2 for about an hour. The two wafers were then processed into

the T-ME lasers. The T_o of the lasers from the unheated wafer was found to be 60 ± 7 °K, whereas T_o was 41 ± 7 °K for the lasers fabricated from the heat treated wafer. No significant difference in threshold current was observed in this case. The phenomenon agrees with the previously observed T_o of the mass transport lasers (T_o = 40 - 50 °K) and that of the T-ME's (T_o = 60 - 70 °K) (chapter 2.). The decrease in T_o is attributed to the decrease in doping concentration in the cladding layer as a result of Zn out-diffusion during heating.

Having identified the cause of the low T_o, we proceeded to modify the structure to impede zinc diffusion into the active region. The schematic of the new structure is shown in Fig. 3.20. A thin (0.3 - 0.5 μm) P^--InP layer was first grown adjacent to the active layer, followed by the ordinary P^+-InP high doping layer. This thin layer acts as a buffer to absorb the Zn diffused from the P^+ layer to provide the desirable highly doped cladding layer, and at the same time acts as a "diffusion stop" layer to reduce the Zn diffusion into the active layer.

The resulting lasers were found to have T_o of 83 ± 4 °K with threshold current densities around 4.0 kA/cm^2 (lowest I_{th} was 11 mA for a cavity volume of $250 \times 0.2 \times 1.5\ \mu m^3$). The light versus current characteristics of a typical laser with threshold current around 20 mA are shown in Fig. 3.21. The external quantum efficiency is around 70 % for both facets (at $I = 3I_{th}$) and the laser is capable of operating in the fundamental transverse mode and of delivering 200 mW per facet (pulsed operation) at an injection current of 1.8 A. Results of our experimental investigations are summarized in Table 3.4. It should be stressed that this simple modification scheme can be applied to most laser structures, resulting in improved laser performance. The T_o's measured in the T-ME's are "inherent" values, and the modification scheme demonstrated here provides a simple way to improve the temperature sensitivities without sacrificing laser threshold. We also recognize that if the cladding layer is doped with elements

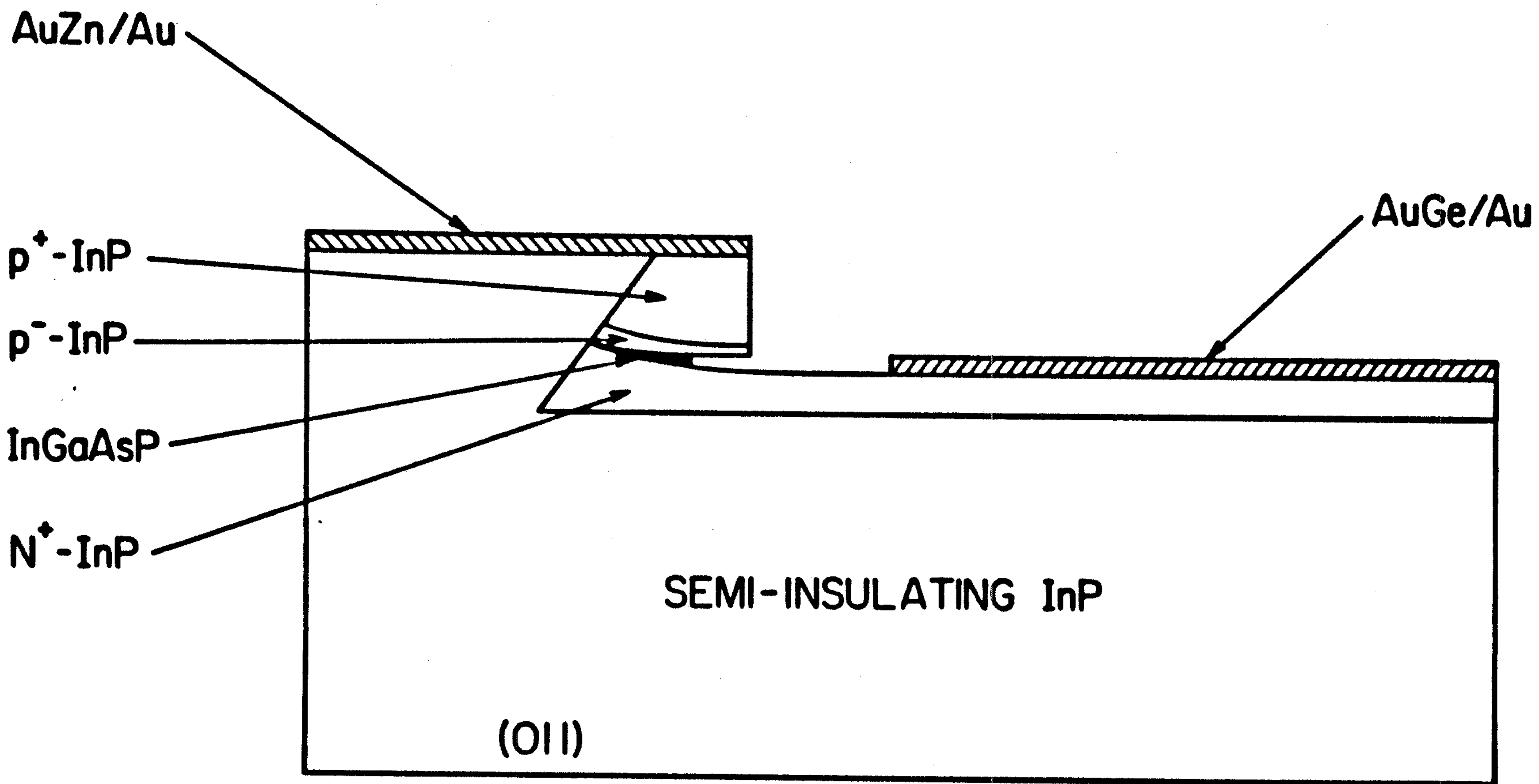

Figure 3.20 Schematic drawing of the modified T-ME laser structure.

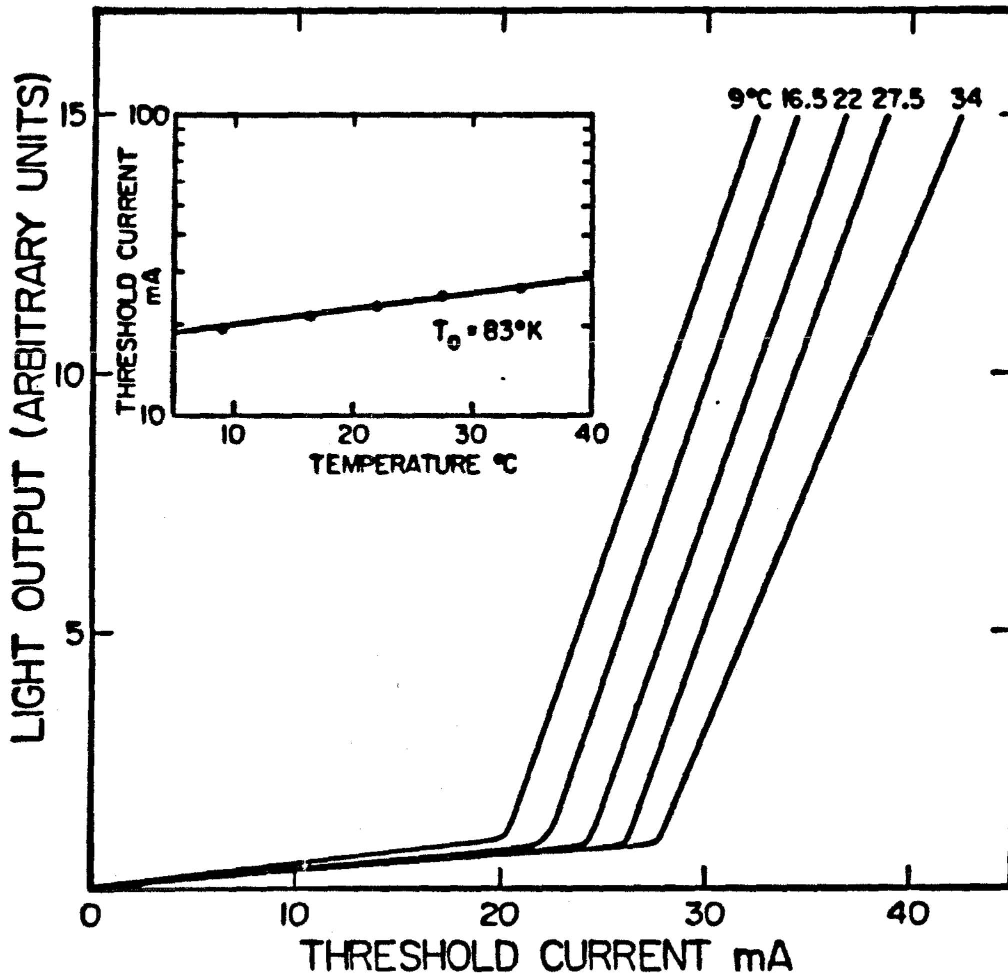

Figure 3.21 **Typical light versus current characteristics of the modified T-ME lasers.**

Wavelength (μm)	Condition	T_o (°K)	J_{th} (kA/cm²)
1.2	Wafer heated at 675 °C	41 ± 7	~ 5
1.2	Wafer not heated	60 ± 7	~ 5
1.3	Low doping level	43 ± 5	5.2
1.3	High doping level	65 ± 5	6.4
1.3	Modified structure	63 ± 4	4.0

Table 3.4 Summary of the experimental observations of T_o and threshold current density under the various conditions.

(e.g. Cd and Mg) which do not diffuse into the active layer, low threshold and high T_0 lasers may be obtained without the present blocking layer.

As a short summary, we have learned that non-radiative Auger recombination and carrier leakage are important factors determining the temperature sensitivity of InGaAsP lasers and LEDs. However, there is an important difference between the two effects. The interband Auger recombination is material dependent and intrinsic, and thus unavoidable. However, the carrier leakage is extrinsic and can be reduced by increasing the doping level in the cladding layer, as demonstrated in the modified structure.

3.7 Auger Recombination in Quantum Well InGaAsP Lasers

Although it has been demonstrated that GaAlAs/GaAs quantum-well lasers exhibit higher T_0's than normal DH lasers [3.35], it is unclear whether InGaAsP quantum-well lasers would be free from a break-point in the threshold current vs temperature characteristics. In this section, the non-radiative CHCC Auger process in the quantum-well lasers is investigated. It is found that the rate of the CHCC process is greatly reduced in such quasi two dimensional structures.

Equation (3.2.7) has been modified (see (3.7.2)) to calculate the rate of Auger recombination in a quantum-well structure. It is well-known that when the active layer thickness L_z of a semiconductor laser is of the order of the carrier de Broglie wavelength, quantum size effects arise [3.36]. The non-radiative band-to-band Auger process then changes in a fundamental way. For a quasi two dimensional layer, it is usually assumed that the single-particle Hamiltonian can be separated into a quantized component normal to the layer and continuous components in the plane of the layer [3.37]. In such case, the energy spectrum is given by [3.38]

$$E(k_{zn},k_x,k_y) = \frac{\hbar^2 k_{zn}^2}{2m^*} + \frac{\hbar^2}{2m^*}(k_x^2 + k_y^2) \tag{3.7.1}$$

where n denotes the nth quantized state of k_z, m^* is the effective mass of electrons or holes, and k_x, k_y are the continuous components of the crystal momentum. The effective masses of the electrons and holes in the direction perpendicular and parallel to the plane of the layer have been taken to be the same. The Auger rate for such quasi two dimensional systems becomes

$$P=\frac{2\pi}{\hbar}(2\beta)2\left(\frac{V}{(2\pi)^3}\right)^3\left(\frac{e^2}{\varepsilon V}\right)^2 \, \mathrm{S} \, \frac{|F_1F_2|^2}{(\,|\vec{k}_1-\vec{k}_{1'}|^2 + L_D^{-2}\,)^2} \tag{3.7.2}$$

$$\times \; [f_1f_2(1-f_{1'})(1-f_{2'})-(1-f_1)(1-f_2)f_{1'}f_{2'}]\delta(E_f-E_i)d\vec{k}_1 d\vec{k}_{1'} d\vec{k}_{2'}$$

where S denotes summing over discrete states and integrating over continuous states.

In this section, all the calculations have been performed for $In_{.72}Ga_{.28}As_{.60}P_{.40}$ for which the emission wavelength is about 1.3μm. The quantum-well is assumed to be a finite square well and the summation is extended only over the confined states in equation (3.7.2). The small Fermi factors at the top of well ($\sim 10^{-5}$–10^{-6}) justify this approximation. The rate is then calculated numerically and the Auger lifetime is obtained from (3.2.12).

The results of the calculation are presented in Figs. 3.22-3.24. In Fig. 3.22, $\frac{1}{\tau_A}$ is plotted against the electron density at a temperature of 300°K and for a quantum-well with width 100 Å. The slope of 2.45 (> 2) is typical of the non-radiative process in degenerate materials. In Fig. 3.23, the non-radiative Auger lifetimes of the quantum-well and ordinary laser structures are compared under the same injection conditions and temperatures. A well with width 100 Å has also been assumed. It shows that the Auger lifetime is about two orders of

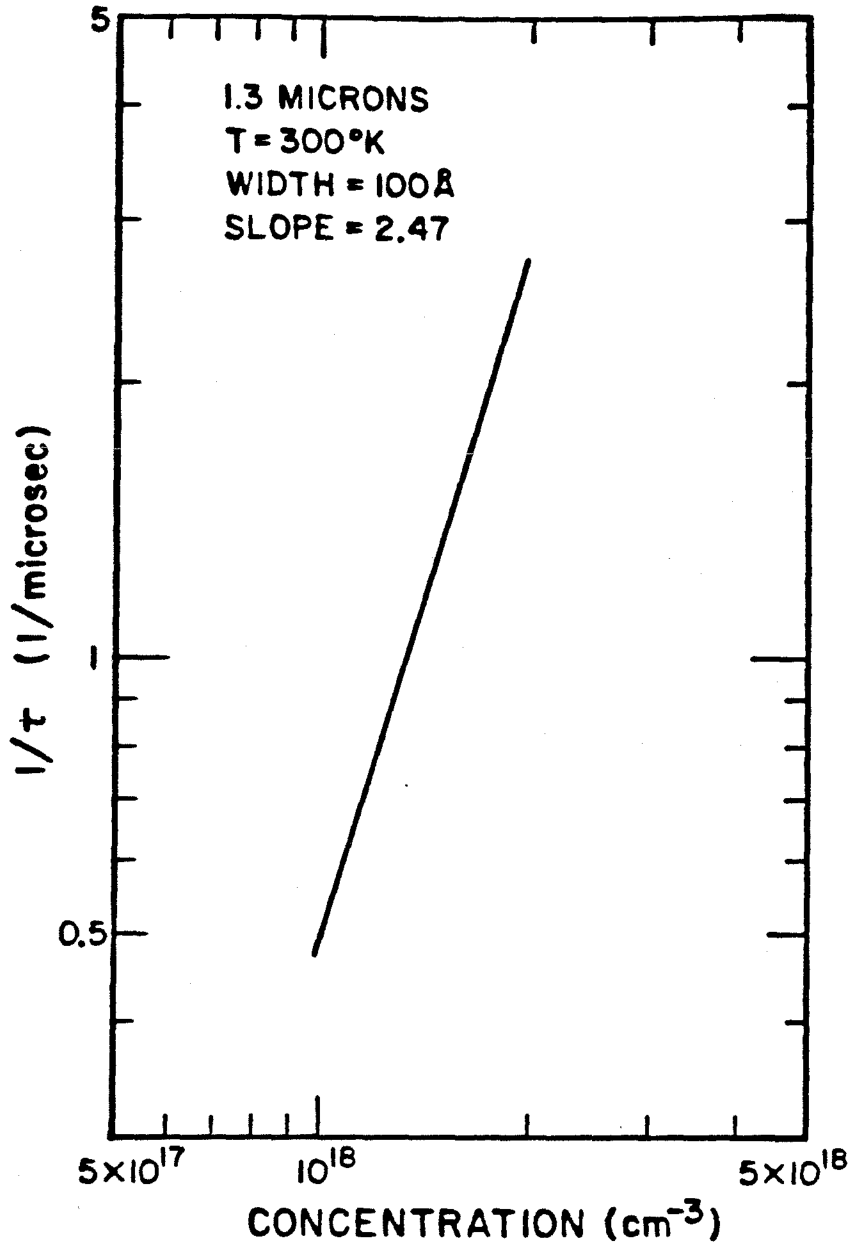

Figure 3.22 The inverse of Auger lifetime as a function of carrier concentration for a 1.3 μm quantum-well (width=100 Å) InGaAsP laser at 300°K.

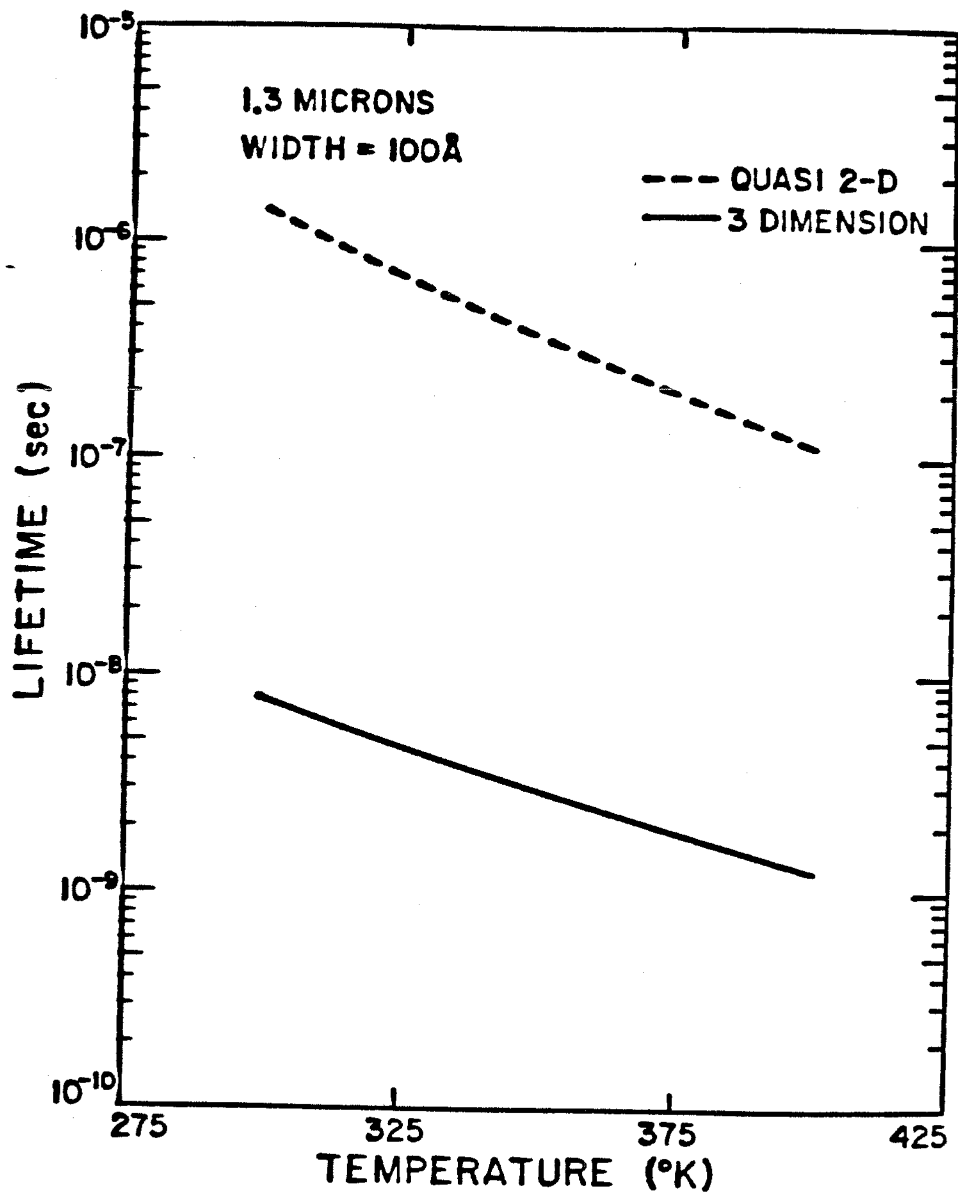

Figure 3.23 Comparison of calculated Auger lifetimes for a 1.3 μm quantum-well (width=100 Å) and ordinary InGaAsP lasers under the exact same injection conditions.

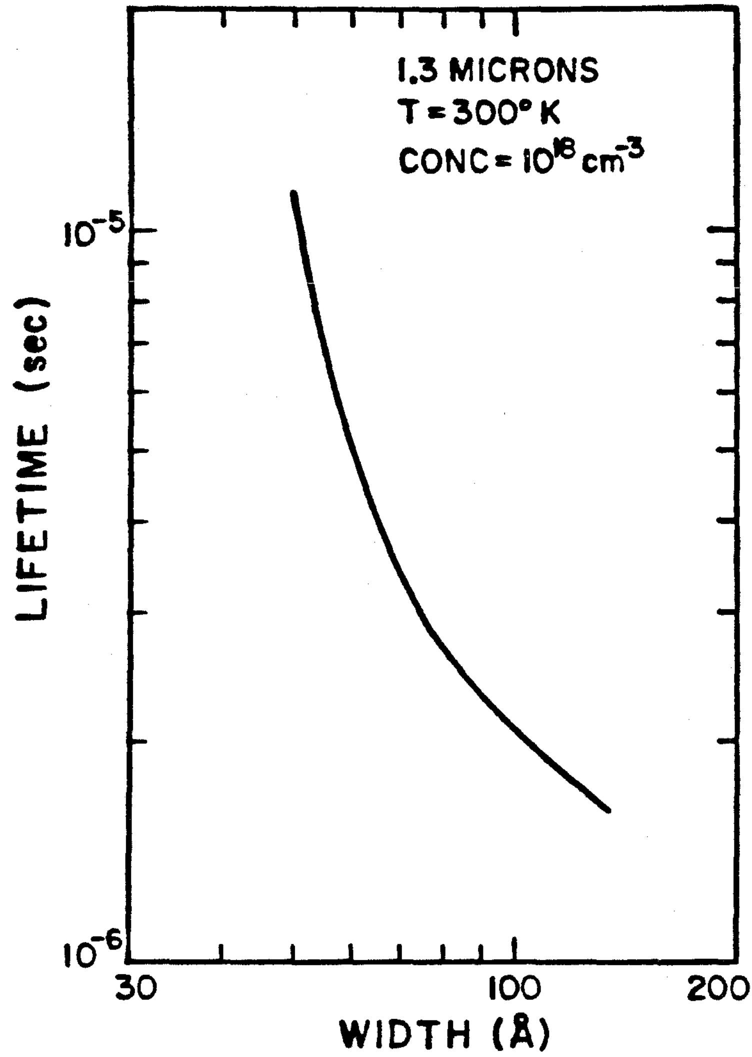

Figure 3.24. Calculated Auger lifetime for a 1.3 μm quantum-well laser as a function of well width at 300°K.

magnitude longer in the quasi two dimensional system. In Fig. 3.24 is plotted the lifetime vs width of well at a temperature of 300°K. It can be seen that the lifetime decreases rapidly with increasing well width. This is expected since the number of confined states increases and the energy separation between states decreases when the width of the well increases. Moreover, the quantum size effect would have to disappear gradually as the width increases.

The dramatic increase in lifetime in a quasi two dimensional system as compared to the three dimensional system is due to the nature of the difference in the density of states, and, more importantly, the decrease in the number of configurations that can satisfy the stringent requirement of both momentum and energy conservation simultaneously.

The threshold current density can be written as

$$J_{th} = \frac{n_{th} e d}{\tau} \tag{3.7.3}$$

for ordinary lasers and single quantum-well lasers, and

$$J_{th} = \frac{n_{th} e N d}{\tau} \tag{3.7.4}$$

for multiple quantum-well lasers [3.38]. In the above equations, e is the electronic charge, d the active layer thickness, n_{th} the injected carrier density at threshold, N the number of quantum-wells, and τ is the carrier lifetime. In ordinary lasers, it is the competition between the non-radiative processes and the radiative process which shortens the carrier lifetime (see (3.2.13)). From equations (3.7.3) and (3.7.4), it is obvious that decrease in τ causes a corresponding increase in the threshold at the same n_{th}. Although the non-radiative Auger lifetime is longer in the quantum-well lasers, it is the relative magnitude between the radiative and non-radiative lifetimes that is important.

In quantum-well lasers, it can be shown that the ratio of the radiative lifetime in three dimensional structure and quasi two dimensional system under the constant matrix element assumption can be written as

$$\frac{\tau_{q2d}}{\tau_{3d}} = \left(\frac{2m_r}{\hbar^2}\right)^{\frac{1}{2}} \frac{L_z}{\pi} (\hbar\omega - E_g)^{\frac{1}{2}} \times \frac{1}{N} \quad (3.7.5)$$

where m_r is the reduced mass of the electron and hole; L_z is the width of the well; ω is the frequency of light; E_g is the bandgap energy; and N is the number of pairs of levels where optical transition can take place. Taking N=1, it can easily be verified that the ratio is less than one for $(\hbar\omega - E_g)^{\frac{1}{2}} < .275$. Since under ordinary laser operation, $(\hbar\omega - E_g)^{\frac{1}{2}} << .275$, the radiative lifetime in a quantum-well laser is even shorter than in a conventional laser. This can be verified in the GaAs-GaAlAs system from the data in [3.35]. Thus, in the quantum-well lasers, the non-radiative CHCC Auger process is no longer competitive with the radiative process. Unfortunately, due to the uncertainty in band discontinuity of the split-off hole bands, reliable estimate of the CHSH process in a quantum well cannot be made at this time. However, since the CHCC process is now unimportant, it is likely that quantum well InGaAsP lasers will not have a low temperature break-point above which the T_0 decreases considerably. The data in [3.39] do indicate that the breakpoint is ~ 300 °K, which is considerably higher than ordinary quaternary lasers. The absence of the CHCC process may be the contributing factor to the high breakpoint.

Appendix A

Thermionic-Diffusion Model of Majority Carrier Current at a Band Discontinuity

In this appendix, the fundamental ideas of the thermionic-diffusion model used to derive (3.5.4) and (3.5.5) will be outlined for a simplified case of a one sided heterojunction. Consider the band discontinuity as shown in Fig. 3.25 (we have chosen to derive the electron current here). The majority electron current is then given by

$$J_e = e\left[-n(x)\mu_n \frac{dV(x)}{dx} + D_n \frac{dn(x)}{dx} \right] \quad \text{(A.1a)}$$

$$= e\, D_n \left[-\frac{en(x)}{kT}\frac{dV(x)}{dx} + \frac{dn(x)}{dx} \right] \quad \text{(A.1b)}$$

where the Einstein relation $\mu_n = \frac{eD_n}{kT}$ is used. Multiply (A.1b) by $\exp(-eV(x)/kT)$ and integrate by parts, we have

$$J_e \int_0^W e^{-\frac{eV(x)}{kT}}\, dx = eD_n \left[n(W)\, e^{-\frac{e(V_D - V)}{kT}} - n(0) \right] \quad \text{(A.2)}$$

where V_D is the built-in voltage and V the applied voltage (Fig. 3.25). In the case of thermionic emission, the current can be written as [3.26]

$$J_e = ev_x \left[n(0) - n_o \right] \quad \text{(A.3)}$$

where v_x is the unilateral thermal velocity given by

$$v_x = \left(\frac{kT}{2m_c\pi}\right)^{\frac{1}{2}} \quad \text{(A.4)}$$

The n_o in (A.3) is the quasi-equilibrium electron density at $x = 0$ and can be expressed as

$$n_o = N_c\, e^{-\frac{e(V_D + V_n)}{kT}} \quad \text{(A.5)}$$

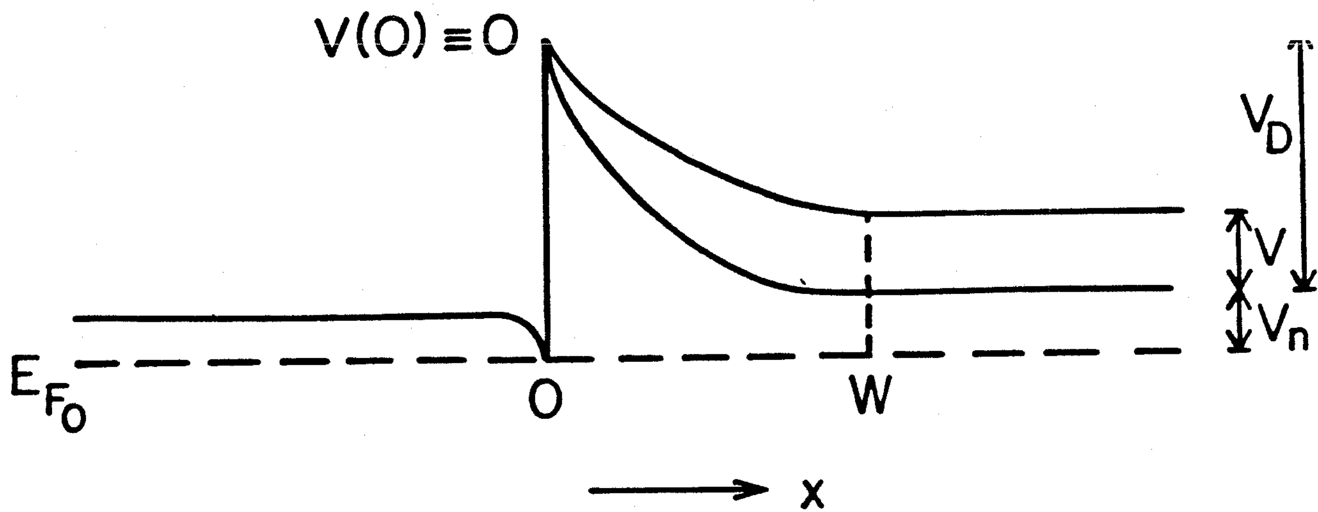

Figure 3.25. Schematic drawing of the band discontinuity at a "one-sided" heterojunction.

with V_n defined in Fig. 3.25 and N_c is the effective density of states of the high bandgap material. Eliminating n(0) from (A.2) and (A.3), and define

$$v_D = D_n \,/ \int_0^W \exp(-\frac{eV(x)}{kT})\, dx \tag{A.6}$$

we have finally

$$J_e = \frac{v_x N_c}{[1 + v_x / v_D]} e^{-\frac{e(V_D + V_n)}{kT}} [e^{\frac{eV}{kT}} - 1] \tag{A.7}$$

Generalizing from (A.7) to (3.5.4) and (3.5.5) is then straightforward.

References - Chapter 3

3.1 R. C. Goodfellow, A. C. Carter, G. I. Rees, and R. Davis, IEEE Trans. Elect. Dev., **ED-28** , p. 365 (1981)

3.2 T. Fukui and Y. Horikoshi, Jap. J. Appl. Phys., **18** , p. 961 (1979)

3.3 A. R. Adams, M. Asada, Y. Suematsu, and S. Arai, Jap. J. Appl. Phys., **19** , L621 (1980)

3.4 N. K. Dutta, R. J. Nelson, and P. A. Barnes, Elect. Lett., **16** , p. 653 (1980)

3.5 G. H. B. Thompson and G. H. Henshall, Elect. Lett., **16** , p. 42 (1980)

3.6 N. K. Dutta and R. J. Nelson, Appl. Phys. Lett., **38** , p. 407 (1981)

3.7 A. Sugimura, IEEE J. Quant. Elect., **QE-17** , p. 627 (1981)

3.8 L. C. Chiu, P. C. Chen, and A. Yariv, IEEE J. Quant. Elect., **QE-18** , p. 938 (1982)

3.9 M. Yano, H. Imai, and M. Takusagawa, J. Appl. Phys., **52** , p. 3172 (1981)

3.10 W. Ng and Y. Z. Liu, Elect. Lett., **18** , p. 693 (1982)

3.11 L. C. Chiu, K. L. Yu, S. Margalit, T. R. Chen, U. Koren, A. Hasson, and A. Yariv, to be published in IEEE J. Quant. Elect.

3.12 A. R. Beattie and P. T. Landsberg, Proc. R. Soc. London, Ser A, **249** , p. 16 (1958)

3.13 L. Huldt, Phys. Stat. Sol. (a), **24** , p. 221 (1974)

3.14 A. Sugimura, J. Appl. Phys., **51** , p. 4405 (1980)

3.15 P. Lawaetz, Phys. Rev B, **4** , p. 3460 (1971)

3.16 Y. Horikoshi and Y. Furukawa, Jap. J. Appl. Phys., **18** , p. 809 (1979)

3.17 G. H. B. Thompson, IEE Proc., **128** , pt 1, p. 37 (1981)

3.18 T. Uji, K. Iwanoto, and R. Lang, Appl. Phys. Lett., **38** , p. 193 (1981)

3.19 S. Yamakoshi, T. Sanada, O. Wada, I. Umebu, and T. Sakurai, Appl. Phys. Lett., **18** , p. 144 (1982)

3.20 S. Yamakoshi, T. Sanada, O. Wada, I. Umebu, and T. Sakurai, Gallium Arsenide and Related Compounds, Inst. Phys. Conf. Ser. (1981)

3.21 C. M. Wu and E. S. Yang, J. Appl. Phys., **49** , p. 3114 (1978)

3.22 P. J. Anthony and N. E. Schumaker, IEEE Elect. Dev. Lett., **EDL-1** , p. 58 (1980)

3.23 P. J. Anthony and N. E. Scumaker, J. Appl. Phys., **51** , p. 5038 (1980)

3.24 D. L. Scharfetter, Sol. Stat. Elect., **8** , p. 299 (1965)

3.25 H. C. Casey, Jr., and M. B. Panish, "Heterostructure Lasers," Pt. A, Chap. 4, Academic Press, New York (1978)

3.26 S. M. Sze, "Physics of Semiconductor Devices," Chap. 5, J. Wiley and Sons, New York (1981)

3.27 L. L. Chang, sol. Stat. Elect., **8** , p. 721 (1965)

3.28 S. R. Forrest, O. K. Kim, and R. G. Smith, Appl. Phys. Lett., **41** , p. 95 (1982)

3.29 G. E. Stillman, L. W. Cook, G. E. Bulman, N. Tabatabaier, R. Chin, and P. D. Dapkus, IEEE Trans. Elect. Dev., **ED-29** , p. 1355 (1982)

3.30 W. R. Frensley and H. Kroemer, Phys. Rev. B, **16** , p. 2642 (1977)

3.31 L. C. Chiu and A. Yariv, Jap. J. Appl. Phys., **21** , L305 (1982)

3.32 O. Wada, S. Yamakoshi, and T. Sakurai, Appl. Phys. Lett., **41** , p. 981 (1982)

3.33 All T_o values quoted in this section are the average of 4-6 lasers of each

category.

3.34 Y. Itaya, Y. Suematsu, S. Katayama, K. Kishino, and S. Arai, Jap. J. Appl. Phys., **18**, p. 1795 (1979)

3.35 R. Chin, N. Holonyak, Jr., B. A. Vojak, K. Hess, R. D. Dupuis, and P. D. Dapkus, Appl. Phys. Lett., **36**, p. 19 (1980)

3.36 M. I. Elinson, V. A Volkov, V. N. Lutskii, and T. W. Pinsker, Thin Film Solids, **12**, p. 383 (1972)

3.37 R. Fivaz, J. Phys. Chem. Solids, **28**, p. 839 (1967)

3.38 N. Holonyak, Jr., R. M. Kolbas, R. D. Dupuis, and P. D. Dapkus, IEEE J. Quant. Elect., **QE-16**, p. 170 (1980)

3.39 E. A. Rezek, N. Holonyak, Jr., and B. K. Fuller, J. Appl. Phys., **51**, p. 2402 (1980)

Chapter 4
Impact Ionization in III-V Semiconductor Compounds

4.1 Introduction

In an optical fiber communication link, the receiver performance is just as, if not more, important as that of the transmitter. An important class of semiconductor photodetectors is the Avalanche Photodiodes (APD). A unique feature of APD's is the built-in internal current gain provided through the mechanism of carrier multiplication in a high electric field region. This carrier multiplication increases the sensitivity of the detector substantially, since it reduces the relative value of the noise inevitably added by subsequent stages of amplification. Moreover, since multiplication occurs only at high electric field, the electrons and holes travel at their respective saturation velocities, leading to large gain-bandwidth product. As such, APD's are especially suited as receivers for low loss, high speed fiber communication in the spectral range of 1.3-1.6 μm. An understanding of the ionization process is thus essential in the selection of materials and design for high speed APD's.

However, the carrier multiplication mechanism that provides current gain also generates excess multiplication noise: the dark current and thermal noise are multiplied along with the signal. The excess noise generated depends critically on the ratio of the impact ionization coefficients of electrons and holes [4.1], and is the ultimate limiting factor for device performance at high gain.

For low excess noise, a large disparity in ionization coefficients of electrons and holes is desirable. A qualitative understanding of the underlying physics can

be gained by considering the simple case of electron injection at x=0 in a fully depleted high field region of length W. The electron and hole current equations are then given by

$$\frac{dI_e}{dx} = \beta I_h + \alpha I_e \tag{4.1.1}$$

and

$$I = I_e + I_h = \text{constant} \tag{4.1.2}$$

where I_h, I_e; β, α are the hole current, electron current, hole ionization and electron ionization coefficients respectively. Substituting (4.1.2) into (4.1.1), we have

$$\frac{dI_e}{dx} + (\beta - \alpha)I_e = \beta I \tag{4.1.3}$$

The multiplication factor for electrons, $M(= \frac{I_e(W)}{I_e(0)})$ is then derived from (4.1.3) to be

$$M = \frac{1}{\left[1 - \int_0^W \alpha\, e^{-\int_0^{x'} (\alpha - \beta) dx'} dx\right]} \tag{4.1.4}$$

When $\alpha = \beta$, (4.1.4) reduces to

$$M = \frac{1}{1 - \int_0^W \alpha dx} \tag{4.1.5a}$$

$$= \frac{1}{1 - W\alpha} \qquad (\text{ for } \alpha \neq f(x)\ ) \tag{4.1.5b}$$

We next consider the case when β=0. The equation for electron current is simply

$$\frac{dI_e}{dx} = \alpha I_e \tag{4.1.6}$$

and

$$M = e^{\int_0^W \alpha dx} \tag{4.1.7a}$$

$$= e^{\alpha W} \qquad (\text{for } \alpha \neq f(x)) \tag{4.1.7b}$$

From (4.1.5b), we see that high gain is obtained when $\alpha W \approx 1$. When $\alpha W \to 1$, $M \to \infty$, a phenomenon generally known as avalanche breakdown. The origin of this avalanche breakdown is the feedback effect where the generated secondary carriers are capable to create further electron-hole pairs. Therefore, in the case where both types of carriers are capable of impact ionization, each injected (or photo-excited) carrier generates only one electron-hole pair during its transit through the high field depletion region. Thus, on the average, only three carriers are present in the high field region at any instant (recall that $1/\alpha$ is the average distance a carrier travels before it undergoes impact ionization). Due to this small number of carriers, significant statistical fluctuations in carrier numbers are expected, leading to high excess noise. On the other hand, in the case of single carrier dominated impact ionization, (4.1.7b) shows that M just increases exponentially with αW, and no avalanche breakdown occurs. Thus, for high gain operation, $\alpha W >> 1$, and there are a large number of carriers in the depletion region at any instant. As a result, statistical fluctuations of the ionization process will only have minor effect on the total number of carriers, resulting in low excess noise.

For demodulation of optical signals with wavelengths $\lambda < 1\ \mu m$, silicon APD with large ratio of α/β is the ideal detector. Unfortunately, for λ in the range of 1.3-1.6 μm, suitable materials of Ge and most III-V semiconductor compounds have $\alpha \approx \beta$. Recently, Hildebrand et al [4.2] have investigated experimentally the carrier impact ionization coefficients in the ternary system of $Ga_{1-x}Al_xSb$ lattice matched to GaSb. An interesting and important result of their work is the enhanced β for $x \approx 0.052$ (i.e. for $E_g \approx \Delta$), leading to high ratio of β/α.

Unfortunately, no satisfactory explanation of their results has emerged, and the nature of the ionization processes is still a controversial subject. In the remaining sections of this chapter, impact ionization coefficients of electrons and holes in the $Ga_{1-x}Al_xSb$ system will be calculated and compared with experimental results. A possible explanation for the observed dependence of hole impact ionization coefficient on x will be discussed. In addition, an APD using quantum well effects with large β/α is proposed.

4.2 Electron and Hole Impact Ionization Coefficients

Impact ionization in direct III-V semiconductor compounds is essentially the reverse of the Auger process discussed in the previous chapter. An important distinction, however, is that in the present case, we are dealing with a non-thermal equilibrium system. Hill [4.3] has shown that the matrix elements for impact ionizations in the presence of an externally applied electric field is enhanced by a factor κ over the zero field case. However, for electric field strength $\mathcal{E} < 10^4$ V/cm, κ is essentially unity. Thus, for a comparison to Hildebrand's results ($\mathcal{E}$ in the range of $10^4 - 10^5$ V/cm), transition matrix elements used in chapter 3 are directly applicable, and will be employed to derive approximate expressions for the ionization coefficients.

In relatively weak fields ($10^4 - 10^5$ V/cm), the carriers that have gained enough energy to create an electron-hole pair are those "lucky" ones that have avoided colliding with phonons and other carriers [4.4] ("Ballistic electrons" is the terminology in common use today). Thus, the Shockley distribution [4.4] for electrons and holes can be assumed, and the carrier distribution f then takes the form of

$$f \sim e^{-\frac{E'_2}{e\mathcal{E}\lambda}} \tag{4.2.1}$$

where E'_2 is the energy of the initiating carrier (see Fig. 4.1), and λ is the carrier-optical phonon collision mean free path. The impact ionization coefficients are then given by [4.5]

$$\alpha, \beta = \int_{E_T}^{\infty} \frac{P(2')}{v_{sat}} e^{-\frac{E'_2}{e\mathcal{E}\lambda}} \frac{1}{e\mathcal{E}\lambda} dE'_2 \tag{4.2.2}$$

where E_T is the threshold energy for ionization, $P(2')$ is the ionization probability per unit time, and v_{sat} is the saturation velocity of the carriers.

In the high field region, the carrier concentration is low. In this case, the statistical factors that are important in the Auger process can be neglected. In these circumstances, $P(2')$ for electron initiated CHCC process is just

$$P(2') = \frac{2\pi}{\hbar} \frac{1}{(2\pi)^9} \int\int\int \left(\frac{4\pi e^2}{\varepsilon}\right)^2 \frac{4\alpha_{ch}}{E_g} \frac{k'^2_2}{|k'^2_2 + L_D^{-2}|^2} \tag{4.2.3}$$

$$\times\, \delta(\vec{k}_1 + \vec{k}_2 - \vec{k}_{1'} - \vec{k}_{2'})\, \delta(E_f - E_i)\, d\vec{k}_1 d\vec{k}_{1'} d\vec{k}_2$$

Assuming $k_1 \approx k_2$, and neglecting L_D^{-1} as compared to k'_2 (see Fig. 4.1a), the integration is straight forward and after some algebra, yields,

$$P(2') \approx \frac{\sqrt{2}\mu^{\frac{3}{2}}}{3\hbar} \left(\frac{e^2}{4\pi\varepsilon\hbar c}\right)^2 \left(\frac{m_c}{m_o}\right) \frac{E_p}{E_g^2} (m_c c^2) \frac{(E'_2 - E_g)^2}{E'_2} \tag{4.2.4}$$

Using (4.2.2), we have for α

$$\alpha \approx \frac{\sqrt{2}\mu^{\frac{3}{2}}}{3\hbar v_{sat}} \left(\frac{e^2}{4\pi\varepsilon\hbar c}\right)^2 \left(\frac{m_c}{m_o}\right) \frac{E_p}{E_g^2} (m_c c^2)\, e^{-\frac{E_T}{e\mathcal{E}\lambda}} \tag{4.2.5}$$

$$\times \left[(E_T - E_g)^2 + 2e\mathcal{E}\lambda(E_T - E_g) + 2(e\mathcal{E}\lambda)^2 \right]$$

where v_{sat} is the saturation velocity of electrons, and the threshold energy E_T is given by [4.6],

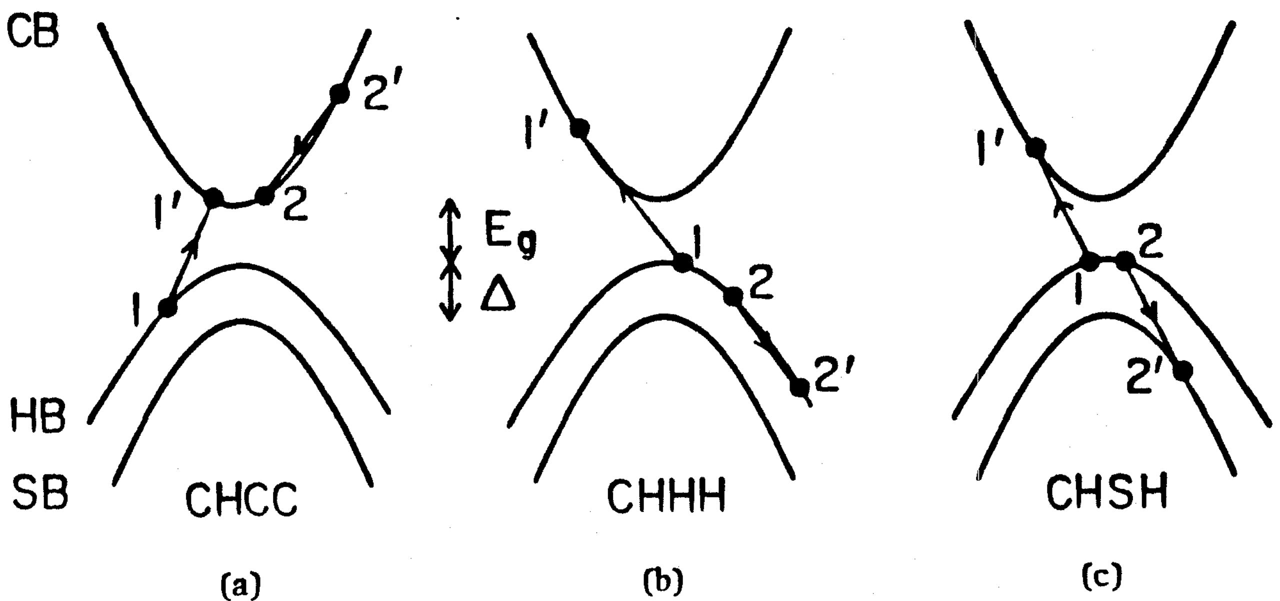

Figure 4.1 The three impact ionization processes: (a) electron initiated CHCC process, (b) heavy hole initiated CHHH process, and (c) split-off hole initiated CHSH process.

$$E_T = \left(\frac{1+2\mu}{1+\mu}\right)E_g \tag{4.2.6}$$

Similarly, for heavy hole initiated process (CHHH), we have

$$\beta_h \approx \frac{\sqrt{2}}{3\hbar v_{sat}}\mu^{\frac{3}{2}}\left(\frac{e^2}{4\pi\varepsilon\hbar c}\right)^2\left(\frac{m_h}{m_o}\right)\frac{E_p}{E_g^2}(m_h c^2)e^{-\frac{E_T}{e\mathcal{E}\lambda}} \tag{4.2.7}$$

$$\times\left[\,(E_T-E_g)^2+2e\mathcal{E}\lambda(E_T-E_g)+2(e\mathcal{E}\lambda)^2\,\right]$$

with

$$E_T = \left(\frac{2+\mu}{1+\mu}\right)E_g \tag{4.2.8}$$

For split-off hole initiated process (CHSH), if we neglect screening as in the previous case, then

$$\beta_s \approx \frac{8}{9\hbar v_{sat}}\left(\frac{e^2}{4\pi\varepsilon\hbar c}\right)^2\left(\frac{m_h}{m_o}\right)^2\mu^{\frac{1}{2}}\frac{E_p^2}{E_g^2\Delta(\Delta+E_g)}(m_c c^2)\,(e\mathcal{E}\lambda)\,e^{-\frac{E_T}{e\mathcal{E}\lambda}} \tag{4.2.9}$$

$$\times\left[\,(E_T-E_g)^2+2e\mathcal{E}\lambda(E_T-E_g)+2(e\mathcal{E}\lambda)^2\,\right]$$

The threshold energy in this case is [4.6]

$$E_T = E_g\left[\,1+\frac{2m_s(1-\Delta/E_g)}{2m_h+m_c--m_s}\,\right] \qquad \Delta < E_g \tag{4.2.10a}$$

$$E_T = \Delta \qquad \Delta \geq E_g \tag{4.2.10b}$$

where m_s is the split-off hole mass.

However, as can be seen from Figs. 4.2, L_D^{-2} cannot be neglected when $\Delta \geq E_g$. In constrast, it is $|\vec{k}_{2'}^2-\vec{k}_2^2|$ which can be neglected compared with L_D^{-2}. Normally, for non-degenerate systems in thermal equilibrium, the screening length L_D^{-2} is given by the familiar expression [4.7]

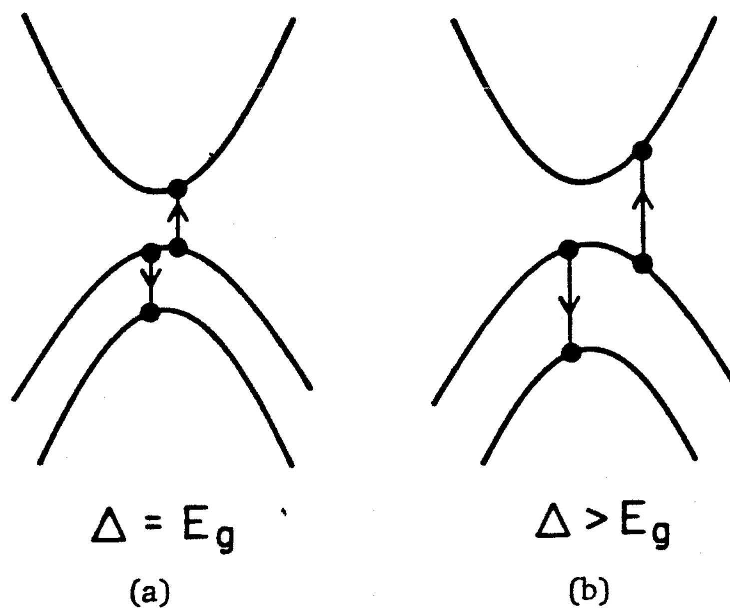

Figure 4.2 The split-off hole initiated CHSH process for: (a) $\Delta = E_g$ and (b) $\Delta > E_g$.

$$L_D^{-4} = \frac{8}{\pi}(kT)\left(\frac{e^2}{4\pi\varepsilon\hbar c}\right)^2\left(\frac{m_c}{\hbar^2}\right)^{\frac{3}{2}}\left(\frac{m_h}{\hbar^2}\right)^{\frac{3}{2}} e^{-\frac{E_g}{kT}} \tag{4.2.11}$$

However, for a non-equilibrium system, kT should be replaced by kT_c where T_c is the effective carrier temperature. Here, it is assumed that kT_c is approximately equal to $e\mathcal{E}\lambda$, a point that will be discussed further in the next section. In this case, we have instead

$$\beta_s \approx \frac{\pi}{12\hbar v_{sat}}\left(\frac{m_s}{m_o}\right)^2 \frac{E_p^2}{E_g^3\Delta(\Delta+E_g)} e^{-\frac{\Delta-E_g}{e\mathcal{E}\lambda}} \frac{(e\mathcal{E}\lambda)^2}{(1+\mu)^{\frac{3}{2}}} \tag{4.2.12}$$

$$\times\left[\,(\Delta-E_g)^2 + 8e\mathcal{E}\lambda(\Delta-E_g) + 20(e\mathcal{E}\lambda)^2\,\right]$$

for $\Delta > E_g$. Note that the exponential is now given by $e^{-\frac{\Delta-E_g}{e\mathcal{E}\lambda}}$. The significance of this form will become clear in the next section, when (4.2.5), (4.2.8), (4.2.9), and (4.2.12) are used to compare with the experimental results of [4.2].

Since the parameters λ and v_{sat} are not known accurately, they are used as fitting parameters in (4.2.5), (4.2.8), (4.2.9), and (4.2.12). λ is determined primarily from the slope of $\ln\beta$ vs $1/E$ plot, and v_{sat} is then adjusted to obtain the correct magnitude for α and β. If λ and v_{sat} needed to arrive at a reasonable agreement with experimental results fall in an unphysical range, then the validity of the expressions should be questioned. As a check, (4.2.5) and (4.2.11) have been applied to the case of InP. Data for α and β are taken from [4.8]. With $\lambda = 60$Å, 82Å and $v_{sat} = 1.2\times10^7$, 9×10^5 cm/sec for electrons and holes respectively, it can be seen from Fig. 4.3 that reasonable agreement is obtained between theory and experiment.

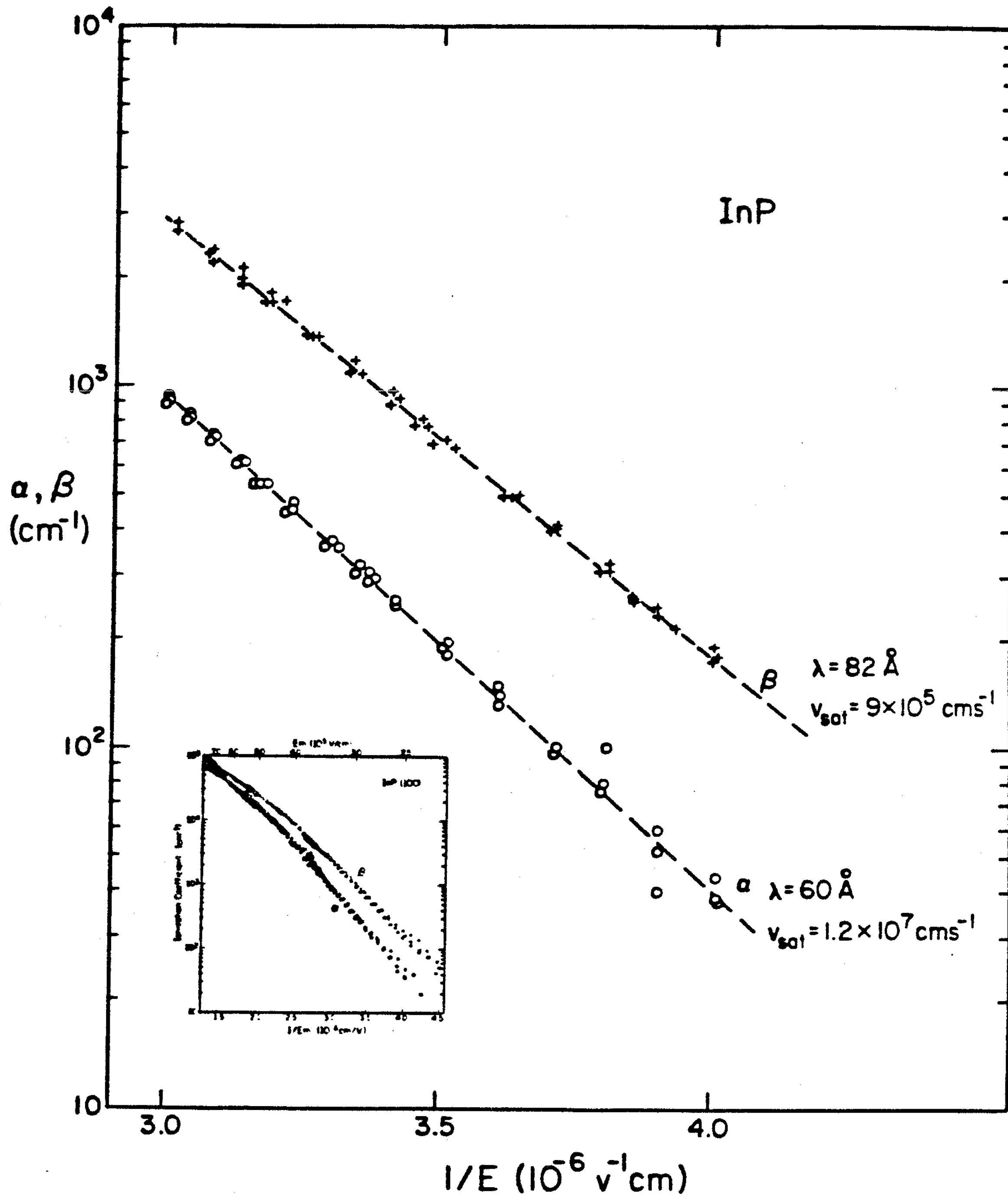

Figure 4.3 Comparison of experimental and calculated (dashed lines) electron and hole impact ionization coefficients for InP. The insert shows the original data from [4.8].

4.3 Resonant Enhanced Hole Impact Ionization in GaAlSb ?

Hildebrand et al [4.2] have investigated the impact ionization of electrons and holes in $Ga_{1-x}Al_xSb$ for various values of x, thereby changing the bandgap energy E_g and the ratio Δ/E_g. An interesting and important result of their work is the significant increase in β/α for $\Delta/E_g \approx 1$. This suggests that low noise APD can be fabricated from these materials.

The large value of β when $\Delta \approx E_g$ is attributed in [4.2] to the relaxation of the requirements of momentum and energy conservations, as shown in Figs. 4.2. The experimental results of [4.2] is reproduced in Fig. 4.4. As is normally done, Hildebrand et al expressed the ionization coefficient as

$$\alpha, \beta = \text{constant} \times e^{-\frac{E_T}{e\mathcal{E}\lambda}} \tag{4.3.1}$$

where the prefactor is assumed to be constant. However, when using (4.3.1), it was found that λ for holes depends strongly on Δ/E_g, and varies from 200–400Å. This is rather unphysical, since the initiating particle is always a heavy hole, which, in the case of CHSH process, is then scattered into the split-off hole band. The value of λ should therefore be close to that of the heavy holes and thus expected to be independent of Δ/E_g. Hildebrand et al found phenomenologically that a distribution of the form

$$f \sim e^{-\frac{\Delta - E_g}{e\mathcal{E}\lambda}} \tag{4.3.2}$$

gives rise to an almost constant λ. However, the origin of (4.3.2) was not understood. In fact, the use of (4.3.2) had been heavily criticized by Kasemset [4.9], who argued that (4.3.2) had no reasonable physical origin. More importantly, it deviates from the well accepted Shockley distribution of (4.2.1). Instead, in [4.9], impact ionization initiated by heavy holes is proposed when $\Delta > E_g$, which

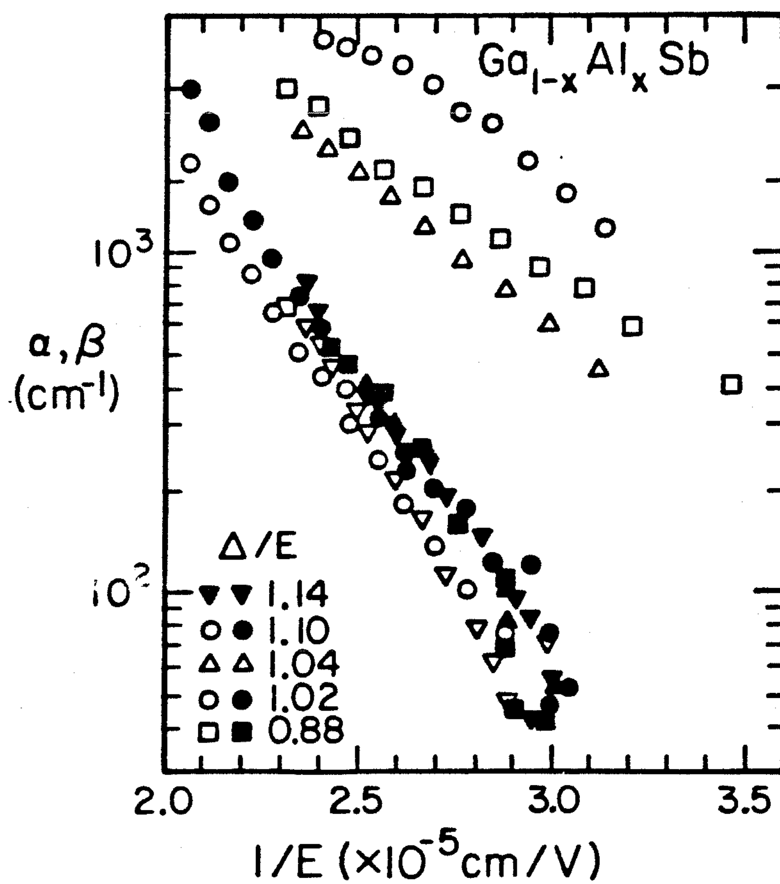

Figure 4.4 Experimental data of α and β for $Ga_{1-x}Al_xSb$ as measured in [4.2].

also results in a relatively constant λ. However, when the prefactor (which also depends on the applied field) is taken into account, due to the high threshold energy (see (4.2.9)), β calculated from (4.2.8) is too small compared with the experimental data. Furthermore, it seems more unreasonable to assume that the CHSH process dominates for $\Delta < E_g$, but is abruptly turned off when $\Delta > E_g$, as suggested by [4.9]. Kasemset's conclusion was based on a constant prefactor, as in [4.2]. However, it is clear from the previous section that the prefactor plays an equally important role, and should not be neglected.

As shown in section 4.2, we see that the form (4.3.2) emerges when screening is taken into account with the assumption $kT_c \sim e\mathcal{E}\lambda$. The calculated β using (4.2.12) is shown in Fig. 4.5, whereas Fig. 4.6 shows the dependence of β on Δ/E_g. It can be seen that reasonable agreement is obtained, which suggests that the most probable process is that initiated by the split-off hole (CHSH process). Also, it lends support to the assumption $kT_c \sim e\mathcal{E}\lambda$, and provides a path leading to the distribution of the form given by (4.3.2).

It should be pointed out that, strictly speaking, the enhancement of β is not due to any resonant phenomenon, since for $\Delta > E_g$, the threshold energy is always Δ, which only changes insignificantly from GaSb to AlSb. Moreover, simultaneous fulfillment of the requirements of energy and momentum conservation is always ensured when $\Delta > E_g$ (see Figs. 4.2), not only when $\Delta = E_g$.

4.4 Resonant Enhanced Hole Impact Ionization in Quantum Wells

Although as explained in the previous section, the enhancement at $\Delta = E_g$ is not resonant, a "resonant" enhanced β can nevertheless be achieved in a quantum well structure as shown in Fig. 4.7. In a quasi two dimensional system, the density of states is step-like [4.10] instead of the more familiar parabolic shape.

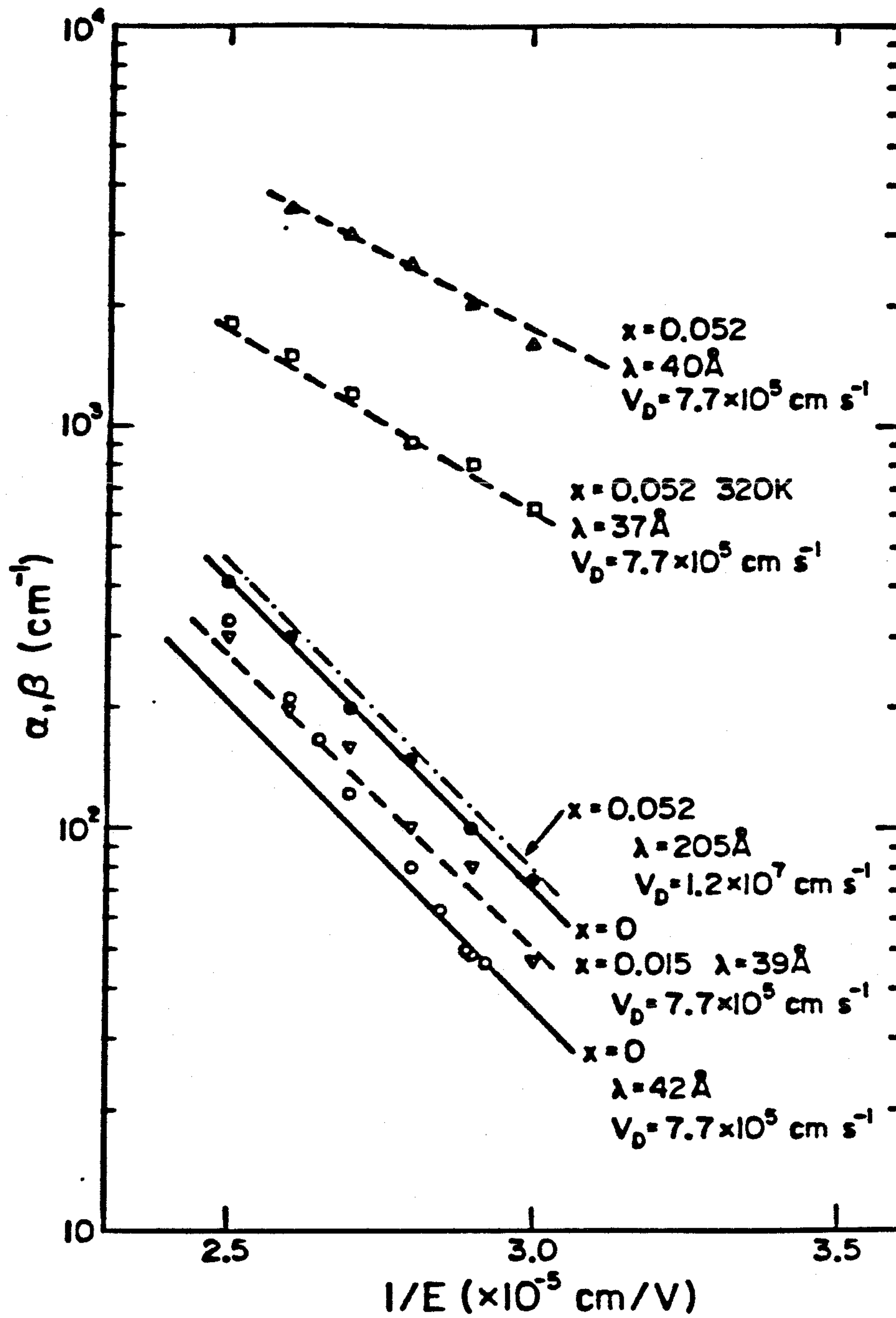

Figure 4.5 Comparison of experimental and calculated impact ionization coefficients for electrons and holes in $Ga_{1-x}Al_xSb$. Data taken from [4.2].

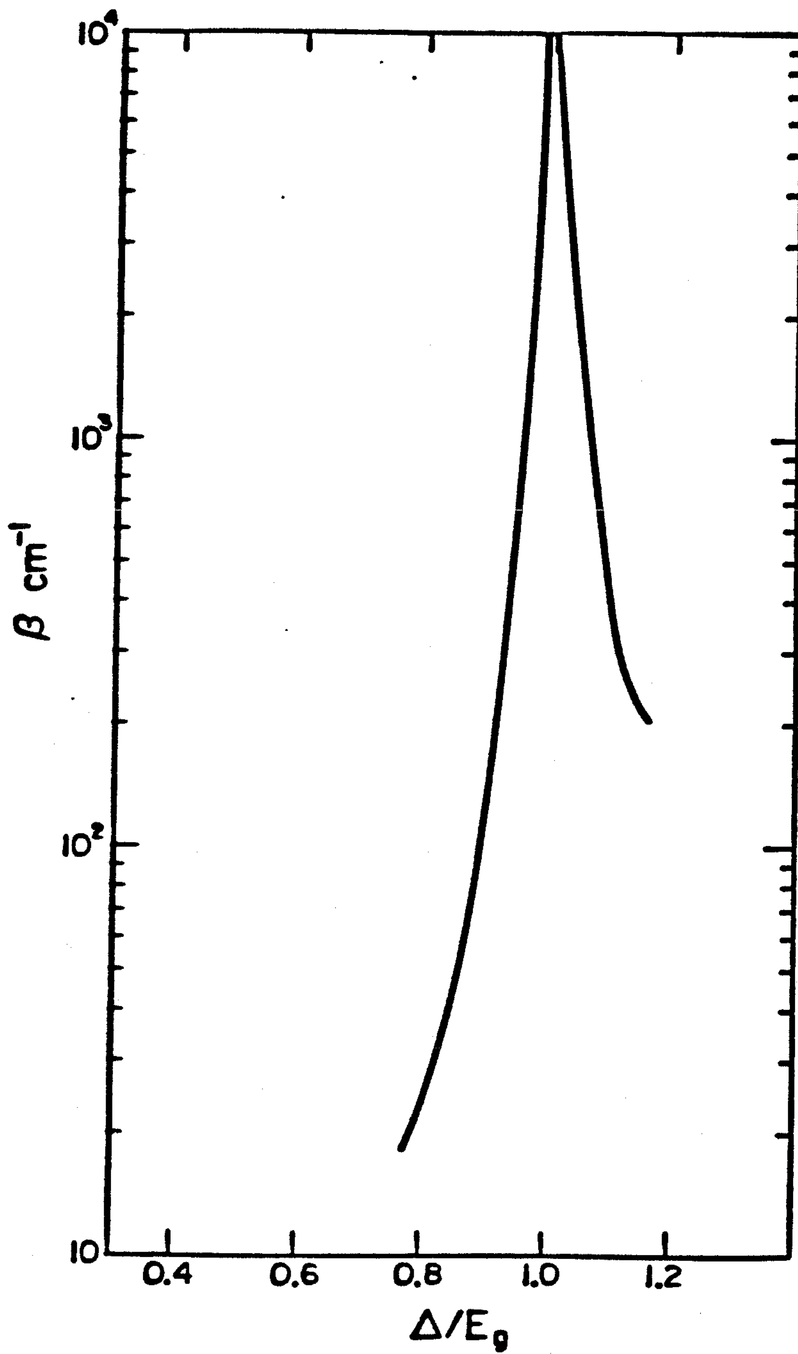

Figure 4.6 The hole impact ionization coefficient in $Ga_{1-x}Al_xSb$ system as a function of Δ/E_g.

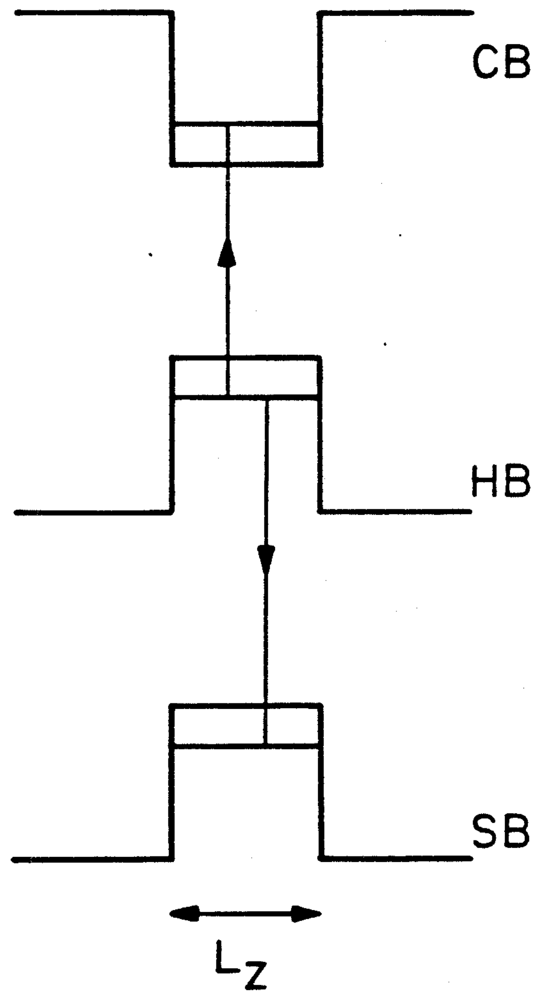

Figure 4.7 **Band structure of the proposed quantum well configuration.**

More importantly, the density of states is finite even for the lowest lying confined state, as opposed to zero in three dimensional bulk material at band extremum. Therefore, an enhancement in β when $\Delta \approx E_g$ is expected. Moreover, for the structure shown in Fig. 4.7, the electron impact ionization is expected to be suppressed (chapter 3) due to the more stringent condition of momentum and energy conservation in a quasi two dimensional system. Thus the ratio β/α is expected to be greatly enhanced in a quantum well structure, and a single carrier dominated impact ionization APD with low noise is then possible.

For an order of magnitude estimate of the enhancement in β, only the density of states is modified, and the same approach utilized in section 4.2 is followed. In addition, only one confined level is taken into account for each of the three bands involved. β_{q2d} for the quasi two dimensional case is then given approximately by

$$\beta_{q2d} \approx \frac{64\pi^3}{\hbar v_{sat}} \left(\frac{m_c m_s}{m_o^2}\right) \frac{E_p^2}{E_g^3 \Delta(\Delta+E_g)} \frac{1}{1+\mu} \left(\frac{\hbar c}{L_z}\right)^2 \frac{(m_c c^2)^{\frac{1}{2}}}{(m_h c^2)^{\frac{3}{2}}} e^{-\frac{\Delta-E_g}{e\mathcal{E}\lambda}} \qquad (4.4.1)$$

where L_z is the width of the quantum well. The ratio $\frac{\beta_{q2d}}{\beta_{3d}}$ is then given approximately by

$$\frac{\beta_{q2d}}{\beta_{3d}} \approx \frac{192\pi^2}{5} \left(\frac{m_c}{m_s}\right)(1+\mu)^{\frac{1}{2}} \left(\frac{\hbar c}{L_z}\right)^2 \frac{(m_c c^2)^{\frac{1}{2}}}{(m_h c^2)^{\frac{3}{2}}} \frac{1}{e\mathcal{E}\lambda} \qquad (4.4.2)$$

For $L_z = 100Å$, $\mathcal{E} = 4\times10^4$ V/cm, $\lambda = 40Å$, $m_c = .07m_o$, $m_h = .37m_o$, $m_s = .14m_o$, (4.4.2) gives $\frac{\beta_{q2d}}{\beta_{3d}} \approx 12$. Thus the hole impact ionization coefficient is expected to be enhanced by an order of magnitude, suggesting the possibility of fabricating low noise, high performance quantum well APD.

References - Chapter 4

4.1 R. J. McIntyre, IEEE Trans. Elect. Dev., **ED-13** , p. 154 (1966).

4.2 O. Hildebrand, W. Kuebart, K. W. Benz, and M. H. Pilkuhn, IEEE Jour. Quant. Elect., **QE-17** , p. 284 (1981).

4.3 D. Hill, Jour. Phys. C: Sol. Stat. Phys., **9** , p. 3527 (1976).

4.4 W. Shockley, Sol. Stat. Elect., **2** , p. 35 (1961).

4.5 D. J. Robbins, Phys. Stat. Sol. (b), **98** , p. 11 (1980).

4.6 T. P. Pearsall, R. E. Nahory, and J. R. Chelikowsky, Inst. Phys. Conf. Ser., **33**b , p. 331 (1977).

4.7 A. Haug, Sol. Stat. Elect., **21** , 1281 (1978).

4.8 G. E. Stillman, L. W. Cook, G. E. Balman, N. Tabatabaie, R. Chin, and P. D. Dapkus, IEEE Trans. Elect. Dev., **ED-29** , p. 1355 (1982).

4.9 D. Kasemset, IEEE Jour. Quant. Elect., **QE-17** , p. 1595 (1981).

4.10 For example, see N. Holonyak, Jr., R. M. Kolbas, R. D. Dupuis, and P. D. Dapkus, IEEE Jour. Quant. Elect., **QE-16** , p. 170 (1980).

Chapter 5
Quantum Well Infrared Detectors

5.1 Introduction

The capability of Molecular Beam Epitaxy (MBE) [5.1] and Metal-Organic Chemical Vapor Deposition (MO-CVD) for growing ultra thin epitaxial layers and their added flexibilities in precise control over doping profiles have extended the bounds of device research to new realms. These techniques make possible the direct observation of the quantized size effects when the width of the quantum-well or period of superlattice is on the order of the carrier de Broglie wavelength. In this chapter, approximate calculations of the phonon-assisted free carrier absorption, the phononless free carrier absorption, and inter-valence band absorptions in a single quantum-well will be presented. It is found that the free carrier and intervalence band absorptions are enhanced in the quasi two dimensional system. The possibility of employing such structures as infrared solid state detectors will be discussed. These proposed detectors are similar to Schottky barrier and extrinsic semiconductor photodetectors. The similarities and differences are compared. Two generic types of detectors will be considered: (1) Free electron absorption detectors; and (2) Intervalence band absorption detectors.

5.2 Free Carrier Absorption in GaAs/GaAlAs Quantum Wells

Free carrier absorption in polar semiconductors has been investigated in the literature [5.2]. Most theoretical calculations have been restricted to the non-degenerate case where the application of Boltzman statistics leads to analytical

results. In view of the high density of electrons possible in a modulation-doped structure [5.3], we have proceeded to calculate numerically the free carrier absorption by using Fermi statistics. Following [5.4], the absorption coefficient in polar semiconductor can be written as

$$\alpha_{\pm} = \left(\frac{e^2}{4\pi\varepsilon_o \hbar c}\right)\frac{a_{pol}}{3\pi\omega^3}\left(\frac{2\hbar\omega_o}{m_c}\right)^{\frac{3}{2}}\left(\frac{2m_c kT}{\hbar^2}\right)\left[N_q + \frac{1}{2} \mp \frac{1}{2}\right] \tag{5.2.1}$$

$$\times\int_0^{\infty}\left[\ln\left(\frac{1}{\alpha_c} + e^{-z_{\mp}} e^{\frac{1}{2}\left(x + \frac{z_{\mp}^2}{x}\right)}\right) - \left(\frac{z_{\mp}^2}{2x} - z_{\mp} + \frac{x}{2}\right)\right]\left(\frac{x}{x + q^2}\right)dx$$

where e is the electronic charge, ε_o is the permittivity of free space, ω_o is the optical phonon frequency, ω is the frequency of incident radiation, m_c is the conduction band effective mass, T is the temperature, N_q is the occupation number of phonons, $\frac{1}{\alpha_c} = e^{\frac{E_f}{kT}}$ with E_f the Fermi level, a_{pol} is the dimensionless coupling constant given by

$$a_{pol} = \left(\frac{e^2}{4\pi\varepsilon_o \hbar c}\right)\left(\frac{m_c c^2}{2\hbar\omega_o}\right)^{\frac{1}{2}}\left(\frac{1}{\kappa_\infty} - \frac{1}{\kappa_o}\right) \tag{5.2.2}$$

with κ_∞ the dielectric constant at optical frequency and κ_o is the static dielectric constant;

$$z_{\pm} = \frac{(\hbar\omega \pm \hbar\omega_o)}{2kT} \tag{5.2.3}$$

and

$$q^2 = \frac{\hbar^2 L_D^{-2}}{4m_c kT} \tag{5.2.4}$$

where L_D is the screening length. The subscript $\pm$ denotes phonon creation and annihilation respectively. Although the integrand appears to be singular for x=0, ∞, a closer look will reveal that it is well behaved and is zero for both x=0 and ∞. In fact, for $\hbar\omega \sim$ .2-.4 eV, most of the contribution to $\alpha_{\pm}$ comes from the vicinity

of $x = z_{\pm}$ where the integrand assumes its maximum value. The process of induced emission of light can be shown to be negligible in comparison to the absorption given above, and is neglected.

In a single quantum-well with discrete confined states, if we assume the incident photon has energy larger than the potential-well barrier and thus the final state of the electron is in the continuum band, then the ratio of the coefficient for free carrier absorption is given approximately by

$$\frac{\alpha_{3D}}{\alpha_{Q2D}} \approx \left(\frac{m_c kT}{2\pi\hbar^2}\right)^{\frac{1}{2}} \times \frac{L}{N} \tag{5.2.5}$$

where L is the width of well and N is the number of confined states. For most cases, it can easily be verified from (5.2.5) that the absorption in the quasi two dimensional system is considerably larger. Calculated values at 77 °K are presented in Fig. 5.1. The calculation is based on the GaAs-$Ga_{0.7}Al_{0.3}As$ system, which would be sensitive to radiation at about 4μm. Although the calculations in this work are carried out for single quantum-well only, the energy band in the case of uncoupled multiple quantum-well structures can be shown to be very narrow [5.5,5.6], and the results given here will approximately be valid for such structures too.

5.3 Phononless Free Carrier Absorption in Quantum Wells

In GaAs, the normal phonon-assisted free electron absorption in a quantum well was found in the last section to be enhanced by a factor of 3-5 over its bulk value. Despite this enhancement, the coefficient of free carrier absorption, α, is still quite small. In this section, it will be shown that phononless free carrier absorption in a quantum well structure is possible, with further enhancement in the absorption coefficient.

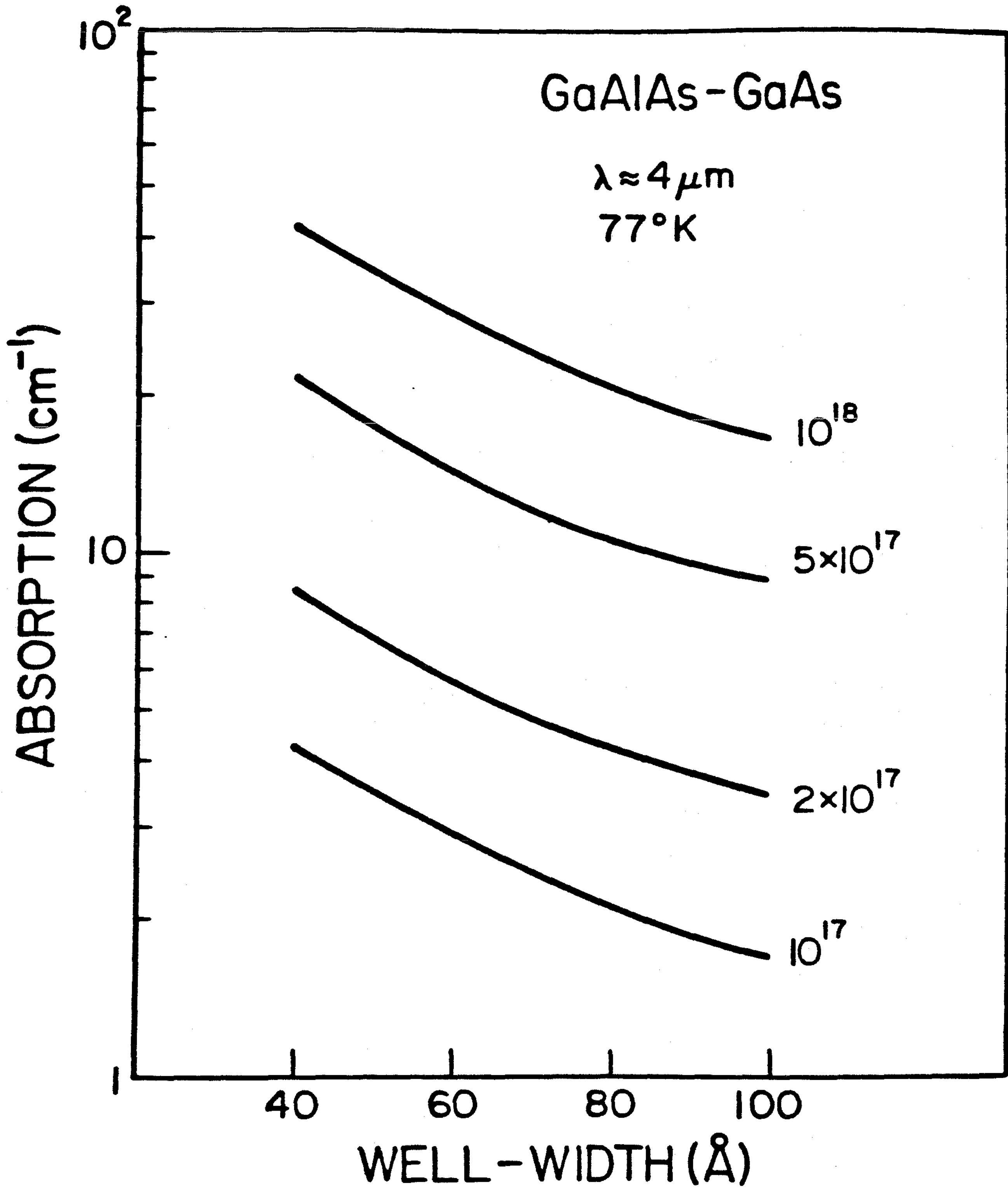

Figure 5.1 Calculated coefficient of free electron absorption at 77 °K for different electron concentrations.

In this section, an approximate calculation for α_f^{pl} due to phononless free carrier absorption in a quantum well will be presented. Estimated values for α_f^{pl} were over an order of magnitude larger than the phonon-assisted case. This is expected since the transition matrix element is now first order as compared to the second order phonon-assisted process.

To demonstrate the effect of phononless free electron absorption, an order of magnitude calculation for the absorption coefficient α_f^{pl} in a single quantum well was performed. If the actual superlattice structure is such that the wells are effectively decoupled (which is desirable to minimize the dark current in a detector), then the present result will also be a reasonable estimate for α_f^{pl} in such constructions.

Approximating the electron wave functions by

$$\psi_i = \sqrt{\frac{2}{LA}}\, u_i(\rho)\, e^{i\vec{k}\cdot\vec{\rho}} \sin\frac{\pi x}{L} \tag{5.3.1}$$

$$\psi_f = \frac{1}{\sqrt{V}}\, u_f(\rho)\, e^{i\vec{k}'\cdot\vec{\rho}}\, e^{ik_x x} \tag{5.3.2}$$

where L is the width of well, LA=V is the volume of the well, $\vec{\rho}$ is the radius vector in the plane of the heterojunction (y-z plane), $\vec{k}$ the electron wave vector, u the periodic part of the Bloch function, and the subscripts i,f denote the initial and final states respectively. The interaction Hamiltonian is then given by

$$H_{fi} = -\frac{ie\hbar A_o\sqrt{2}}{2m_oV}\int u_f^*(\rho)e^{-i\vec{k}'\cdot\vec{\rho}}e^{-ik_x x}\,(\hat{e}_o\cdot\nabla)\,u_i(\rho)e^{i\vec{k}\cdot\vec{\rho}}\sin\frac{\pi x}{L}\,d\vec{\rho}\,dx \tag{5.3.3}$$

where A_o is the vector potential of the incident radiation field, m_o the mass of free electron, and $\hat{e}_o$ is the unit polarization vector of the electromagnetic field.

Invoking the periodicity of the crystal in the y-z plane, (5.3.3) can be simplified to

$$H_{fi} = \frac{eA_o\sqrt{2}}{2m_oL} P_{fi} \int_0^L \sin\frac{\pi x}{L} e^{-ik_x x} dx \qquad (5.3.4)$$

with the familiar condition for conservation of crystal momentum $\vec{k}' = \vec{k}$. The momentum matrix element P_{fi} in (5.3.4) is given by

$$P_{fi} = -\frac{i\hbar}{A'} \int_{uc} (\hat{\epsilon}_o \cdot \hat{\rho})\, u_f^*(\rho) \frac{\partial}{\partial \rho} u_i(\rho)\, d\vec{\rho} \qquad (5.3.5)$$

where A' is now the area of the "unit cell" in the y-z plane, uc denotes unit cell, and the integration extends over one unit cell only in the y-z plane.

It follows immediately from (5.3.4) and (5.3.5) that the incident field would couple strongly only when the radiation is polarized in the y-z plane. Also, it is apparent from (5.3.4) that H_{fi} is finite unless k_x lies in the neighborhood of $\frac{m\pi}{L}$ with m an odd integer. Therefore, the structure can be designed to yield a finite H_{fi}, and thus results in phononless free carrier absorption. Maximum coupling occurs near the vicinity of $\frac{m\pi}{L}$ when m is an even integer. For $GaAs/Ga_{.7}Al_{.3}As$ system designed to detect IR radiation around 4 μm, with $L \approx 100\mu m$, energy conservation dictates that m is around 2.5. The absorption coefficient is then given approximately by (see appendix B)

$$\alpha^{pl} \approx \frac{0.048}{\varepsilon_o \hbar c n_r} \frac{2}{m_o \hbar\omega} |P_{fi}|^2 \left(\frac{m_c}{m_o}\right) \frac{1}{L} \left[1 - e^{-\frac{n\pi\hbar^2 L}{m_c kT}}\right] \qquad (5.3.6)$$

where ε_o is the permittivity of free space, n_r the refractive index ($\approx$ 3) and n the electron concentration. To provide an order of magnitude estimate for α^{pl}, the momentum matrix element was assumed to be the form given in [5.7]. The calculated α^{pl} as a function of n at 77 and 300 °K are shown in Fig. 5.2. Compared to the phonon-assisted process (Fig. 5.1), it can be seen that the coefficient is more than an order of magnitude larger.

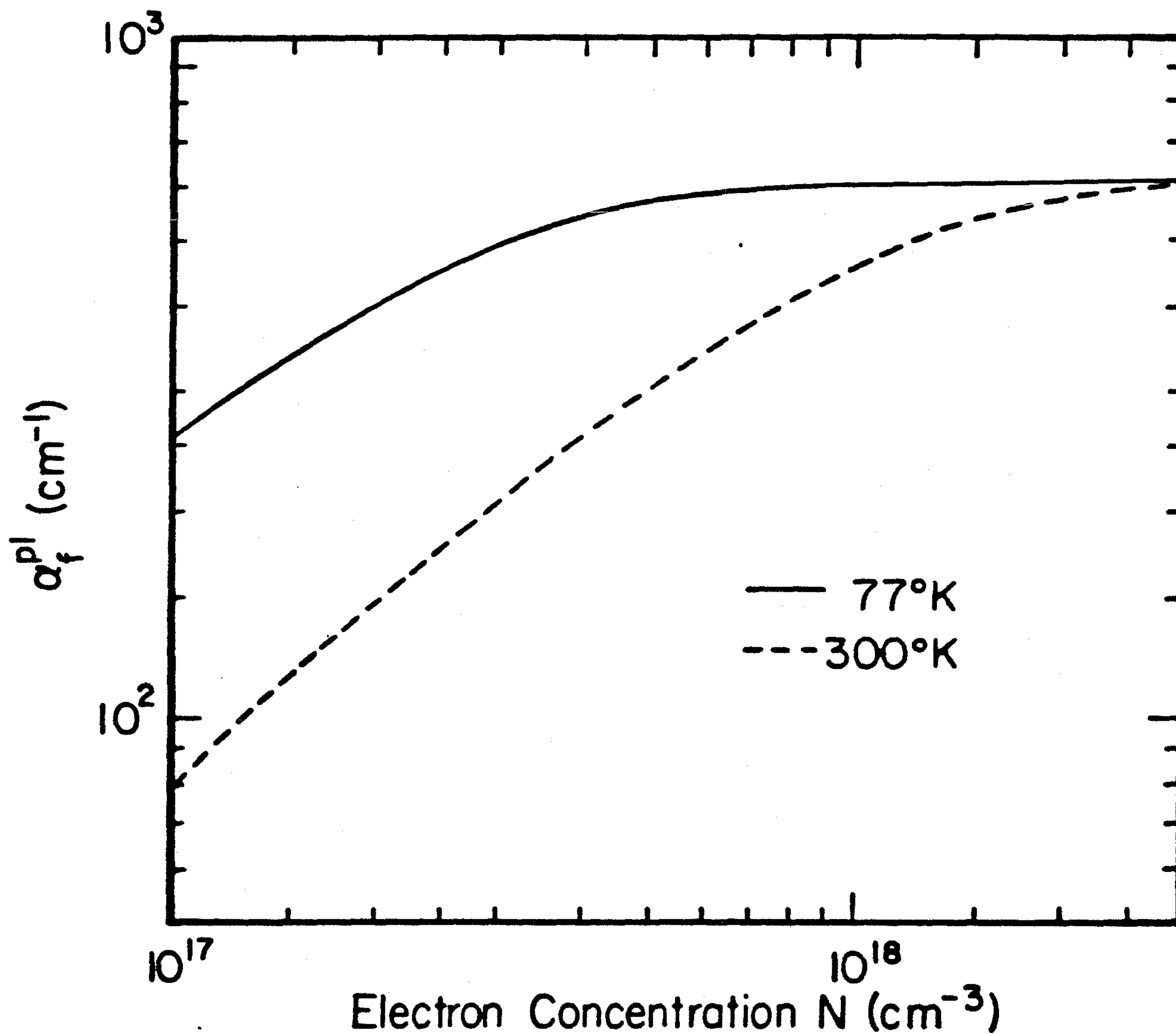

Figure 5.2 Calculated phononless free electron absorption coefficient as a function of electron concentration at 77 and 300 °K.

This enhanced phononless free carrier absorption has some significant implications. A necessary requirement according to (5.3.5) is that the radiation field be polarized in the plane of the heterojunction for strong coupling. A more important consequence is that excited electrons will continue to travel in the x direction, and when an external field is applied, a significant fraction of the excited electrons will be pulled out of the well region (see Fig. 5.4), thereby increasing the sensitivity and efficiency of the detector. The importance of this would be realized when compared to the phonon-assisted case, where the phonon absorption/emission process also randomized the electron momentum. In addition, the increased efficiency and absorption indicate that a surface detector is quite feasible, with the possibility of fabricating a detector array.

5.4 Intervalence Band Absorption

The radiative absorption coefficient α for transition between heavy and split-off hole bands can be written as [5.8,5.9, or appendix B]

$$\alpha = \frac{n}{c}\int\!\!\int\!\!\int W(k)\,(f_s - f_h)\,\frac{2d^3k}{(2\pi)^3} \qquad (5.4.1)$$

with

$$W(k) = \frac{2\pi}{\hbar}\left[\frac{e^2}{4\pi\varepsilon_0}\,\frac{2\pi\hbar^2}{n^2(\hbar\omega)}\,\frac{\langle M^2\rangle}{m^2}\right]\delta[E_h(k)-E_s(k)-\hbar\omega] \qquad (5.4.2)$$

$$f_h = \frac{1}{1+e^{\frac{E_h(k)-E_{fv}}{kT}}}, \qquad f_s = \frac{1}{1+e^{\frac{E_s(k)-E_{fv}}{kT}}} \qquad (5.4.3)$$

$$E_h(k) = -\frac{\hbar^2k^2}{2m_h}, \qquad E_s(k) = -\Delta - \frac{\hbar^2k^2}{2m_s}$$

where $\langle M^2\rangle$ is the optical matrix element, n the refractive index, E_{fv} is the hole quasi-fermi level, m_h and m_s are the heavy hole and split-off hole effective masses respectively, and Δ is the spin-orbit splitting gap. In three dimensions,

due to the density of states, $\alpha \sim \frac{(\hbar\omega-\Delta)^{\frac{1}{2}}}{\hbar\omega}$, and thus the absorption is very small for $\hbar\omega \approx \Delta$. However, in quasi-two dimensional system, due to the finite density of states for the lowest lying confined states, α can be approximated by (for $\hbar\omega \approx \Delta$)

$$\alpha = \frac{\pi}{3n}\left(\frac{1}{137}\right)\frac{\langle M^2 \rangle}{\hbar\omega}\frac{m^*}{m}\frac{1}{L} \times \left[\frac{1}{1+e^{-\frac{\Delta+E_{fv}}{kT}}} - \frac{1}{1+e^{-\frac{E_{fv}}{kT}}}\right] \tag{5.4.4}$$

where $\frac{1}{m^*} = \frac{1}{m_s} - \frac{1}{m_h}$. The matrix element $\langle M^2 \rangle$ is estimated approximately as described in [5.9]. The calculated absorption for the InAlAs-InP system at different hole concentrations and at 300 and 77 °K is shown in Fig. 5.3. Here, because the optical transition is direct, the absorption coefficient is much larger than the free carrier absorption.

5.5 Multi- Quantum Well Infrared Detector

In this section, two structures using the free carrier and intervalence band absorptions as near infrared photodetectors are proposed. Figs. 5.4(a)-(b) show a structure employing the modulation-doped technique so that only one side of the well is doped and the structure is graded to produce the configuration shown. In such structure, the internal electric field in the space charge region near the junction can be very high and is estimated to be 10^5 V/cm [5.6]. The basic idea here is that this field will aid in drawing the electrons excited by the incident radiation out of the well, resulting in a current flowing in the external circuit. The principle of operation of this detector is similar to that of the Schottky barrier photodetector [5.10], although there exist some subtle differences. In the case of the Schottky detector, the absorption is large. However, the effective thickness of the absorbing film is very thin, since only those

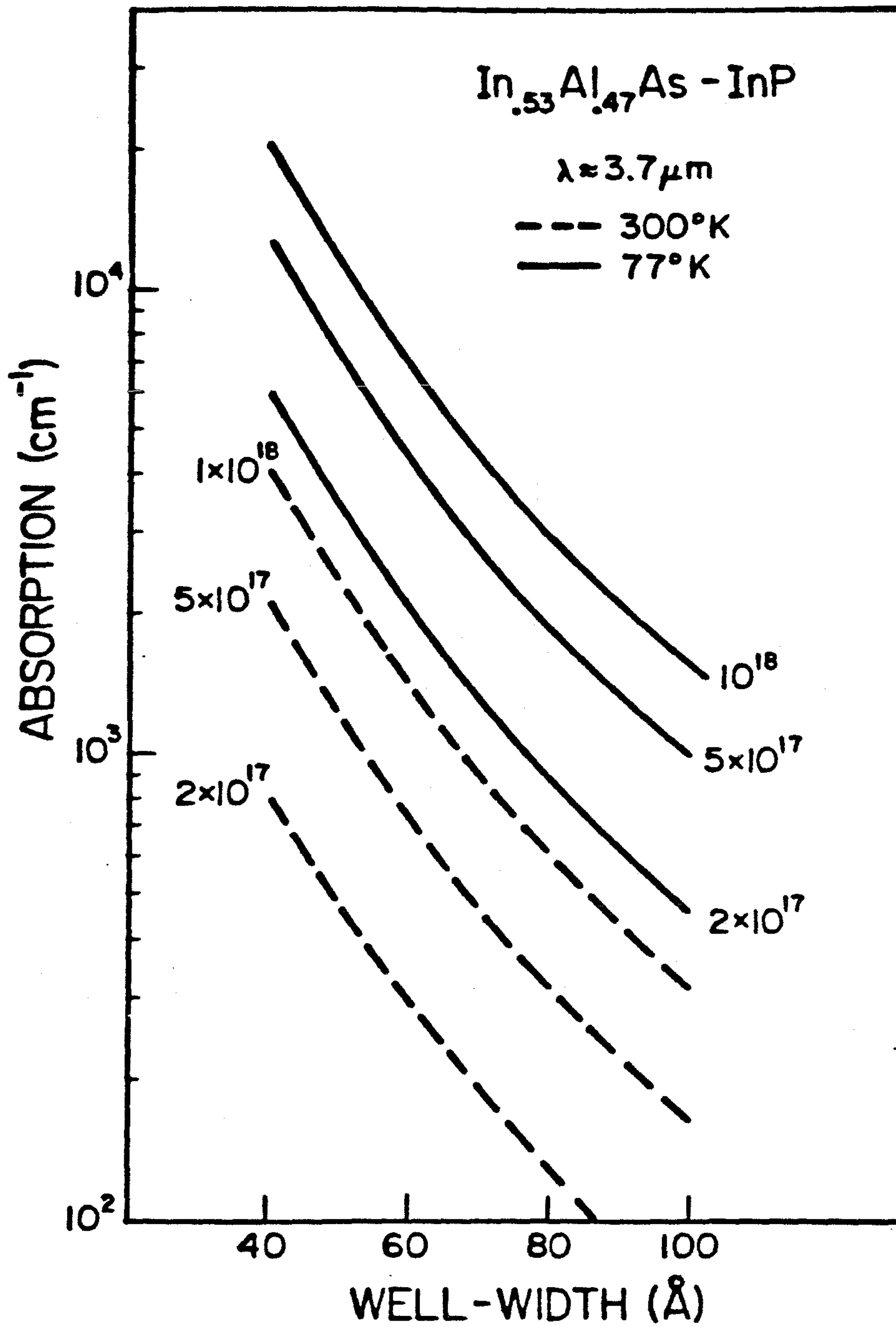

Figure 5.3 Calculated coefficient of intervalence band absorption at 77 and 300 °K for three different hole concentrations.

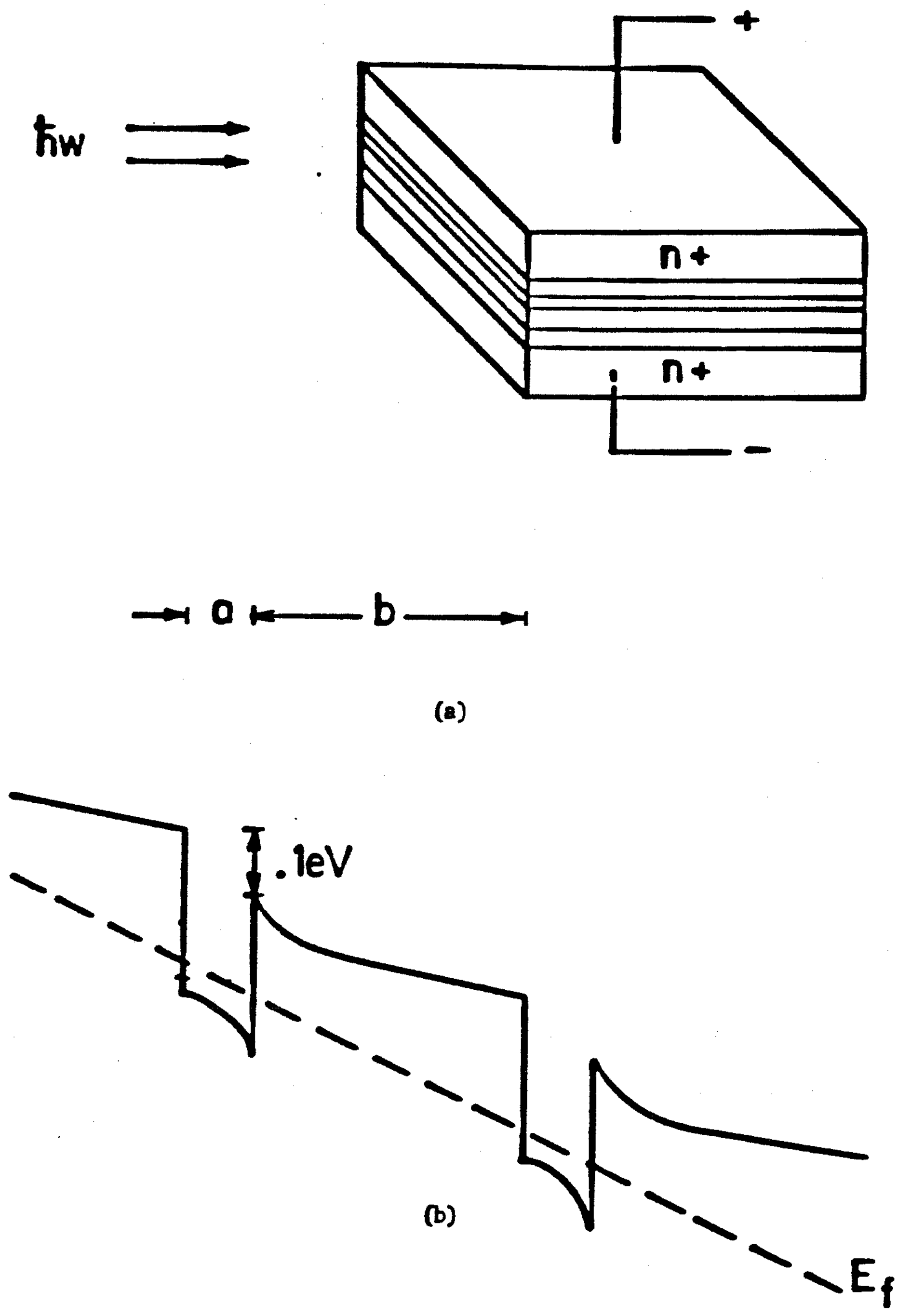

Figure 5.4 (a) A schematic drawing of the proposed detector.

(b) Band diagram of the proposed structure.

excited carriers which are within a diffusion length of the metal-semiconductor interface will have a chance of surmounting the barrier. Moreover, the distribution of the excited carriers will be essentially isotropic, leading to very small transmission coefficient [5.11]. In the quantum-well detector, the internal electric field renders the distribution anisotropic and peaked in the direction of the field. Thus, the probability of transmission is greatly enhanced. Also, for well width below $\sim 100\text{Å}$, the probability of traversing the well is estimated to exceed 0.9 (assuming the electron-phonon mean free path to be 200 Å), when the electrons are launched "hot" into the well (see Fig. 5.4(b)). Hence the photo-current can be increased by employing the multiple well structure. Also, the Al content in the outer contacting layers can be adjusted so that the central absorbing region is enclosed by a "waveguide" [see Fig. 5.4(a)]. This, coupled with the enhanced transmission probability and multiple well structure, will compensate for the small absorption coefficient.

For the intervalence band absorption, the schematic of the desired structure is shown in Fig. 5.5(a). Here, the basic idea is the same as the former case, except the role of electrons is now replaced by the holes. In this case, because of the resonance nature of the absorption, it is similar to the impurity semiconductor detector [5.11]. The materials chosen to form the heterostructure has to provide adequate confinement for holes in the valence band to minimize dark currents. The step in the split-off hole band should be very small (preferably only one confined state exists), so that the excited holes could be pulled out under an externally applied bias. Denoting the regions by subscripts 1 and 2, the appropriate condition that should be met (Fig. 5.5(b)) can be formulated as follows:

Figure 5.5

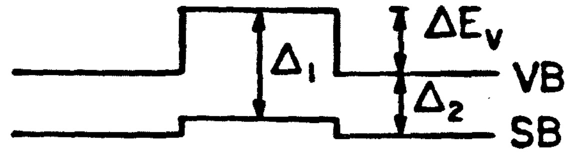

(a) Required band structure using the intervalence band absorption as detector.

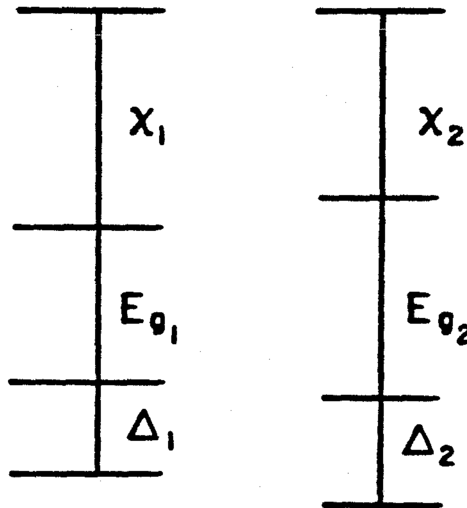

(b) Conditions to be satisfied for the heterostructures to operate as a detector.

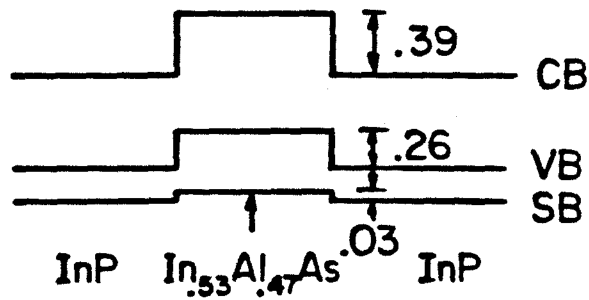

(c) Band diagram for the lattice matched $In_{.53}Al_{.47}As$-InP system.

$$(\chi_2+E_{g2}+\Delta_2) - (\chi_1+E_{g1}+\Delta_1) \le \left(\frac{\pi\hbar}{L}\right)^2 \frac{1}{2m}$$

$$(\chi_2+E_{g2}) - (\chi_1+E_{g1}) \approx .2\text{–}.3\text{eV} \qquad (5.5.1)$$

$$\Delta_1 \approx \hbar\omega$$

where χ is the electron affinity, and E_g the bandgap. Using published values, we found that for $In_{.53}Al_{.47}As$ lattice matched to InP, the band structure is as shown in Fig. 5.5(c), and it can be seen that the conditions stated in (5.5.1) are nearly met.

The efficiency of the detectors depends on the ratio of a/b, where a and b are defined in Fig. 5.4(b). Here a and b are chosen so that the wells are uncoupled to prevent tunneling currents. Preliminary experimental results on a device of the free electron absorption type show a strong response in the near infrared region. The device consists of twenty alternating layers of GaAs/GaAlAs quantum-wells with b/a $\approx$ 4 grown by MBE. The current-voltage characteristic of the device is shown in Fig. 5.6. Incident power was estimated to be approximately 10^{-8} watts.

5.6 Proposed Infrared Detector Using Inter-Subband Absorption and Tunneling

In this section, new types of quantum well infrared detectors which would provide improved sensitivity by utilizing inter-subband absorption rather than free carrier absorption are proposed.

Schematic drawings of the band (conduction) structures of the proposed detectors are shown in Figs. 5.7(a)-(b). Adjacent to the GaAs well region is a layer of $Ga_xAl_{1-x}As$ followed by a thick $Ga_yAl_{1-y}As$ barrier layer, with $x > y$ to provide a thin tunneling barrier for electrons in band E_f. The periodicity, a, of the structure is given by L+d+b. In Fig. 5.7(b), region III is tapered, and this structure

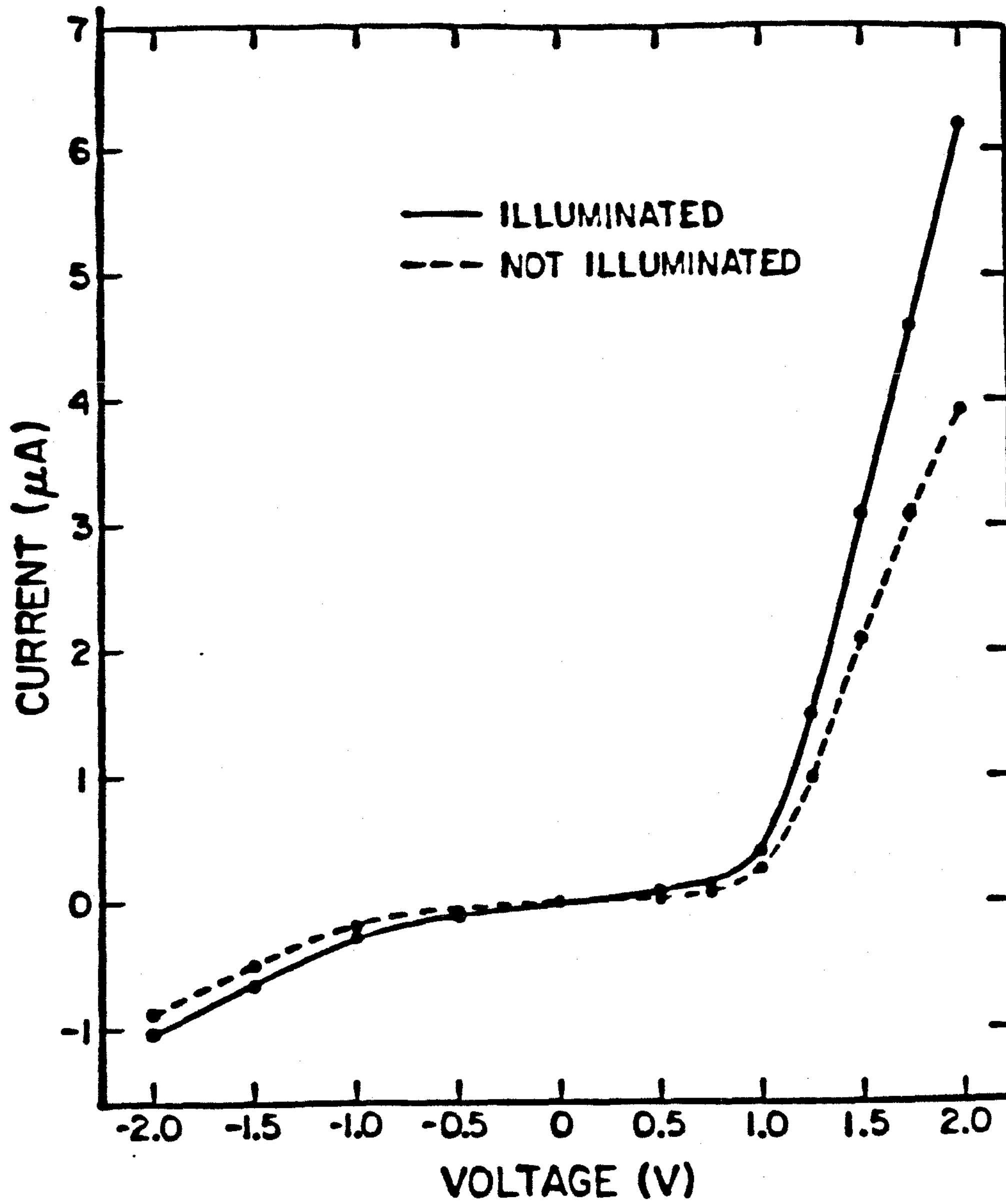

Figure 5.8 Current-voltage characteristic of the device at 77 °K. Illumination was with a broadband IR source (2700 °K) and a GaAs filter was used.

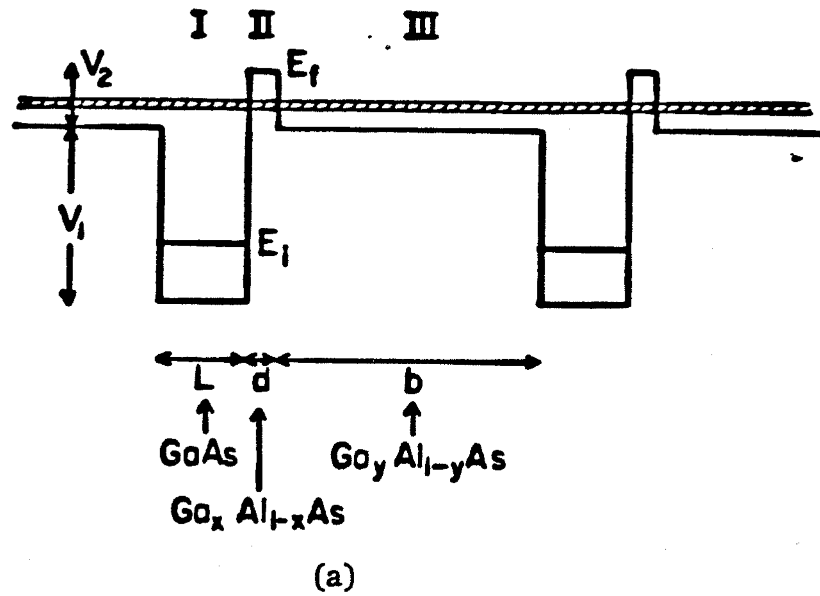

(a)

Figure 5.7 (a) and (b) Band (conduction) structures of the proposed detector at thermal equilibrium.

(c) Band structure of (b) under an externally applied bias.

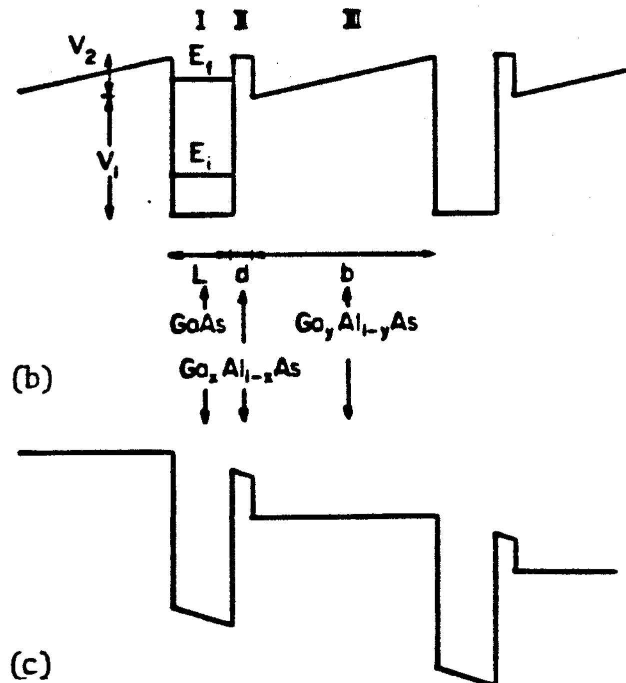

has lower mobility than 5.7(a). However, when an external voltage is applied, the mobility is expected to be enhanced significantly as can be seen from Fig. 5.7(c). The energy versus wave vector (E vs. k) relation can be obtained by assuming a bloch type wave function, as in Kronig-Penny model, and solving a 6×6 determinant. However, to minimize detector dark current, the lowest lying level E_i in the well region should be effectively decoupled to prevent high dark current due to tunneling effect. In such case, the wave function can be approximated by (5.3.1). By proper matching of the widths L, b, and d, both the energy and momentum conservation requirements can be met (i.e. we can find $E_f(k_x)-E_i(\frac{\pi}{L})=\hbar\omega$ with $k_x \approx \frac{\pi}{L}$). The absorption coefficient can then be estimated as in section 5.3. For L=100μm, d=15Å, b=250Å, V_2=0.1eV, and V_1=0.3eV, the inter-subband absorption coefficient can then be expressed approximately as

$$\alpha = 7.6\times10^{-3} \left(\frac{m_c}{m_o}\right) f \frac{1}{L} \left[1 - e^{-\frac{n\pi\hbar^2 L}{m_c kT}}\right] \tag{5.6.1}$$

where m_c is the electron effective mass, N the electron density in the well region, and the oscillator strength f is given by $\frac{2}{m_o\hbar\omega}|P_{fi}|^2$. Fig. 5.8 shows α as a function of N at 77 and 300 °K. The value of m_c was taken to be the bulk value of 0.067m_o where the effect of quasi two dimension on the effective mass has been neglected. The momentum matrix element P_{fi} was assumed to take the form as derived in [5.7]. We see that due to the direct "resonant" nature of the transition, the absorption coefficient is greatly enhanced. This would lead to much greater sensitivity compared to the free carrier absorption case.

To function as a detector, the excited electrons must be "pulled out" of the well region under an applied potential before it relaxes back to E_i. In the present structure, the probability for an electron to be recaptured by the "mother" well or by other wells depends critically on L and d. Because region II (see Fig. 1)

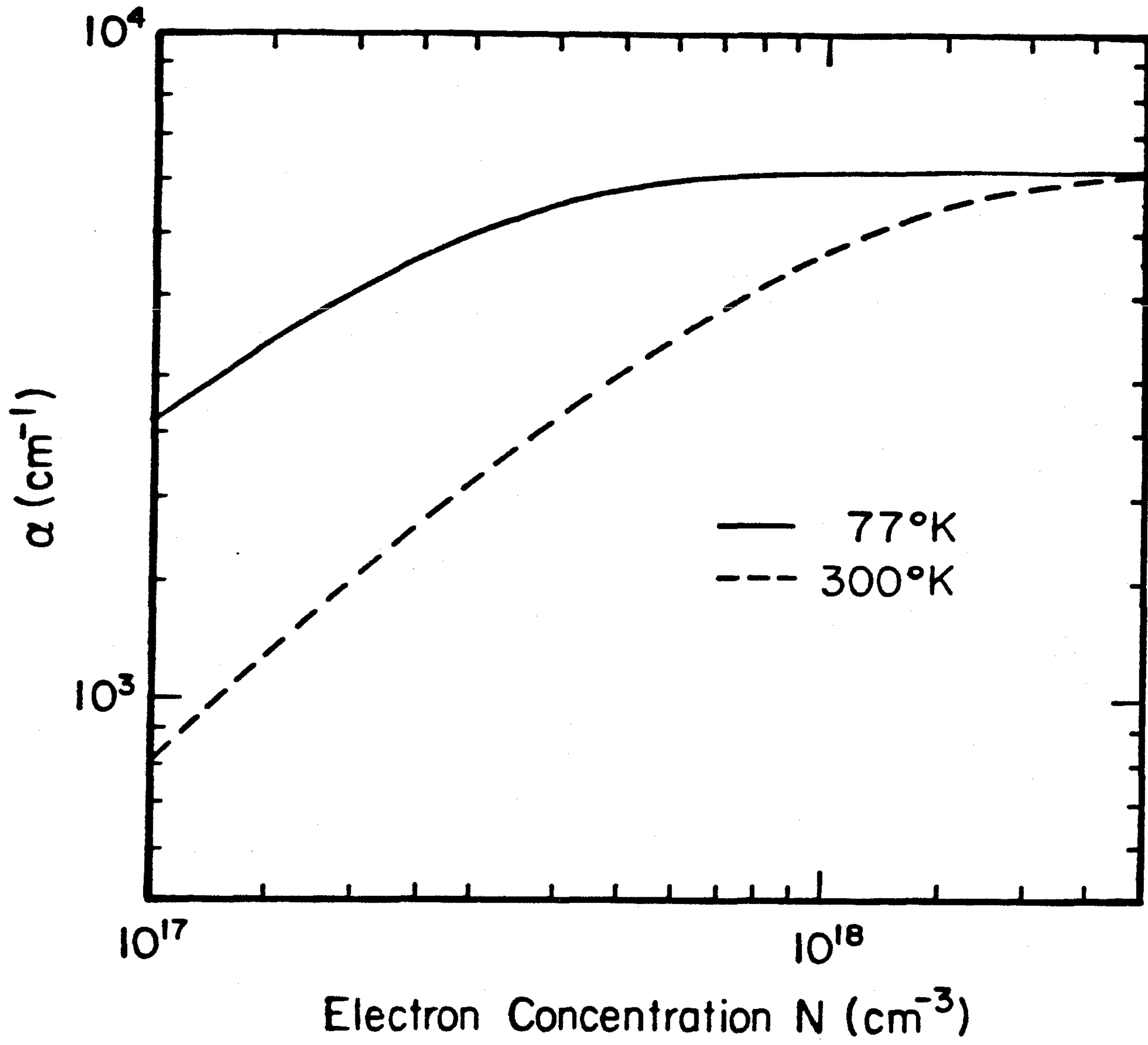

Figure 5.8 **Calculated absorption coefficient as a function of electron density at 77 and 300 °K.**

presents a barrier to the excited electrons, d must be made thin so as to increase the tunneling probability. The estimated quantum mechanical tunneling probability per incidence for a "free" electron in band E_f in the absence of an external field is shown in Fig. 5.9. The values are expected to be significantly higher when an external voltage is applied, since then the electron velocity distribution will be anisotropic; besides, some electrons will be scattered into the continuum band. Trade offs between absorption coefficient and tunneling probability can be made by changing the width L and d, or by varying the externally applied voltage, which simultaneously adjust the trade offs between device gain and response time.

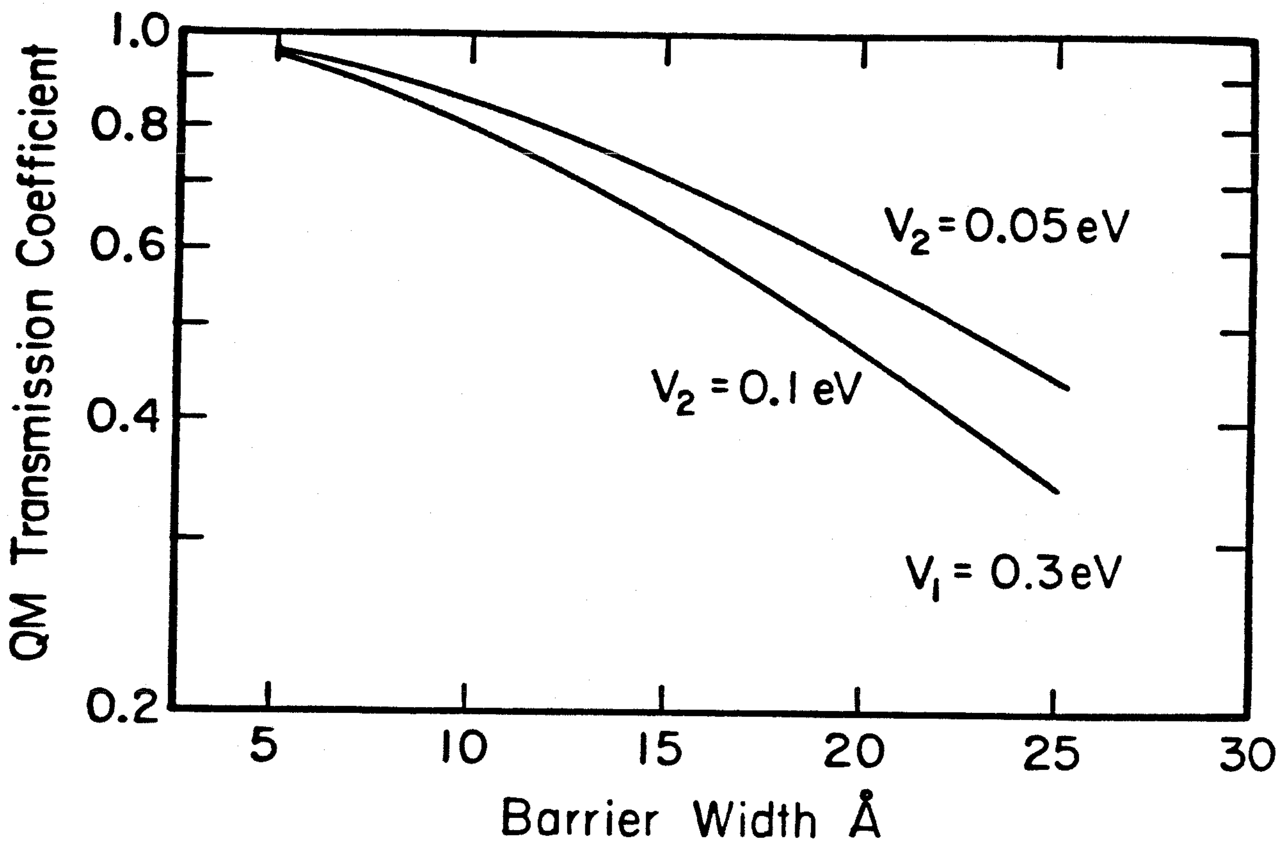

Figure 5.9 Estimated tunneling probability in the absence of external bias as a function of barrier width d.

Appendix B

Absorption Coefficient

In this appendix, general expression (B.6) for absorption coefficient will be derived. In particular, omitted steps leading to (5.3.6) will be filled in.

Let P/Ω denote the transition rate per unit volume for electrons from initial state $\vec{k}$ to the final state $\vec{k}'$. We then have

$$\frac{P}{\Omega} = \frac{Nc}{n_r\Omega}\alpha \tag{B.1}$$

where N is the total photon number in Ω. On the other hand, the photon flux S is given by

$$S = \frac{Nc}{n_r\Omega}\hbar\omega \tag{B.2}$$

However, S in (B.2) is just the magnitude of the time averaged poynting vector given by

$$S = \frac{1}{2}\omega^2\varepsilon_o n_r A_o^2 \tag{B.3}$$

From (B.1-B.3),

$$\alpha = \frac{P}{\Omega}\frac{2\hbar^2}{\varepsilon_o n_r A_o^2}\frac{1}{\hbar\omega} \tag{B.4}$$

From Fermi's Golden Rule,

$$P = \frac{2\Omega}{(2\pi)^3}\int d\vec{k}'\,\frac{2\pi}{\hbar}\,|H_{fi}|^2\,\rho(E) \tag{B.5}$$

where $\rho(E)$ is the joint density of states which includes the Fermi occupation factors.

From (B.4) and (B.5), we obtain

$$\alpha = \frac{1}{\pi^2 n_r \varepsilon_o \omega} \frac{1}{A_o^2} \int d\vec{k}' \, |H_{fi}|^2 \rho(E) \tag{B.6}$$

From (5.3.4),

$$H_{fi} = \frac{eA_o\sqrt{2}}{2m_oL} P_{fi} \int_o^L \sin\frac{\pi x}{L} e^{-ik_x x} dx = \frac{eA_o\sqrt{2}}{2m_oL} P_{fi} I \tag{B.7}$$

Substituting (B.7) into (B.6), we get

$$\alpha = (\frac{1}{137}) \frac{2\hbar c}{\pi n_r \omega} \int d\vec{k} \frac{1}{(m_oL)^2} |P_{fi}|^2 I^2 \frac{1}{e^{\frac{E_o - E_{fc}}{kT}} + 1} \tag{B.8}$$

where the final state is assumed to be unoccupied. Under the constant optical matrix assumption, and assuming only the lowest confined state is occupied, (B.8) can be simplified to

$$\alpha = (\frac{1}{137}) \frac{4m_c c^2}{n_r \omega m_o^2 L^3 \hbar c} |P_{fi}|^2 I^2 \frac{1}{e^{\frac{E_o - E_{fc}}{kT}} + 1} \tag{B.9}$$

The quasi Fermi level E_{fc} can be expressed in terms of the carrier concentration n as

$$n = \frac{m_c}{\pi\hbar^2 L} \int_{E_o}^{\infty} \frac{1}{e^{\frac{E - E_{fc}}{kT}} + 1} dE \tag{B.10}$$

$$= \frac{m_c}{\pi\hbar^2 L} kT \ln [1 + \frac{E_{fc} - E_o}{kT}]$$

Thus,

$$\frac{1}{e^{\frac{E_o - E_{fc}}{kT}} + 1} = 1 - e^{-\frac{n\pi^2\hbar^2 L}{m_c kT}} \tag{B.11}$$

Substituting (B.11) into (B.9), we have finally

$$\alpha = \left(\frac{1}{137}\right) \frac{4m_c c^2}{n_r \omega m_o{}^2 L^3 \hbar c} |P_n|^2 I^2 \left[1 - e^{-\frac{n\pi^2\hbar^2 L}{m_c kT}} \right] \qquad \text{(B.12)}$$

which is used in deriving (5.3.6) and (5.6.1).

References - Chapter 5

5.1 A. Y. Cho, J. Vac. Sci. Tech., **16**, p. 275 (1979)

5.2 S. Visvanathan, Phys. Rev. **120**, pp 376 (1960)

5.3 R. Dingle, H. L. Stormer, A. C. Gossard, and W. Wiegman, Appl. Phys. Lett. **33**, pp 665 (1978)

5.4 K. Seeger, 'Semiconductor Physics," , Chapter 11, Springer Verlag, Wien (1976)

5.5 L. Esaki and L. L. Chang, Phys. Rev. Lett. **33**, pp 495 (1974)

5.6 T. Ando and S. Mori, J. of Phy. Soc. of Japan, **47**, pp 1518 (1979)

5.7 E. O. Kane, J. Phys. Chem. Solids, **1**, p. 249 (1957)

5.8 W. W. Anderson, IEEE J. Quant. Elect., **QE-13**, p. 532 (1977)

5.9 A. Sugimura, IEEE J. Quant. Elect., **QE-17**, p. 627 (1981)

5.10 See for example, S. M. Sze, 'Physics of Semiconductor Devices," Chap. 13, p. 760, Wiley Interscience, New York (1981)

5.11 P. R. Bratt, in "Semiconductors and Semimetals," Vol. XII, Chap. 2, Academic Press, New York (1977)